Convective processes in the polar atmospheric boundary layer:

a study based on measurements and modeling

Dissertation

zur Erlangung des Grades
Doktor der Naturwissenschaften
–Dr. rer. nat.–

vorgelegt im
Fachbereich 1 (Physik/Elektrotechnik)
der Universität Bremen

von

Amelie Tetzlaff

Universität Bremen

ALFRED-WEGENER-INSTITUT
HELMHOLTZ-ZENTRUM FÜR POLAR-
UND MEERESFORSCHUNG

1. Gutachter: Prof. Dr. Peter Lemke
2. Gutachter: Prof. Dr. Thomas Jung

Die Dissertation wurde angefertigt am

Alfred-Wegener-Institut Helmholtz-Zentrum für Polar- und Meeresforschung

in Betreuung durch die Gutachter und Dr. Christof Lüpkes

Eingereicht am: 17. September 2015
Datum des Kolloquiums: 10. Dezember 2015

Convective processes in the polar atmospheric boundary layer:

a study based on measurements and modeling

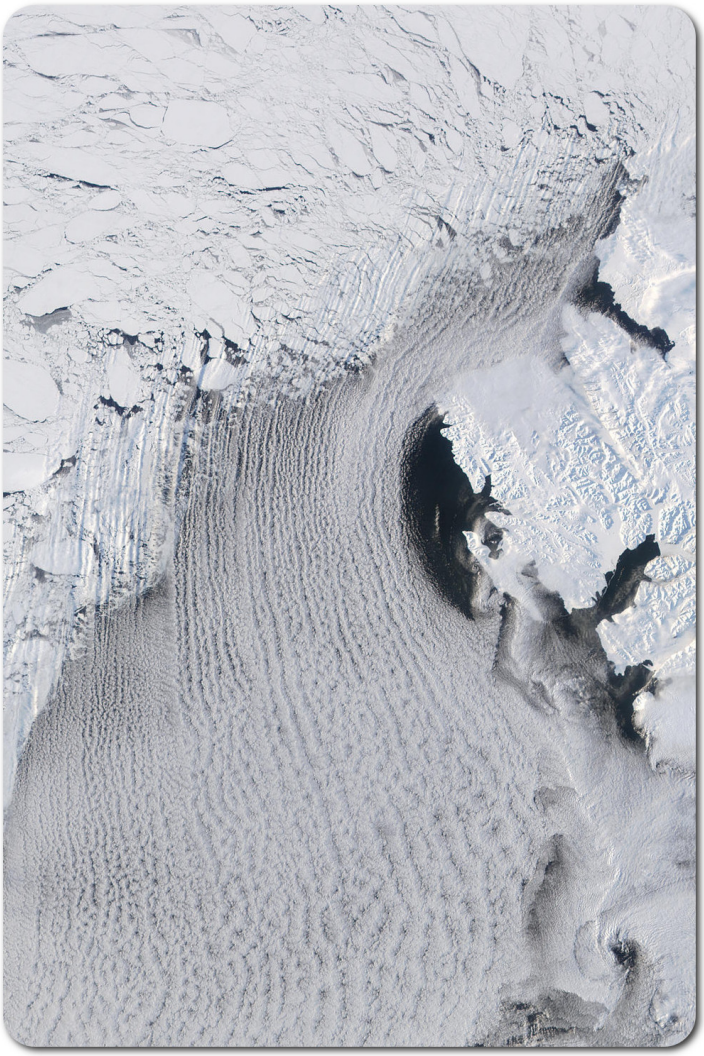

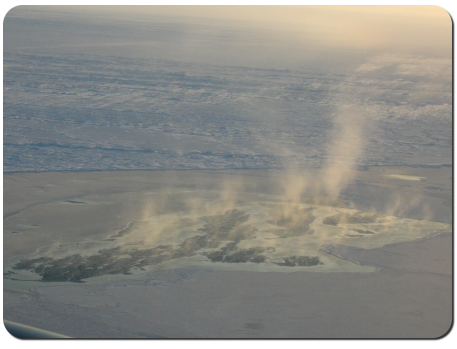

Amelie Tetzlaff

Abstract

Climate change is especially pronounced over the Arctic Ocean, where the atmosphere warmed twice as fast as in lower latitudes in the last few decades. This warming is associated with a rapid decline of the Arctic sea ice cover. For future predictions of changes in the Arctic climate system, profound knowledge of all processes influencing the surface energy budget in polar regions is essential. The focus of this thesis lies on improving our current understanding of convective processes and the related turbulent fluxes in the polar atmospheric boundary layer (ABL) over both the sea ice covered regions and over the open ocean at the sea ice edge. A major part of the analysis is based on aircraft measurements from the campaign STABLE, which was carried out over the pack ice in the northern Fram Strait in March 2013. These results are supplemented by modeling studies using a simple boxmodel and a one-dimensional mesoscale model.

For the first time, comprehensive aircraft measurements over leads were conducted during the campaign STABLE. They are used to study the formation of convective plumes over leads and their impact on the polar ABL. It is found that the conditions over four wide leads are highly variable with respect to turbulent fluxes, as well as to the mean variables temperature, humidity, and wind. In one of the cases large entrainment fluxes exceeding 30 % of the surface fluxes are observed. The convective plumes over leads have a large influence on the vertical profiles of sensible heat and momentum fluxes, which are non-linear downstream of the leads with a distinct flux maximum in the core of the convective plumes. For the first time, it it shown based on measurements that the plume also affects the wind field by diminishing low level jets in the region influenced by the plume. In addition to the small scale impact of individual leads the regional impact of lead ensembles is studied using long transect flights. The analysis shows that near-surface atmospheric temperatures are clearly related to the ice concentration in the considered region.

The impact of a heterogeneous sea ice cover and of the related surface temperature changes on atmospheric temperatures is also analysed using a Lagrangian box model. The model uses reanalysis winds as well as sea ice concentration and surface temperature from satellites as input data. The box model is used to calculate the evolution of the near-surface air temperature along backward-trajectories, which are then compared to measured temperatures at three different Arctic sites. The results suggest that a large amount of the observed air temperature variability can be attributed to heterogeneous surface temperatures and that the characteristic length of the upstream region influencing air temperatures at a specific location is 200 km.

Convection during cold air outbreaks at the sea ice edge has a much stronger impact on the polar ABL than convective plumes over leads. Dropsonde measurement of four cold air outbreaks during STABLE are used to analyse the downstream development of meteorological variables and the ABL growth. Two of the considered cases are influenced by the size of the Whaler's Bay polynya north of Svalbard, which was unusually large in the three winters from 2012 to 2014 compared to the previous 20 years. The analysis of the dropsonde measurements shows that the unusual ice conditions lead to strong atmospheric convection in a region north of Svalbard that was typically ice-covered in the last decades. This leads to extreme convective ABL heights and modifies local temperature conditions considerably.

Convective processes in the ABL have to be parametrised in climate models. Therefore, in addition to the measurements, the performance of three different sensible heat flux parametrisations is tested in a 1D mesoscale model and results are compared to those of a large eddy simulation

model (LES). Both the considered counter-gradient and eddy-diffusivity mass-flux (EDMF) approach reproduce the shape of the temperature profile of the LES better than a classical mixing length approach. A sensitivity analysis shows that the EMDF approach is the least sensitive to changes of the vertical grid spacing, which can be attributed to the derivation of the ABL height using a diagnostic equation of the updraft velocity. The sensitivity of the counter-gradient closure to the grid spacing can be significantly reduced when the updraft velocity equation of the EDMF approach is included and used to derive the ABL height.

Contents

1 Introduction

Sea ice is an important part of the climate system and covers up to 10 % of the Earth's ocean surface. It acts as an insulating lid and thus has a large impact on the exchange of energy, moisture, gases, and momentum between ocean and atmosphere. The strength of this insulation effect depends on ice thickness and ice concentration. A direct interaction between atmosphere and ocean is only possible over open water areas in so-called leads and polynyas and over the open polar ocean at the sea ice edge.

The term "lead" is commonly used for elongated channels in sea ice that form due to divergent sea ice drift. Typically, leads have widths of a few meters to a few kilometers and lengths of a few hundred meters to hundreds of kilometers (Lindsay and Rothrock, 1995; Marcq and Weiss, 2012) and are covered by open water or thin ice. The term "polynya" refers to a larger ice free area of up to thousands of km^2 in size occurring at a fixed location (e.g. Barber et al., 2001). Polynyas can either form due to offshore winds that push the sea ice away from the shore or from a fast ice edge or due to upwelling warm water. They are also important areas for ice production and associated dense water formation (e.g. Tamura et al., 2008). Examples of visible satellite images of leads and polynyas are shown in Fig. 1.1.

Temperature differences between the air and the surface of leads or polynyas can easily exceed 30 °C in winter and spring leading to strongly enhanced turbulent heat transport from the ocean to the atmosphere. While upward turbulent heat fluxes over thick sea ice are typically in the order of $5\,W\,m^{-2}$ (Maykut, 1982), they can be two orders of magnitude larger over open water (Maykut, 1986) and are still enhanced over thin ice (Alam and Curry, 1997). This means that areas covered by open water or thin ice have a large impact on the local energy budget over sea ice. The large impact of small ice concentration changes on near-surface atmospheric temperatures has been demonstrated by Lüpkes et al. (2008b). They used a one-dimensional atmospheric model coupled with a sea ice model and found that under clear skies in winter a decrease of the ice concentration by 1 % caused an air temperature increase of up to 3.5 K after 2 days model runtime.

Large turbulent sensible and latent heat fluxes also occur during cold air outbreaks when cold air flows off the sea ice towards the warmer open ocean. For example, Brümmer (1996) measured sensible and latent heat fluxes of up to $700\,W\,m^{-2}$ at 90 m height during several cold air outbreaks west of Spitzbergen. Cold air outbreaks are characterized by extreme modifications of the atmospheric boundary layer with respect to height, temperature, humidity, and cloud cover, and thus have a large impact on the local climate.

Especially in the context of climate change a better understanding of all processes influencing the surface energy budget in polar regions is crucial. In the last few decades the observed warming rates over the Arctic ocean were twice as large as those in lower latitudes (Serreze et al., 2009; Screen and Simmonds, 2010). This so-called Arctic amplification is associated with a decline in Arctic sea ice cover. Sea ice, especially when covered by snow, has a high albedo and reflects a

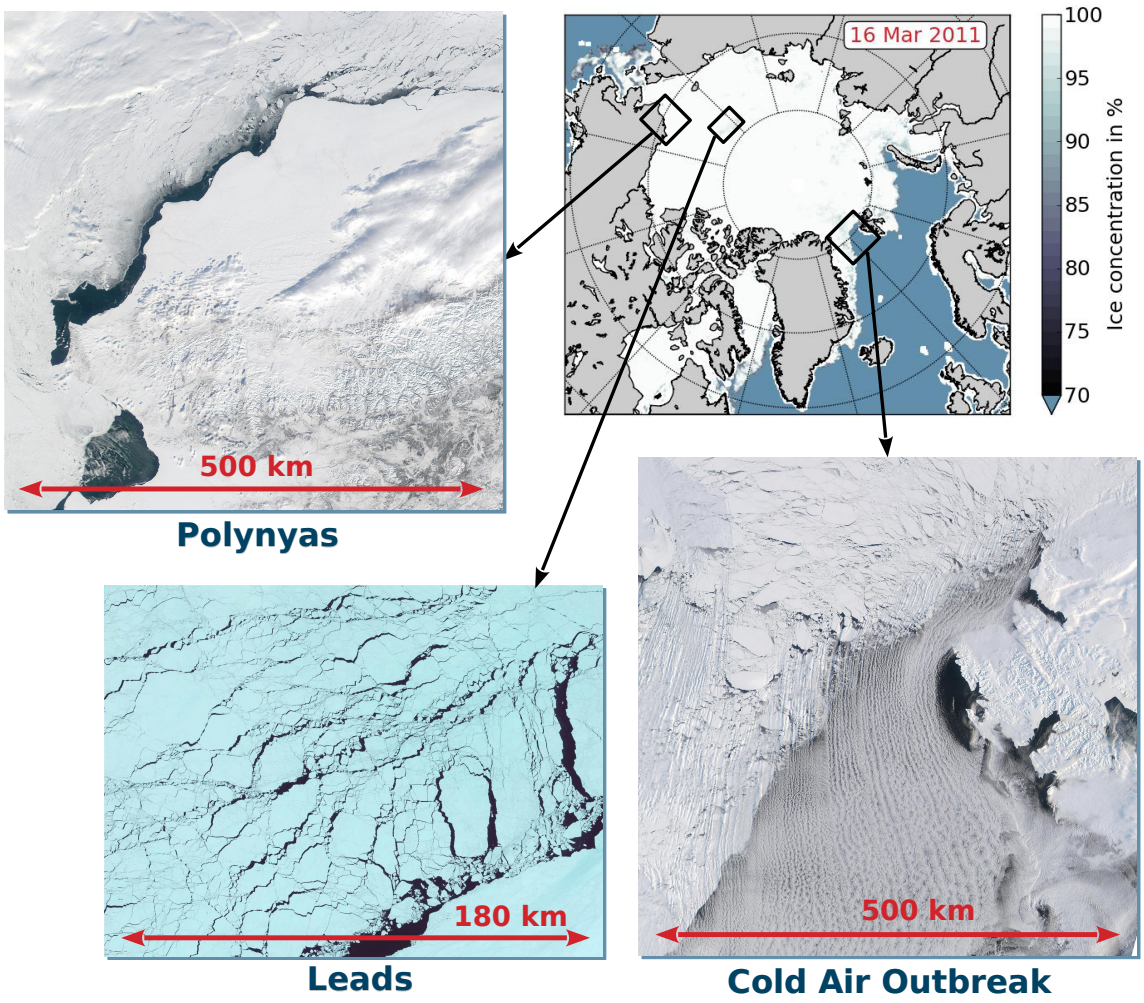

Figure 1.1: Exemplary visible satellite images of a polynya (Modis Terra image on 18 March 2002[1]), leads (Landsat 5 image on 29 April 2005[2]), and a cold air outbreak (Modis Terra image on 3 March 2002[1]). Upper right: SSM/I-ASI sea ice concentration[3] in the Arctic on 16 March 2011.

large part of the incoming solar radiation back to space. A reduced sea ice cover exposes more open water, which has a much lower albedo and absorbs more incoming radiation. The resulting warming of the upper layers of the ocean causes an enhanced sea ice melt. This mechanism is called the ice-albedo-feedback and is one of the drivers for Arctic amplification (e.g. Perovich et al., 2007). Other drivers include an increased meridional heat transport, an altered radiation budget due to changes in cloud cover and water vapor content of the atmosphere, and warming due to black carbon aerosols (Serreze and Barry, 2011).

A reduced sea ice concentration and thickness has large effects on the surface energy budget over the Arctic Ocean. Deser et al. (2010) used a general circulation model to investigate the atmospheric response to the projected Arctic sea ice loss at the end of the twenty-first century. They found the largest response in winter and early spring with an increase of turbulent sensible and latent heat fluxes of up to $90\,\mathrm{W\,m^{-2}}$ compared to fluxes that were obtained using sea ice conditions at the end of the twentieth century. These increased heat fluxes are associated with

[1]Data from visibleearth.nasa.gov (accessed 5 Juni 2012)
[2]Data from earthexplorer.usgs.gov (accessed 5 Juni 2012)
[3]Data from ftp.ifremer.fr (accessed 5 Juni 2012)

an increase of the near-surface temperature that exceeds 15 °C in winter. This demonstrates that a profound understanding of the heat exchange and the associated convective processes in the polar atmospheric boundary layer is essential for future predictions of changes in the Arctic climate system.

Therefore, the objectives of this thesis are to deepen our knowledge of convective processes induced by a heterogeneous sea ice cover – in particular over leads and during cold air outbreaks at the sea ice edge. A major part of the investigations is based on aircraft measurements, supplemented by modeling results obtained with a simple box model and a one-dimensional mesoscale model.

1.1 Arctic sea ice

The Arctic Ocean is surrounded by continents and characterized by a seasonally varying sea ice cover. In the last decades Arctic sea ice has exhibited drastic changes with respect to sea ice extent, thickness, and age. A comprehensive review of these changes is given by Stroeve et al. (2012) and Meier et al. (2014), which will be summarized in the following.

The first satellite-based measurements of sea ice concentrations were those by the Nimbus-5 Electrically Scanning Microwave Radiometer (ESMR) between 1972 and 1976. The longest continuous time series for sea ice extent started in 1978 with the Scanning Multichannel Microwave Radiometer (SMMR), followed by the Special Sensor Microwave/Imager (SSM/I) and the Special Sensor Microwave Imager/Sounder (SSMIS). Over this period Arctic sea ice extent declined in all seasons with the most pronounced downward trend in summer and early autumn. The decline rates of the minimum sea ice extent in September are more than twice as large as those for the maximum extent in March (Fig. 1.2), with values of about -87 000 and -41 000 km^2 per year, respectively (based on the NSIDC sea ice index, Fetterer et al. (2002)). This is equivalent to a September retreat rate of the ice extend of 12 % per decade since 1979. In March 2015 the sea ice extent reached the lowest maximum value observed since the beginning of the satellite era. The decline rates also show large regional differences. For example, Cavalieri and Parkinson (2012) reported that in March the overall Arctic sea ice extent declined by about 3 % per decade from 1979 to 2010, while the decline rates were much larger in the Barents Sea and Greenland Sea regions with values exceeding 5 %.

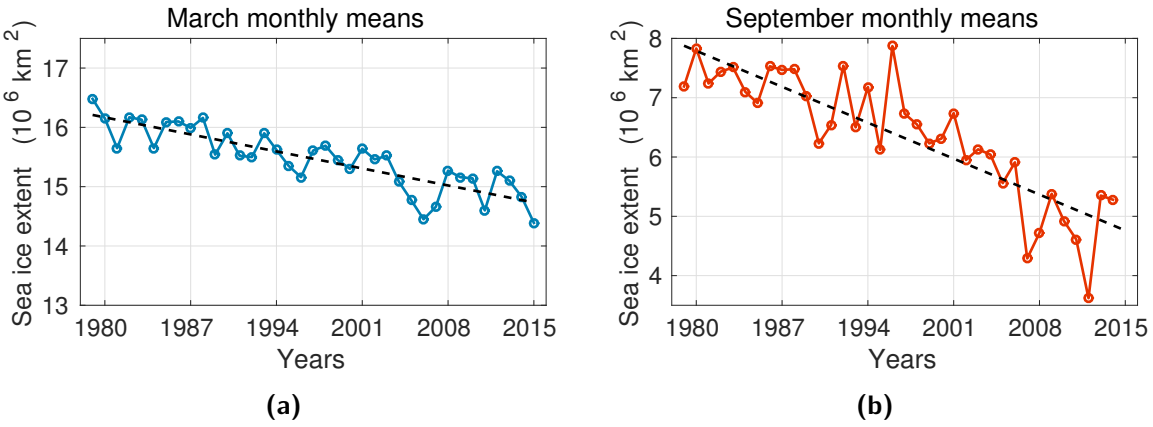

Figure 1.2: Monthly mean Arctic sea ice extent in **(a)** March and **(b)** September based on the sea ice index data from NSIDC (Fetterer et al., 2002).

Measurements of sea ice thickness are more sparse in space and time, which makes it more difficult to determine trends. More or less frequent pan-Arctic ice thickness surveys have been conducted using an airborne electromagnetic induction system (EM bird) since the early 2000s (Haas et al., 2010). By combining ground-based and airborne EM measurements Renner et al. (2014) found a thinning of the sea ice in the Fram Strait at the end of the melt season by over 50 % between 2003 and 2012.

In a recent study Lindsay and Schweiger (2015) combined thickness measurements from upward-looking sonars, from airborne electromagnetic sensors, and from lidar or radar altimeters on airplanes and satellites to derive a comprehensive dataset. They found that the annual mean Arctic ice thickness decreased with a rate of -5.8±0.7 cm per year between 2000 and 2012. While in 1975 the sea ice was on average 3.59 m thick, this value decreased to only 1.25 m in 2012, which means a reduction of 65 %. For September, at the end of the melt season, the reduction was even as large as 85 %.

Arctic-wide sea ice thickness and volume estimates are available from the CryoSat-2 satellite, which was launched in 2010 (Laxon et al., 2013). In a recent study Tilling et al. (2015) showed that a decline in sea ice volume between autumn 2010 and 2012 was followed by an increase in 2013 and 2014. They attributed this increase to the retention of multi-year ice north of Greenland and a relatively low number of days on which melting occurred in 2013.

The thinning of the Arctic sea ice cover also implies a reduced sea ice age. This means a shift from a sea ice cover that was previously dominated by multi-year ice to mostly first-year ice. Maslanik et al. (2011) showed that the multi-year fraction of the total sea ice cover in March decreased from 75 % in the mid 1980s to 45 % in 2011. In addition, sea ice that is older than four years has nearly disappeared. The resulting thinner Arctic sea ice cover dominated by first-year ice is more vulnerable to further melting, which suggests the possibility of a seasonally ice-free Arctic Ocean.

1.2 Leads in sea ice

The characteristics of leads and the interactions of leads with other components of the climate system are of interest for many disciplines of polar research. Refreezing of the surface of leads has a strong impact on the ocean. The salty brine released during the ice formation causes dense water formation, which induces convection in the ocean and impacts the halocline (Smith and Morison, 1993; Morison and McPhee, 1998; Matsumura and Hasumi, 2008). Leads are also regions of high biological productivity and thus important feeding grounds for marine mammals and birds (Stirling, 1997). In the context of this thesis we focus on the impacts of leads on the atmospheric boundary layer (ABL).

Especially in winter and spring, when temperature differences between the air and the lead surface are large, leads are regions of enhanced atmospheric convection. When cold air is advected over a lead, the initiated convection causes the formation of a plume. We use the expression "plume" for the region influenced by the individual convective elements (thermals) emanating from a lead (see Fig. 1.3). In the past, various studies have been conducted to investigate the plume growth, its structure and the associated boundary layer modification. In the following, we summarize the results of these studies, which were based on near-surface measurements during different campaigns, such as AIDJEX (Andreas et al., 1979), LEADEX (Ruffieux et al., 1995), and SHEBA (Overland et al., 2000), and on model results obtained with mesoscale models (e.g. Dare and Atkinson, 2000; Lüpkes et al., 2008a) and large eddy simulations (e.g. Weinbrecht and Raasch, 2001; Esau, 2007).

Air flowing towards a lead experiences an abrupt change of surface temperature and roughness at the lead edge, which initiates the growth of an internal boundary layer (IBL). The height of

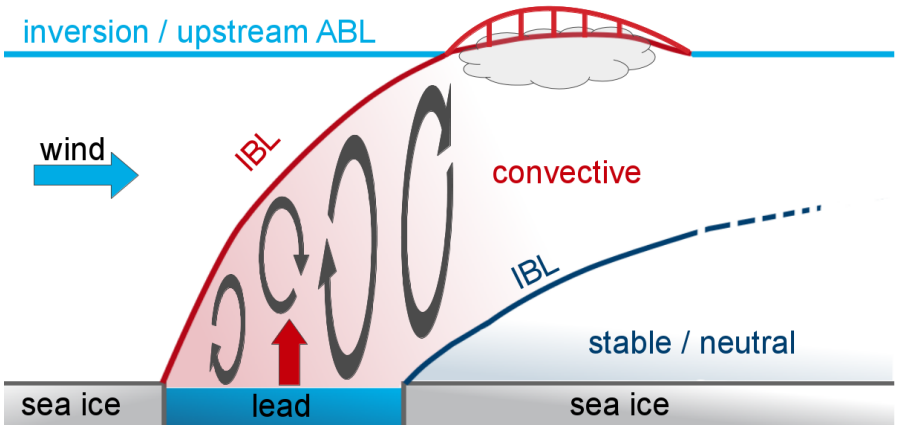

Figure 1.3: Sketch of the convective plume forming over a lead including the growth of the convective internal boundary layer (IBL) over the lead and a second stably or neutrally stratified IBL over the thick pack ice downstream of the lead. Adapted from Lüpkes et al. (2008a).[1]

the IBL coincides with the upper plume boundary and increases with increasing distance over the lead (fetch). When the growing plume reaches the top of the boundary layer of the incoming flow it can even penetrate the lowest layers of the capping inversion. Further donwstream of the lead, over the thicker and colder sea ice the growth of a second IBL is initiated, which typically shows a stable or near neutral stratification (see Fig. 1.3).

The IBL over the lead has a convective character, with large turbulent sensible and latent heat fluxes that can exceed several hundred $\mathrm{W\,m^{-2}}$ (e.g. Ruffieux et al., 1995; Pinto et al., 2003). Even though sensible heat fluxes decrease over thin ice when the lead surface refreezes (Lüpkes et al., 2012b; Pinto et al., 2003), model results by Alam and Curry (1997) suggest that a lead with a 20 cm thin ice cover can still produce turbulent fluxes that are up to 10 times higher than those over the surrounding pack ice in winter. In addition, leads are also an important moisture source and can cause sea smoke, fog, and even trigger cloud formation (Pinto and Curry, 1995).

The convective plume impacts also the region downstream of the lead. Measurements during LEADEX (Ruffieux et al., 1995) showed an increase of the 2 m air temperature and a decrease of atmospheric stability downstream of a lead compared to its upstream values. Pinto et al. (2003) reported that during SHEBA the influence of a 400 m wide lead extended more than 2.5 km downwind during lead-perpendicular winds. Thus, leads do not only have local impacts but larger leads can also affect the atmosphere on regional scales.

Various studies suggest that the characteristics of the convective plume depend on lead width or lead fetch, ice cover and open water fraction of the lead, wind speed, as well as the upstream stratification of the ABL and the strength of the capping inversion (Glendening, 1995; Pinto et al., 1995, 2003; Zulauf and Krueger, 2003a,b; Alam and Curry, 1995). It is important to note that, especially for processes in the upper layers of the plume, our present knowledge is to a large extent based on modeling studies only, since observations are rare.

Since the convective processes over leads take place on scales that are much smaller than typical grid sizes of climate models, their impact on the polar ABL has to be parametrised. However, current model parametrisations only consider the average ice concentration within a grid cell and leads are mostly not treated explicitly (e.g. Bitz et al., 2001; Gordon and O'Farrell, 1997). In those models the total heat flux is calculated as the area weighted average of the fluxes over open water and over sea ice. Such formulations cannot account for the actual width and sea ice cover of the leads, nor for their orientation within the grid cell, which is a crucial

[1] This figure has been published in Tetzlaff et al. (2015)

shortcoming. For example, Andreas and Murphy (1986) and Andreas and Cash (1999) showed that the heat transfer is more effective over narrow leads than wider ones. Furthermore, Marcq and Weiss (2012) calculated that for a considered area of 60 km times 66 km sensible heat fluxes are underestimated by up to 30 % when fluxes are calculated using the flux-averaging method rather than accounting for the actual observed lead width distribution.

1.3 Cold air outbreaks

Cold air outbreaks (CAOs) developing at the boundary between pack ice and open ocean have a large impact on the exchange of energy and mass between ocean and atmosphere. They can influence regions of more than 1000 km length and are often associated with convective rolls that are visible as cloud streets in satellite images (see Fig. 1.1). Further downstream, the organized convection typically changes from longitudinal rolls to cellular patterns. During CAOs the ABL height can rise from typically 100 m over the sea ice covered region to more than 2 km at 200 km downstream of the marginal sea ice zone where no sea ice is present. Over this distance, an increase of the ABL temperature of up to 20 K has been documented by Brümmer (1996).

Measurements of cold air outbreaks were obtained during many different aircraft campaigns in the Barents and Greenland Seas (Brümmer et al., 1992; Brümmer, 1996, 1997; Brümmer, 1999; Hartmann et al., 1997), which are regions of frequent CAOs in the Arctic (Brümmer and Pohlmann, 2000; Kolstad and Bracegirdle, 2008). Since the decrease of the winter sea ice cover is especially pronounced in these regions (Cavalieri and Parkinson, 2012), we can also expect an impact on CAOs. A northward retreat of the ice edge causes a shift of the locations of CAOs (Kolstad and Bracegirdle, 2008) and can thus have a large impact on local temperature conditions.

A better understanding of CAOs is also particularly important because of their association with hazardous weather conditions, such as strong winds and snowfall during polar lows (Rasmussen and Turner, 2003). Thus, it is problematic that some important features of CAOs are not well represented in climate models. One of these features are convective rolls, which are important for the modeling of fluxes within the ABL (e.g. Liu et al., 2006). Therefore, different large eddy simulations (LES) were conducted to better understand the processes related to roll convection (e.g. Raasch, 1990; Chlond, 1992; Müller and Chlond, 1996; Gryschka and Raasch, 2005).

Most recently, Gryschka et al. (2008) found that in case of strong surface heating convective rolls are initiated by sea ice inhomogeneity in the marginal sea ice zone. These rolls were found to account for up to 50 % of the vertical transport in the model (Gryschka et al., 2014), which is in line with the contributions derived from aircraft measurements by Brümmer (1999). However, the total fluxes did not increase compared to a case without convective rolls, which implies that the convective rolls only take over a part of the transport from the unorganized turbulence. This finding contradicts the widely accepted idea that rolls have a large impact on the total fluxes (e.g. Liu et al., 2006; Etling and Brown, 1993; Young et al., 2002), which demonstrates that the processes related to convective rolls are yet not fully understood.

Other studies dealt with the representation of CAOs in mesoscale models. It has been shown by Lüpkes and Schlünzen (1996) and Chechin et al. (2013) that models with horizontal grid sizes in the range of 1 to 15 km, which do not resolve convective rolls, are able to reproduce the mesoscale structure of the wind and temperature fields in the convective ABL in good agreement with observations. However, with further increased grid sizes the strength of the ice-breeze jet was underestimated (Chechin et al., 2013). This jet-like structure often develops in the region between the ice edge and 100 km downstream of it and has a large impact on the modeled surface fluxes of heat and momentum.

1.4 The aircraft campaign STABLE[1]

1.4.1 Study region and flight patterns

To increase the number of available measurements over leads and during cold air outbreaks were two of the goals of the aircraft campaign STABLE (Spring Time Atmospheric Boundary Layer Experiment). This campaign was organized by the Section Polar Meteorology (campaign leader: Christof Lüpkes) of the Department of Climate Sciences at the German Alfred Wegener Institute (AWI) in Bremerhaven and has been carried out jointly with the Finnish Meteorological Institute in Helsinki. It took place in March 2013 over the sea ice covered region and open ocean of the Fram Strait and was conducted using AWI's Polar 5 aircraft. In this thesis 9 of the total 15 flights that were carried out are used (see Fig. 1.4). Four of these flights included so-called lead patterns, during which flight sections were located parallel and perpendicular to single wide leads. These flight patterns aimed at studying the boundary layer modification and the heat exchange over leads. In addition, five long low-level flights over the sea ice covered region were carried out, which can be used to get an overview of the typical lead widths and surface temperatures in this region, as well as to estimate the impact of leads on the ABL on regional scales.

Furthermore, dropsondes were launched during four flights over the open ocean when CAOs were present. As described in Sect. 1.3, such measurements of CAOs have been carried out during previous campaigns in this region. The significant difference to those campaigns is, however, the

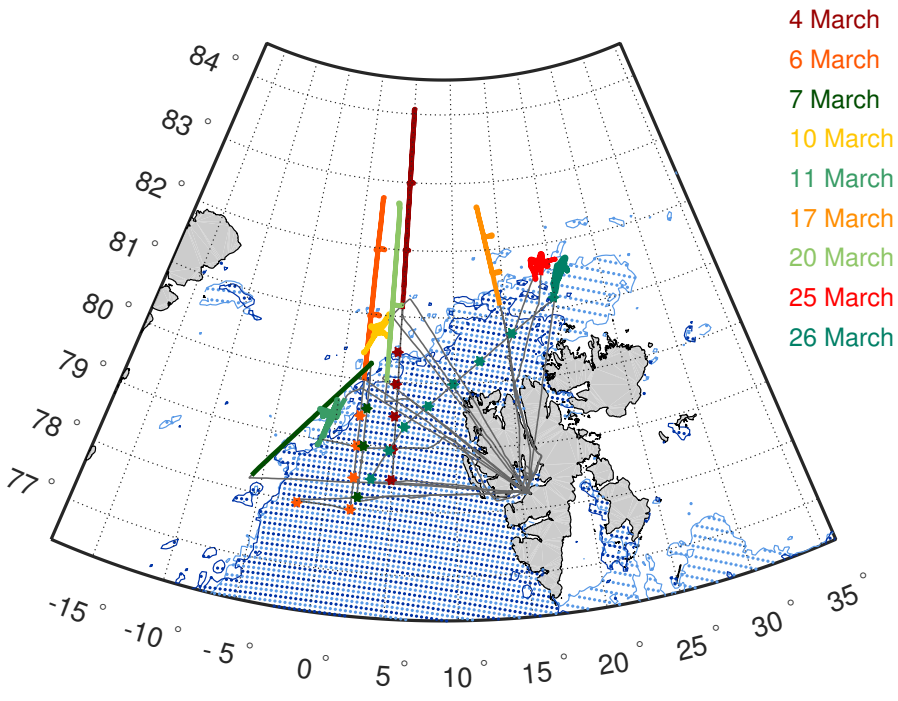

Figure 1.4: Locations of all STABLE flight sections used in this thesis. The asterisks mark the dropsonde positions. The ice edge on 4 March (light blue) and 26 March (dark blue) is shown as contour lines based on a 70 % threshold of the SSM/I-ASI ice concentrations (data from Ifremer/Cersat: http://cersat.ifremer.fr).

[1] Parts of this section have been published in Tetzlaff et al. (2015)

geographic position and orientation of the sea ice edge in March 2013. During the campaigns in the 1990s (Brümmer, 1997; Hartmann et al., 1997, 1999) the northern part of the ice edge was located close to 80° N with an east-west orientation, while in March 2013 a large ice free region was located north of Svalbard. Due to the large extent of this so-called Whaler's Bay polynya the ice edge was oriented in a northeast to southwest direction and was located as far north as 81.5° N at 20° E. Over the course of the month the ice margin moved further south and finally reached about 81° N at 15° E (Fig. 1.4). Our measurements enable us to study the impact of this different location of the ice edge on CAOs.

Coincidentally, March 2013 was also a time period of exceptionally high polar low activity associated with CAOs in this region. 13 polar lows were observed in the Greenland and Barents seas, which Rojo et al. (2015) found to be the highest monthly value since the beginning of their study period in 1999. Thus, the meteorological measurements obtained during STABLE might also be useful for future studies of the polar low developments during this month.

1.4.2 Aircraft instrumentation and data processing

The aircraft Polar 5, a reconverted Basler BT-67, was equipped with meteorological instruments that have been well tested on the previous aircraft of the AWI, Polar 2 and Polar 4, during numerous campaigns (e.g. Hartmann et al., 1994, 1997, 1999). Fast measurements of temperature, pressure, and the wind vector at 100 Hz enable the derivation of turbulent fluxes. With observed ground speeds of the aircraft between 40 and 75 m s^{-1}, depending on wind speed and direction, a spatial resolution of 0.4 to 0.75 m is obtained. The three wind components were derived using data from a 5-hole probe and the temperature was measured with a PT-100. The humidity was measured with two different sensors - a dew point mirror and a humicap. The dew point mirror measurements have a higher absolute accuracy than the humicap measurements, but a large response time. The humicap responds faster, but still not fast enough to resolve turbulent fluctuations. All these sensors were mounted on a 3 m long noseboom to minimize flow distortions by the aircraft (Fig. 1.5).

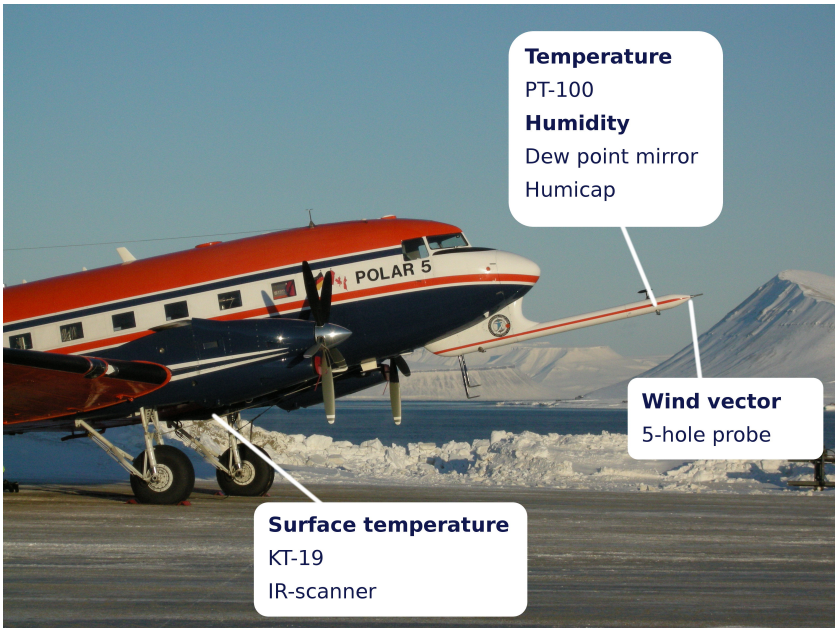

Figure 1.5: Photo of the Polar 5 aircraft of the Alfred Wegener Institute and locations of the meteorological sensors.

The height and position of the aircraft were derived from GPS and INS data. Since such data contain a slight uncertainty the flight heights were furthermore adjusted to the laser altimeter measurements when available. Surface temperatures were measured with a KT-19 radiation thermometer and an infrared scanner (IR-scanner). The KT-19 measures between 9.6 and 11.5 μm wavelength with an uncertainty of about 1 K, which is partly due to emissivity differences of the ice and water surfaces. Data were recorded at 50 Hz and, for the flights during STABLE, the integration time was set to 1 s to ensure a sufficient signal-to-noise-ratio. The IR-scanner measures across-track with a field of view of 90° separated into 1021 pixels. It has a spectral sensitivity of 8 to 12 μm and a scan rate of 20 Hz. Previously, it has been mainly used for oil spill remote sensing (Robbe and Zielinski, 2004). To increase the accuracy, the IR-scanner data are supported by the KT-19 data.

1.5 Thesis outline

This thesis is organized in three main chapters. A large part of content of these chapters is based on three studies that have already been published in the framework of this thesis. Another, smaller unpublished part supplements these investigations. Thus, the chapters form independent studies and include separate introduction, methodology and summary parts. Due to this fact, there is a partial overlap – especially concerning the literature review – of the contents between the different chapters.

Chapter 2 – Surface temperature impact on Arctic air temperatures
In this chapter we analyse the impact of a heterogeneous sea ice cover on atmospheric temperatures. For this purpose, we consider spatial variations of the surface temperature over the Arctic Ocean, which, under cloud free conditions, are mostly related to leads and polynyas that are covered by open water or thin ice. We use a Lagrangian box model to investigate the importance of spatial changes in surface temperatures for local atmospheric temperature changes and to quantify the spatial scale at which these changes are important. This chapter is based on Tetzlaff et al. (2013), which was published in *The Cryosphere*.

Chapter 3 – Influence of leads on the atmospheric boundary layer
This chapter deals with lead-atmosphere interactions. Based on the aircraft measurements during STABLE we analyse the boundary layer modification over four wide leads and calculate profiles of turbulent fluxes. This first part of the chapter is published as Tetzlaff et al. (2015) in the *Quarterly Journal of the Royal Meteorological Society*. In addition, we use the long flight legs during STABLE to derive a lead width distribution and to estimate the effect of leads on atmospheric temperatures on regional scales.

Chapter 4 – Cold air outbreaks: observations and modeling
A large part of this chapter is based on the dropsonde measurements of four CAOs during STABLE. We analyse the downstream development of meteorological variables and the ABL growth. Two of the four cases are influenced by the size of the Whaler's Bay polynya north of Svalbard, which has implications for the local climate in this region. The analysis of these two cases is published as Tetzlaff et al. (2014) in *The Cryosphere*. The measurements are supplemented by a brief excursion towards the modeling of CAOs. We use a 1D version of the mesoscale model METRAS to compare three different parametrisations of the vertical heat transport under typical conditions during CAOs and evaluate their performance for different vertical grid spacings.

Finally, **Chapter 5** summarizes the main results of this thesis and provides an outlook for possible future research.

Since the three published studies resulted from the work carried out by several authors, the author contributions are summarized in the following. A more detailed description can be found in Appendix A. In all studies Amelie Tetzlaff performed the calculations, plotted and analyzed the results, and wrote the manuscripts. The other authors contributed ideas for the conception of the studies and improved the manuscripts. Two of the manuscripts are based on aircraft measurements during the campaign STABLE. All authors of these manuscripts participated in the aircraft campaign and were involved in the flight planning and data acquisition.

2 Surface temperature impact on Arctic air temperatures

Surface temperatures over the Arctic Ocean are highly variable due to changes in sea ice concentration and sea ice thickness, as well as due to cloud radiative effects. This surface temperature variability also influences the near-surface temperatures in the atmospheric boundary layer. Different studies using data from Russian drifting stations in the Central Arctic suggest that under constant ice conditions the most important factors influencing the near-surface air temperatures are cloud cover and wind speed (Walsh and Chapman, 1998; Vihma and Pirazzini, 2005).

In this chapter we focus on the impact of changes in ice concentration and thickness on near-surface atmospheric temperatures and therefore consider only cloud-free cases. The main goal is to quantify the amount of 2-m air temperature variability that can be attributed to a heterogeneous surface temperature field in a region upstream of the considered location. Furthermore, we determine the extent of the upstream region at which these surface temperature changes are an important factor. To address this topic, we calculate the evolution of the near-surface air temperature along backward trajectories using a simple box model with satellite-derived sea ice concentration and surface temperature as input data. The derived temperatures are then compared to measured temperatures at three different sites. This chapter is – with marginal changes – identical to the content published in Tetzlaff et al. (2013).

2.1 Introduction

Sea ice plays an important role in the climate system. It insulates the ocean from the atmosphere and thus hampers the exchange of gases, moisture and heat. The strength of the insulation effect depends, however, on the sea ice thickness and sea ice concentration. Openings in sea ice act as windows and allow a direct ocean-atmosphere interaction with a large impact on the surface energy budget of the polar ocean and atmosphere. In order to obtain accurate fluxes, which determine the energy budgets, the sea ice concentration should be well represented in climate and weather prediction models. Also for reanalyses, a correct representation of ice concentrations is crucial for heat flux calculations (Inoue et al., 2011).

In this context the importance of accurate ice concentration measurements becomes apparent. Using remote sensing data from the Special Sensor Microwave Imager (SSM/I), uncertainties of at least 4 % arise for different algorithms in regions with high ice concentrations such as the Central Arctic (Andersen et al., 2007). Furthermore, Inoue et al. (2008) found an underestimation of the AMSR-E ice concentration of 7 % due to meltponds.

Several modeling studies have revealed a high sensitivity of atmospheric boundary layer (ABL) temperatures to the ice cover. Lüpkes et al. (2008b) used a one dimensional atmospheric model coupled with a sea ice model to investigate the influence of a change in ice cover on the ABL temperatures. They found that, under clear skies in winter and for ice concentrations close to 100 %, a change in ice concentration of 1 % can cause a change of the near-surface equilibrium

temperature by up to 3.5 K after two days of development. Valkonen et al. (2008) have shown that during a cold air outbreak in the Antarctic sea ice zone, the modeled 2-m air temperature varied by up to 13 K depending on the algorithm applied to derive the sea ice concentration. Parkinson et al. (2001) found that uncertainties in total ice concentrations of ± 7 % can cause local temperature changes exceeding 6 K in polar regions and changes in global annual mean temperatures of about 0.3 K using a global climate model.

Leads represent a large source for surface temperature variability. Different characteristics of their impact on the ABL have been measured, such as the annual cycle of sensible heat fluxes (Persson et al., 2002) and the development of sensible heat fluxes on the downwind side of leads (Ruffieux et al., 1995) or different convection regimes over leads (Andreas and Cash, 1999). Heat fluxes over ice and open water areas have also been obtained from aircraft measurements (Fiedler et al., 2010) and have been estimated using surface temperatures from the Advanced Very High Resolution Radiometer (AVHRR) (Meier et al., 1997; Overland et al., 2000). Heat and moisture fluxes from polynyas have been estimated using data from the Special Sensor Microwave Imager (SSM/I) (Martin et al., 2004) and the Advanced Microwave Scanning Radiometer for EOS (AMSR-E) (Boisvert et al., 2012).

The goal of the present study is to supplement the above mentioned studies on the impact of sea ice variability by studying the impact of spatial surface temperature variability on the air temperature at a given location. For this purpose, backward-trajectories arriving at three stations in the Arctic are calculated from reanalysis data. Ice concentrations and ice surface temperatures along the trajectories are prescribed from satellite data. The mean ice surface temperature along the trajectories, as well as the air temperature and sensible heat fluxes obtained by a simple Lagrangian box model are then compared to the 2-m air temperatures measured at the stations.

The application of these methods aims to obtain answers to the following questions: How important are spatial changes in surface temperatures in the high ice concentration regime for local atmospheric temperature changes? To what spatial extent do heterogeneous surface temperatures influence the air temperature variability? How strong do the results depend on the choice of different reanalyses for the calculation of trajectories and on different sea ice concentration products? A description of the data is given in Sect. 2.2 and the methods are described in Sect. 2.3. The results are presented in Sect. 2.4, followed by a discussion (Sect. 2.5) and conclusions (Sect. 2.6).

2.2 Data

For the present study, hourly 2-m air temperatures from three different stations in the Arctic are used. The first two stations are Barrow (Alaska) and Alert (Canada) (Fig. 2.1). Only the coldest months with the largest ice extent are used. For the present analysis, these are February and March for Barrow (2003–2008) and February through April for Alert (2003–2006). These two stations are supplemented by temperatures measured at the French schooner Tara which drifted through the Central Arctic in 2006–2007 during a campaign which was part of the project DAMOCLES (Developing Arctic Modeling and Observing Capabilities for Long-term Environmental Studies) (Vihma et al., 2008). As the thermal differences between sea ice and open water surfaces are small in summer, only one month (April 2007) of Tara data was used in the analysis. Despite the short timeseries, Tara provides invaluable data since measurements from the Central Arctic are sparse.

Backward-trajectories arriving at the stations are calculated from the 10 m-wind fields of the Japanese 25-year reanalysis (JRA) (Onogi et al., 2007) and of the European Centre for Medium-Range Weather Forecasts (ECMWF) reanalysis (ERA-Interim) (Dee et al., 2011). Both reanalyses are available every 6 h with a resolution of 1.125 and 1.5° (and 0.75°) for JRA and

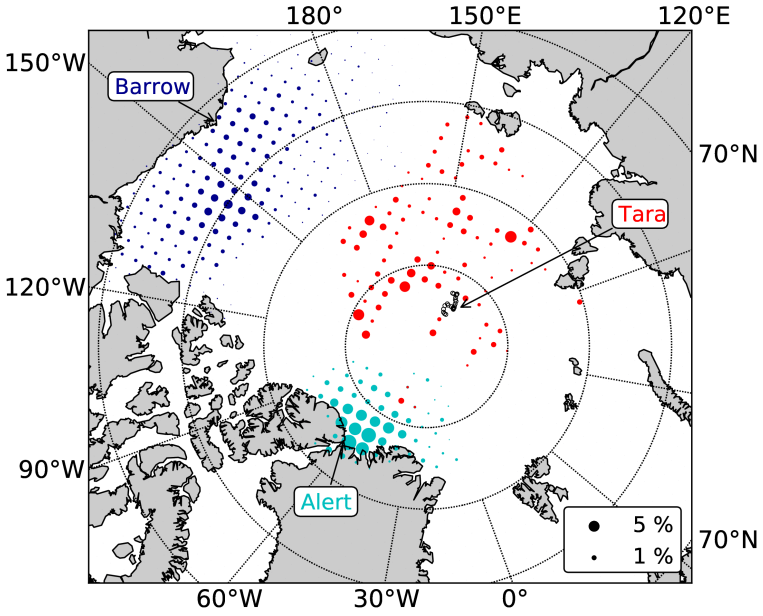

Figure 2.1: Distribution of the trajectory starting points upwind of Alert (light blue), Barrow (dark blue) and Tara (red) for JRA and ERA combined. The grid cell size is 100 km and the size of the circles indicates the relative frequency. The arrows mark the in situ stations and the Tara drift track in April 2007.

ERA, respectively. Sea level pressure fields from both reanalyses are used to calculate potential temperatures. The ERA forecast runs also provide ABL depths every 3 h.

The Lagrangian box model following the trajectories requires ice concentration and ice surface temperature as input data. Four different ice concentration data sets are used. These are the Special Sensor Microwave Imager (SSM/I) data with a resolution of 12.5 km (Kaleschke et al., 2001) and AMSR-E with a resolution of 6.25 km (Spreen et al., 2008) starting in June 2002. Both ice concentrations are derived using the ARTIST sea ice (ASI) algorithm (Kaleschke et al., 2001) and are available through the CliSAP-Integrated Climate Data Center (ICDC). In addition, ice concentrations from AMSR-E using the NASA Team 2 (NT2) and the Bootstrap algorithm are used (Cavalieri et al., 2004). Both have a grid spacing of 12.5 km and are provided by NSIDC. Abbreviations for the different combinations of reanalyses and ice concentration data are given in Table 2.1 and are labeled as a sequence of reanalysis, sensor and algorithm.

Table 2.1: Abbreviations used for the different combinations of reanalyses and ice concentration data sets.

Reanalysis	Sensor	Algorithm	Abbreviation
JRA	SSM/I	ASI	JSA
JRA	AMSR-E	ASI	JAA
JRA	AMSR-E	NASA Team 2	JAN
JRA	AMSR-E	Bootstrap	JAB
ERA	SSM/I	ASI	ESA
ERA	AMSR-E	ASI	EAA
ERA	AMSR-E	NASA Team 2	EAN
ERA	AMSR-E	Bootstrap	EAB

Sea ice surface temperatures are obtained from the MOD29 (MODIS/Terra Sea Ice Extent and IST Daily L3 Global 4 km EASE-Grid Day) data set by Hall et al. (2006). Data have been available since 24 February 2000 with a resolution of 4 km. They are aggregated to a 12.5 km grid. The measured MOD29 temperature, however, represents the surface temperature of a whole pixel and is also influenced by open water areas in that pixel. Therefore, the MOD29 surface temperatures are linearly weighted using the ice concentration products to obtain a better estimate of the actual ice surface temperatures. MOD29 data contain gaps, mainly due to clouds. Considering all trajectories over ice, there are 8 % missing values for Barrow, 20 % for Alert and 32 % for Tara. Since positive cloud radiative forcing changes ice surface temperatures considerably, only trajectories without data gaps are considered. However, this constraint leaves too few considered cases for Tara and hence also cases with less than 10 % missing values are allowed. Here, the missing values are replaced using a linear interpolation along the trajectory.

2.3 Methods

2.3.1 Backward-trajectories

Two-dimensional trajectories are calculated based on the 10 m-wind fields of the JRA and ERA reanalyses. A time step of 1 h is used for the calculation and the velocity at a certain point is obtained by linearly weighting the wind velocities of the surrounding four points according to their distance in spherical coordinates. Only those trajectories are considered, which do not pass over land along their path.

2.3.2 Statistical analysis method

The influence of surface temperatures along the trajectories on ABL temperatures is examined using three different methods. As a first approach, the mean ice surface temperatures along the trajectories are compared to the in situ 2-m air temperatures at the stations (IST method) by calculating correlation coefficients r, root mean squared errors (RMSE) and biases. This approach does not account for the impact of the spatial surface temperature variability along one trajectory. However, the spatial variability of the ice surface temperatures between trajectories with different paths is accounted for. Since the MOD29 ice surface temperatures are given as daily fields, the observed variability during one day is only due to spatial differences caused by different trajectory paths and not due to temporal changes of the ice surface temperature. For time periods longer than one day, there is also the day-to-day variability of the ice surface temperatures. It can be shown by a simple statistical analysis that the impact of this variability on correlation coefficients is small compared with the spatial variability caused by different trajectory paths.

The second approach includes the influence of the spatial surface temperature variability along each trajectory by its impact on the air temperature evolution along the trajectories which is calculated using a simple box model (Sect. 2.3.3). In the following, this method is called the air temperature method (AT). Air temperature changes are only caused by sensible heat fluxes from ice or open water areas and by radiative cooling in the model. The squared correlation coefficient between the modeled and the observed 2-m air temperature at the stations gives the amount of air temperature variability which is explained by the model, i.e. by changes in surface sensible heat fluxes. The spatial extent at which surface temperature changes are important for air temperature variability is then the radius of impact. It is determined by analyzing the changes of the explained variances as a function of the trajectory length.

Another possibility to get information about the radius of impact can be based on the in-

vestigation of the temperature changes along trajectories caused by heat fluxes. In this third approach, the differences between the observed temperatures at the trajectory starting and ending points (the latter are Barrow, Alert and Tara) are correlated with the mean sensible heat fluxes along the trajectories. In the following, this method is called the temperature variability method (TV). The sensible heat fluxes are obtained from the same simple box model as used for the AT method. For both the AT and the TV method, the air temperature at the trajectory starting point is assumed to equal the ice surface temperature at this location. Results of IST and AT are presented in Sect. 2.4.4 while TV results are added in Sect. 2.4.5 only.

For all methods, 95 % confidence intervals for the correlations are obtained using a Fisher's z-transformation (von Storch and Zwiers, 1999). In addition, biases and root mean squared error values (RMSE) between the temperatures are calculated. The significance of these values can be tested using a student-t test (von Storch and Zwiers, 1999). These significance tests require the degrees of freedom. Since hourly temperature measurements are not statistically independent, the degrees of freedom are not equal to the number of observations. Therefore for the determination of the degrees of freedom, lag correlations of the in situ temperatures are calculated. The time, where the 95 % confidence interval of the lag correlation reaches 1/e, gives the time scale at which observations become independent from each other. These are 27 h for Barrow, 23 h for Alert and 10 h for Tara. Thus, the degrees of freedom are not equal to the actual number of measurements within the time series but are reduced using these time scales.

2.3.3 Box model

For the AT and TV methods, a simple box model is used to investigate the Lagrangian change of air temperatures along trajectories. The dominant source term in the prognostic equation for potential temperature is assumed to be the turbulent sensible heat flux at the surface. Radiative cooling of the air column is also accounted for assuming a constant cooling rate c of 2 °C per day as in Vihma et al. (2003). Contributions from other processes such as condensation or cloud radiative effects are only indirectly taken into account by their impact on the surface temperature which is prescribed from observations. Therefore, the balance equation of temperature becomes

$$\frac{\mathrm{d}\theta(z)}{\mathrm{d}t} = -\frac{\partial\overline{w'\theta'}(z)}{\partial z} - c \cdot \exp(-\frac{z}{z_c}), \tag{2.1}$$

where θ is the potential temperature of the air, $\overline{w'\theta'}$ is the turbulent sensible heat flux and the height z_c is 600 m. Equation 2.1 is integrated over the ABL height H which is represented as a box of constant height in the Lagrangian model. The box travels along a trajectory calculated from reanalysis data (Sect. 2.3.1).

In general, the solution of Eq. 2.1 depends on the specified temperature profile. However, we will demonstrate in the following that the solutions are identical for a well mixed ABL with height constant θ and for a more general power law temperature profile. This holds for the assumption that both the difference between the temperatures at 10 m height and at the ABL top and the mixed layer height H are not depending on time.

The temperature profile above the reference height of $z_{\mathrm{ref}} = 10\,m$ can be expressed as a power law:

$$\theta(z) = (\theta(H) - \theta(z_{\mathrm{ref}})) \left(\frac{z - z_{\mathrm{ref}}}{H - z_{\mathrm{ref}}}\right)^b + \theta(z_{\mathrm{ref}}). \tag{2.2}$$

This relationship includes a linear temperature profile for an exponent $b = 1$ and a well mixed ABL for $b = 0$. With the assumption of a constant ABL thickness H, the time derivative of Eq.

2.2 is

$$\frac{\mathrm{d}\theta(z)}{\mathrm{d}t} = \frac{\mathrm{d}(\theta(H) - \theta(z_{\mathrm{ref}}))}{\mathrm{d}t} \left(\frac{z - z_{\mathrm{ref}}}{H - z_{\mathrm{ref}}}\right)^{b} + \frac{\mathrm{d}\theta(z_{\mathrm{ref}})}{\mathrm{d}t} \,. \tag{2.3}$$

When the temperature difference $(\theta(H) - \theta(z_{\mathrm{ref}}))$ is assumed to be constant in time, the first term on the right hand side of the equation vanishes, so that θ and θ_a can be replaced by $\theta(z_{ref})$ in Eq. 2.1. With these assumptions the solutions of Eq. 2.1 are always the same for any profile of the form of Eq. 2.2. However, we use the well mixed case in Sect. 2.3.3 since for $b = 0$ the assumption H =const. is not necessary. This consideration is relevant since Eq. 2.1 is only used in its integrated form over H in the following. Furthermore, a constant flux layer is assumed below the reference height of $z_{\mathrm{ref}} = 10\,\mathrm{m}$, with logarithmic profiles of wind and potential temperature.

To verify the assumption of a well mixed ABL radiosonde data are analyzed. Since soundings at Tara during the considered period are sparse and the soundings at Alert are conducted at higher elevations than the temperature measurements, only data from Barrow are considered. Soundings from the University of Wyoming dataset are used which are available every 12 h. Only those soundings with wind direction from the ice are considered. The stratification is expressed in terms of the Richardson number (Ri) in the lowest 30 m as a function of wind speed (Fig. 2.2). For wind speeds between 2 and $4\,\mathrm{m\,s^{-1}}$ about 90 % of the Ri numbers are below the critical value of 0.25 and 75 % below 0.1. Therefore, the assumption of a well mixed ABL seems to be valid for wind speeds above $3\,\mathrm{m\,s^{-1}}$. In addition, the few sounding from Tara all show a well mixed ABL. Therefore, only trajectories with 90 % of the wind speeds above $3\,\mathrm{m\,s^{-1}}$ are considered. This limit is lowered to 80 % of the wind speed above $2\,\mathrm{m\,s^{-1}}$ for Alert since too few cases remain if the stricter criterion is applied.

The fluxes of sensible heat over ice and water are expressed as bulk formulations and weighted with the ice concentration so that the evolution of the temperature averaged over the boundary layer depth H is calculated as

$$(H - z_{\mathrm{ref}})\frac{\mathrm{d}\theta_{\mathrm{a}}}{\mathrm{d}t} = c \cdot z_{\mathrm{c}} \cdot (\exp(-\frac{H}{z_{\mathrm{c}}}) - \exp(-\frac{z_{\mathrm{ref}}}{z_{\mathrm{c}}})) + A|\vec{u}|C_{\mathrm{si}}(\theta_{\mathrm{i}} - \theta_{\mathrm{a}}) + (1 - A)|\vec{u}|C_{\mathrm{sw}}(\theta_{\mathrm{w}} - \theta_{\mathrm{a}}), \tag{2.4}$$

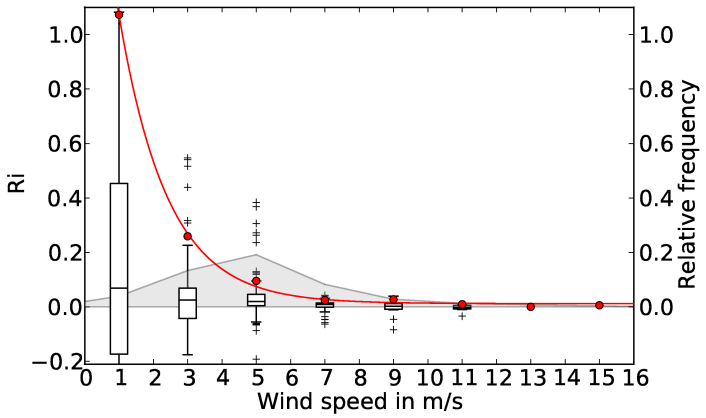

Figure 2.2: Boxplot of Richardson numbers in the lowest 30 m for Barrow derived from radiosonde data in wind speed bins of $2\,\mathrm{m\,s^{-1}}$ (box: quartiles, whiskers: 1.5 times the inner quartile range). The red line is a polynomial fit to the 90 % quantiles and the grey shaded area is the frequency distribution of wind speed.

where θ_i, θ_w and θ_a are the potential temperatures of ice, water and air, respectively. A is the ice concentration and $|\vec{u}|$ is the wind speed at z_{ref} =10 m. It was assumed here that the heat flux at $z = H$ is zero and thus no vertical entrainment is present. The solution of Eq. (2.4) is based on an explicit Eulerian numerical scheme with a relatively large time step Δt of 15 min. However, for moderate wind speeds a reduction to 1 minute caused changes in the order of 0.2 °C only, so that this impact is negligible compared to other uncertainties. The water temperature T_w is permanently at the freezing point of −1.9 °C. C_{si} and C_{sw} are the heat transfer coefficients for ice and water, respectively. They are calculated using the Monin-Obukhov similarity theory as

$$C_s = \frac{\kappa^2}{(\ln(\frac{z}{z_0}) - \Psi_m(\frac{z}{L}))(\ln(\frac{z}{z_T}) - \Psi_h(\frac{z}{L}))}, \tag{2.5}$$

where L is the Obukhov length, κ the von Kármán constant and the Ψ-functions for momentum and heat are chosen according to Grachev et al. (2007). The surface roughness lengths z_0 are assumed to be constant with values of 1 mm for ice and 0.1 mm for water (as often used, for example by Lüpkes et al. (2008b)) and the roughness lengths for heat z_T are one tenth of it, respectively. L is calculated iteratively using

$$L = \frac{u_*^2 \bar{\theta}}{\kappa g \theta_*} \tag{2.6}$$

which neglects the influence of humidity. It is inserted into the turbulent scaling parameters for temperature and velocity

$$\theta_* = \kappa(\theta(z) - \theta_s)(\ln(\frac{z}{z_0}) - \Psi_h(\frac{z}{L}))^{-1} \tag{2.7}$$

$$u_* = \kappa|\vec{u}|(\ln(\frac{z}{z_0}) - \Psi_m(\frac{z}{L}))^{-1} \tag{2.8}$$

after Pielke (2002) which are then used to obtain new values of L. $\bar{\theta}$ is the mean potential temperature of the air.

The transfer coefficients are calculated for the reference height of $z_{ref} = 10\,m$. For comparison with the in situ 2-m air temperatures the potential temperatures are reduced to a height of 2 m, assuming a logarithmic temperature profile below 10 m. Air temperatures are then obtained from the 2 m potential temperatures using the sea level pressure from the reanalysis.

Two different approaches are used for the boundary layer depth. In the first approach it is set to a constant value. Two different values are applied which are typical for the Arctic ABL (Lüpkes et al., 2012b). The first one, 350 m, was, for example, measured over a flaw lead polynya in the Canadian Archipelago by Raddatz et al. (2011). The second one, 100 m, is close to often observed values (reported e.g. by Tjernström and Graversen (2009) for the SHEBA project north of Alaska, by Hartmann et al. (1997) for the marginal ice zone or by Lüpkes et al. (2010) for the inner Arctic Ocean). Using larger ABL depths would increase the e-folding time (see below) and the model output temperatures would not differ much from the initial temperatures. There were also more than 25 % surface-based inversions in February and March during SHEBA. However, during the cold seasons, leads and polynyas that are passed by the trajectories cause vertical mixing due to convection and thus a deepening of the boundary layer. Therefore, no constant ABL depth smaller than 100 m is used.

As a second approach, ABL depths are taken from the ERA Interim 3-hourly forecast runs. Values from the four closest points are linearly interpolated to the trajectory positions. A growing ABL may cause a downward heat flux from the inversion layer. The sensitivity to this entrainment through the capping temperature inversion has also been tested by using a simple approach

relating entrainment to the surface heat fluxes but was found to be negligible relative to other restrictive assumptions and is thus neglected in Eq. 2.4.

The initial air temperature is set equal to the ice surface temperature at the trajectory starting point. The impact of this simplified assumption is small when the model is run long enough to reach an equilibrium temperature, which is independent from the initial temperature. The e-folding time t_e required to reach a stationary state can be calculated on the basis of Eq. 2.4, when constant transfer coefficients are assumed, as

$$t_e = \frac{H}{|\vec{u}|(A \cdot C_{si} + (1 - A) \cdot C_{sw})}. \tag{2.9}$$

t_e is a function of the boundary layer depth H, the wind speed $|\vec{u}|$ and the ice concentration A. To estimate a maximum e-folding time, a wind speed of $5\,\mathrm{m\,s^{-1}}$, an ice concentration of 95 % and a ABL depth of 350 m are assumed. The turbulent transfer coefficients are calculated assuming constant potential temperatures of $-20\,^{\circ}\mathrm{C}$ for air and $-25\,^{\circ}\mathrm{C}$ for ice. This gives an e-folding time of 27 h, corresponding to 480 km length. Therefore, the trajectory length should be larger than 27 h to ensure that the initial conditions have a small impact. However, in most considered cases, the e-folding time is much smaller and already after 2 h the modeled temperature only differs by $0.5\,^{\circ}\mathrm{C}$ from the equilibrium temperature. Nevertheless, the development along trajectories of 30 h is considered.

2.4 Results

2.4.1 Trajectory positions

The trajectories calculated using the different reanalyses show large inconsistencies. Examples are shown in Fig. 2.3. The paths of all trajectories are compared by calculating the mean spatial distances between JRA and ERA (1.5°) trajectories, which differ for the three stations. Mean

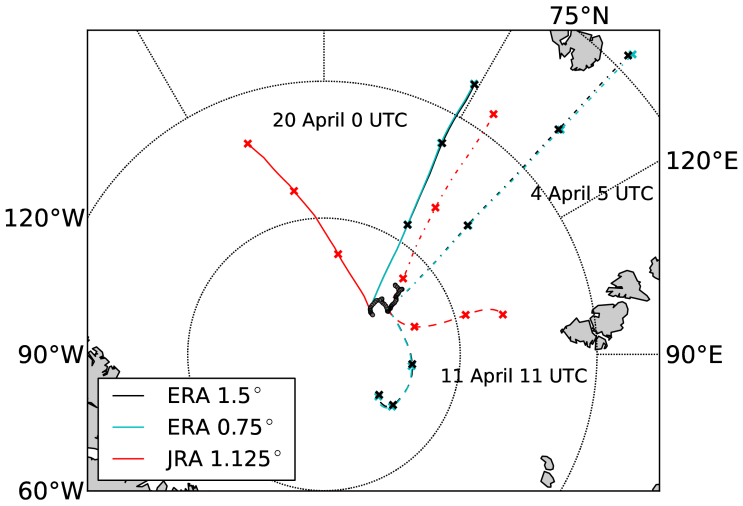

Figure 2.3: Three exemplary sets of trajectories arriving at Tara in 2007 calculated using ERA Interim with two different resolutions and JRA. The temporal differences between crosses are 10 h. The pairs of ERA trajectories are nearly overlapping so that the differences between the trajectories of both ERA data sets are invisible.

separations after 10 h are about 50 km for Barrow, 70 km for Alert and 90 km for Tara. The differences between the three stations are even larger after 30 h, ranging from 120 km for Barrow to 380 km for Tara. This shows a large inconsistency of the near-surface wind fields of the reanalyses over Arctic sea ice, especially in the Central Arctic. The large uncertainties in the trajectory positions cause large uncertainties in the estimation of the impact of remote areas but in the near environment of about 100 km the uncertainties are on average much smaller.

Comparing ERA Interim trajectories using resolution of 0.75 and 1.5° reveals only small mean separations of less than 20 km after 30 h. Figure 2.3 also illustrates that using a higher resolution hardly changes the positions of ERA trajectories. Therefore, the lower resolution is used for the following calculations.

2.4.2 An example of evolution along a single trajectory

First, an example is presented showing the development of the air temperature and sensible heat fluxes obtained using the box model along an individual trajectory. It is the trajectory arriving at Tara on 20 April 2007 at 12 UTC (Fig. 2.4), which has AMSR-E ASI ice concentrations between 85 and 99 % along the path. The air parcel moves about 750 km northward in 30 h. The ice surface temperature varies between −24 and −14 °C (Fig. 2.5). The sensible heat fluxes do not exceed 200 $\mathrm{W\,m^{-2}}$ over water because air-sea temperature differences are 17 °C at maximum and the wind speed does not exceed 7 $\mathrm{m\,s^{-1}}$. The resulting net heat flux is positive in the first 18 hours with small values below 30 $\mathrm{W\,m^{-2}}$ which causes an increase of the potential temperature of 4 °C. At t =-12 h a decrease of the ice surface temperature by 10 °C causes negative net heat fluxes of up to −50 $\mathrm{W\,m^{-2}}$ and a decrease of the air potential temperature of 4 °C in 5 hours. The resulting modeled 2-m temperature at Tara of −16.8 °C agrees well with the measured value within 0.1 °C.

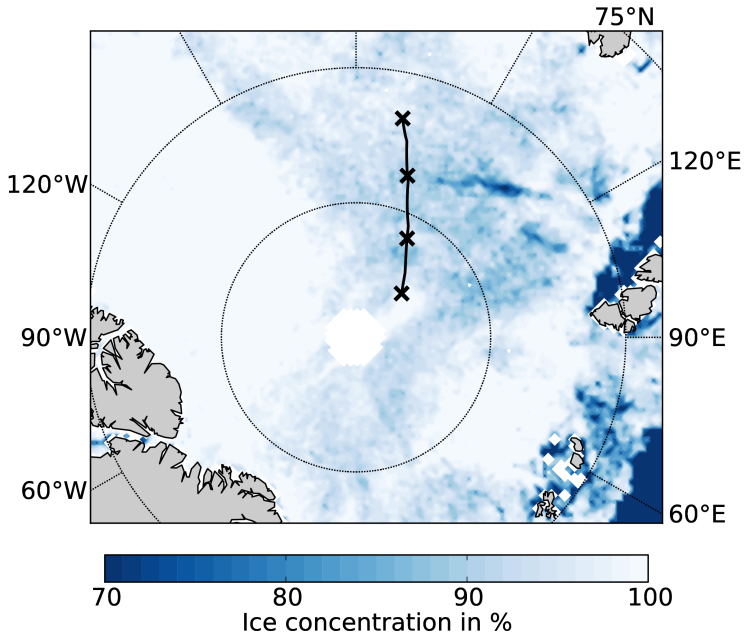

Figure 2.4: AA ice concentration on 20 April 2007 and ERA-trajectory from 20 April 2007 12 UTC during the last 30 hr arriving at Tara (black line).The differences between crosses are 10 h. At this time Tara is located at 87.6° N, 134.9° E.

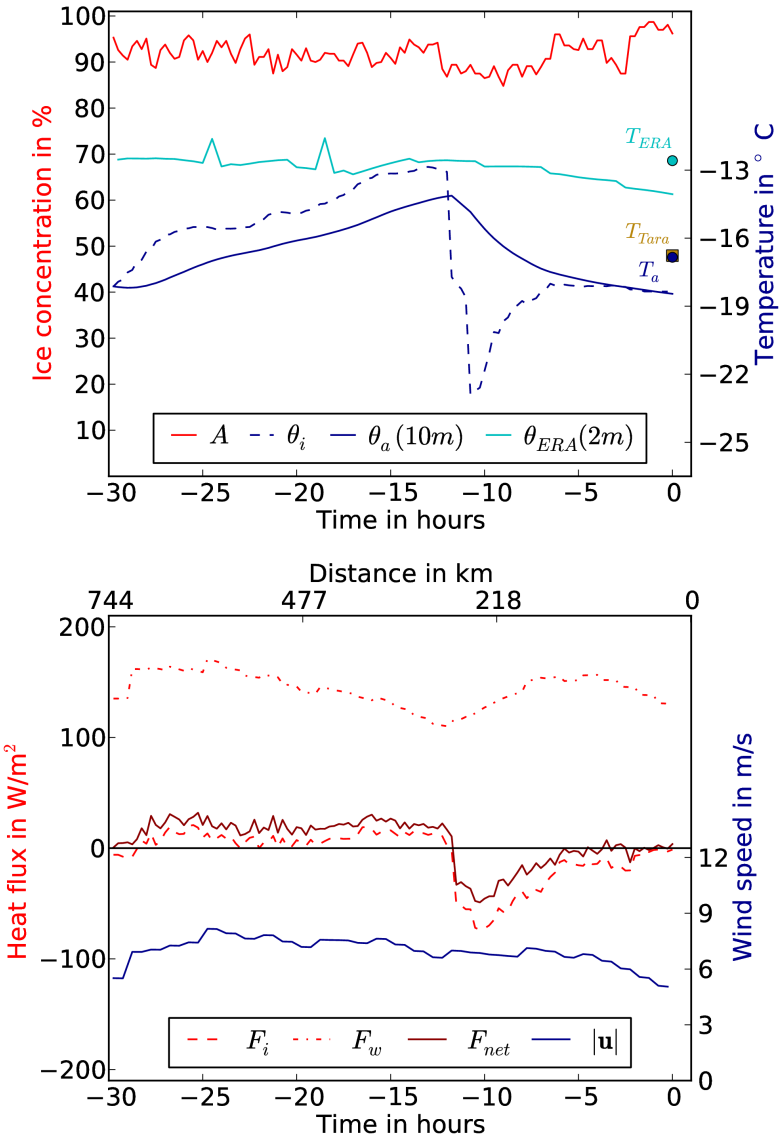

Figure 2.5: Time series of the model input and output data on 20 April 2007 12 UTC for Tara: AA ice concentration (A), ice surface potential temperature (θ_i), air potential temperature at 10 m (θ_a) (lines) and 2-m air temperature at Tara (symbols) observed and calculated from the predicted 10-m potential temperature. Furthermore, sensible heat flux from ice (F_i), water (F_w) and the resulting net flux (F_{net}), and ERA surface wind speed (u) and 2-m potential temperature (θ_{ERA}). The ABL depth is 350 m.

The corresponding ERA 2-m temperatures are too high along the trajectory path with a value of −12.6 °C arriving at Tara. This example shows the important role of the specified surface boundary conditions of a model on the calculated air temperature evolution. While the box model, which uses ice concentrations and ice surface temperatures derived from remote sensing data, reproduces the measured 2-m air temperature quite well, the temperature of the reanalysis is about 4 °C too high. This is probably due to the sea ice boundary conditions in ERA-Interim with fixed values for the ice thickness of 1.5 m (White, 2006) and for the ice concentration of 100 % north of 82.5° N (Inoue et al., 2011) which reduce the surface temperature variability.

2.4.3 Ice concentration along all trajectories

In the following, the geographical locations of the trajectories and the corresponding ice conditions are examined to obtain a basis for further discussions of differences between the results for different stations. Abbreviations for ice concentrations used in this section are according to Table 2.1 but without the prefix for the reanalysis. The frequency distributions of ice concentrations obtained from remote sensing data for the trajectories resulting from ERA or JRA wind fields are very similar. Therefore, the distributions for both reanalyses are combined in Fig. 2.6.

Most trajectories arriving at Alert originate from the Central Arctic north of Greenland (Fig. 2.1) where high ice concentrations are present due to convergent ice drift. Comparing the distribution of ice concentrations along all trajectories, shows that more than 95 % of the time ice concentrations are 98 % or higher for the three AMSR-E data sets (Fig. 2.6). SSM/I ASI has a heavier tail with about 30 % of the values between 90 and 98 %. Barrow's trajectories originate from the Beaufort Sea (Fig. 2.1) where divergences in the Beaufort Gyre decrease the ice concentration. The frequency distribution also reveals lower ice concentrations than for Alert (Fig. 2.6) with a total of 10 % (AA) up to 50 % (SA) below 98 %.

The considered trajectories arriving at Tara originate from the Central Arctic and the Laptev Sea (Fig. 2.1). Ice concentrations show a larger variability and lower values than for Alert and Barrow. For Tara, during 75 % of the cases, the ice concentration values are below 95 % for SA. The difference between the ice concentration data sets is largest for Tara with 40 % of the total ice concentrations below 97 % for AA, 25 % below 97 % for AB and almost 100 % above 97 % for AN. While AB and AN show only small changes in the frequency distributions of ice concentration for the three stations, SA and AA show the highest ice concentrations for Alert and the lowest ones for Tara.

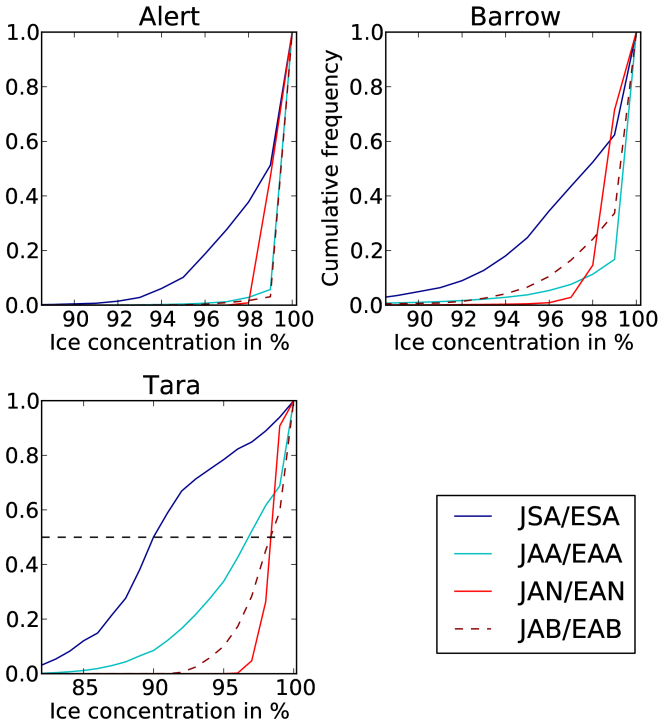

Figure 2.6: Cumulative frequency distribution of ice concentrations along the trajectories (ERA and JRA combined) for different ice concentration data sets for Alert, Barrow and Tara.

2.4.4 Results for the ensemble of trajectories

The correlations between the observed 2-m air temperatures and the mean ice surface temperatures along the trajectories (IST) and modeled temperatures (AT) are positive, exceeding values of 0.6, and significant at the 95 % level for all combinations of reanalyses, ice concentration data sets and ABL depths. The results of the AT method obtained with different ice concentrations show differences in the order of 1 to 3 % but overlapping confidence intervals. Since the sensitivity of the results to different ice concentration data sets is very small only exemplary results (AA) are presented.

Using the AT method, the highest explained variances exceeding 90 % are found for Alert. There, the scatter plot shows a good agreement between model and in situ temperatures for EAA (Fig. 2.7). For ERA, explained variances are about 6 % higher than for JRA (Fig. 2.8). The best results are obtained using an ABL depth of 100 m, with biases of −0.6 °C (ERA) and −1.4 °C (JRA) and RMSE of 2.1 °C (ERA) and 3.1 °C (JRA). Using ERA ABL depths gives similar results while using 350 m increases the negative biases to −1.8 °C (ERA) and −2.2 °C (JRA). The explained variance based on the IST method is 89 % using ERA and 86 % using JRA, which is the same order as the model results. Biases and RMSE using the IST method are larger than those from the AT method.

Explained variances for Barrow are smaller than for Alert ranging between 61 and 74 % for the AT method and between 46 and 51 % using the IST method (Fig. 2.8). In all cases, values for a ABL depth of 350 m are up to 10 % higher than for 100 m and about 5 % higher than for the run with ERA ABL depths. Temperature biases are positive in the order of 1.5 (350 m) to 3.5 °C (100 m) and the RMSE range from 3 to 4 °C. Biases from the IST method are negative with values around -0.8 °C.

Tara shows the largest sensitivity to different reanalyses for the AT method. Explained variances are about 70 % using JRA trajectories with RMSE of about 3.6 °C (Fig. 2.8). Using ERA trajectories gives larger explained variances in the order of 80 % with RMSE of 3.3 °C (100

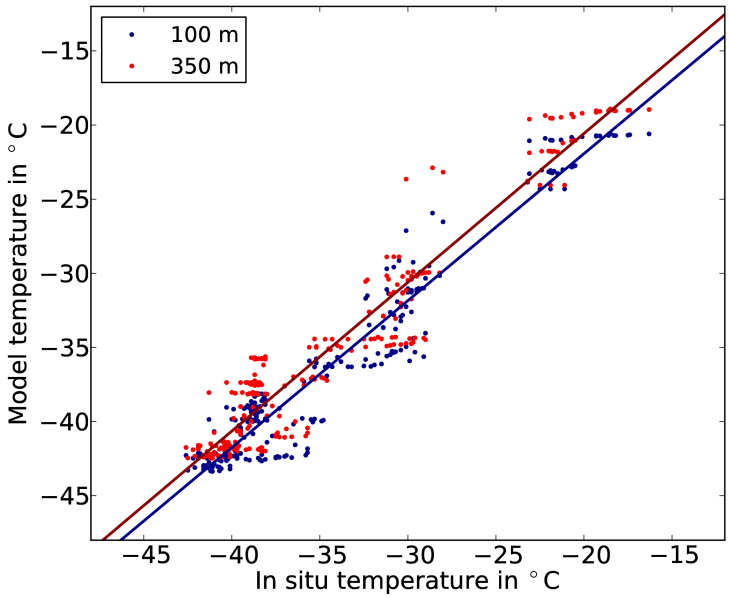

Figure 2.7: Scatter plot of in situ and modeled temperatures (AT method) in °C for Alert 2003-2006 for EAA. The colors denote results for different ABL depths and the lines are the corresponding regression lines.

m) to 3.9 °C (350 m). For both reanalyses higher explained variances are obtained using an ABL depth of 100 m. The variance from the IST method is about 20 % smaller than the explained variance from the AT method. The RMSE are of the same order and the bias based on the IST method of −1.7 °C is even smaller than the biases based on the AT method of about −2.5 °C.

In addition, ERA ABL depths are compared with the two constant values. For Barrow, most ERA derived ABL depths can be found around 150 m (Fig. 2.9) but the distribution has a tail with some ABL depths even exceeding 500 m. This explains why results of the AT method are better for ABL depths of 350 m than for 100 m. In Alert, ABL depths below 100 m are present in the ERA data and the biases and RMSE are also lower for a ABL depth of 100 m. These results are

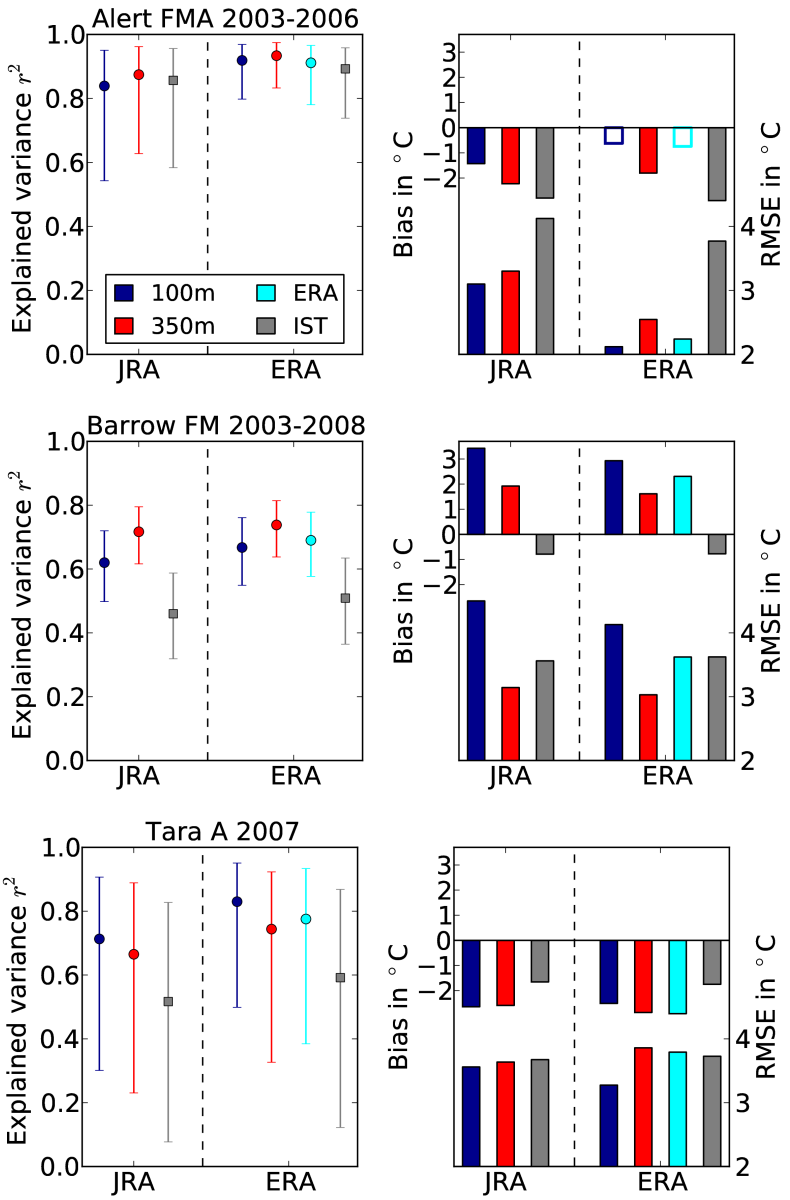

Figure 2.8: Explained varances between observed 2-m air temperatures at the stations and modeled temperatures (AT method, colored), as well as mean ice surface temperatures along the trajectories (gray) with 95 % confidence intervals (left), bias and RMSE (right) for Alert (upper), Barrow (middle) and Tara (lower) using AA ice concentrations. The colors denote the ABL depths. The blank bars are not significant at the 95 % level.

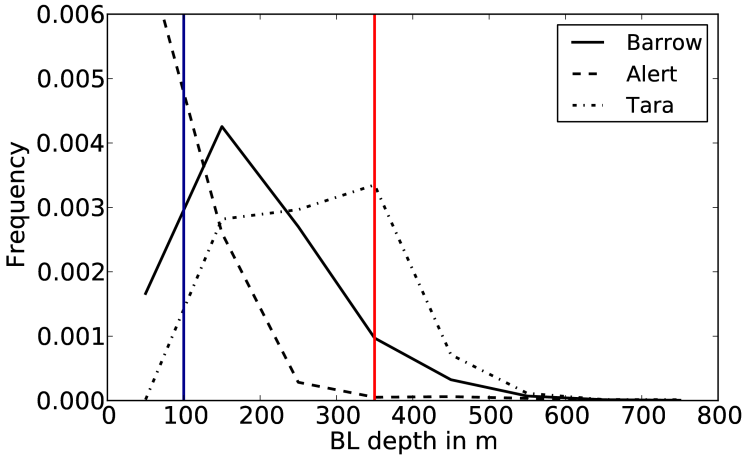

Figure 2.9: Frequency distribution of ERA-interim ABL depths for Barrow, Alert and Tara. The two constant ABL depths that are also used are marked with colors.

in line with the expected results from the ice concentration distributions. Shallow ABLs develop over completely ice covered areas, as observed for Alert, whereas more open water areas, as for Barrow, cause a deepening of the ABL. The ABL depths are the largest at Tara. Here, the most frequent values range from 100 to 400 m. However, explained variances using the AT method are larger for a ABL of 100 m than for a BL of 350 m for both reanalyses.

2.4.5 Radius of impact

The above analysis does not yet answer the question concerning the dominant horizontal scale R (or the corresponding time scale R_t) influencing the 2-m air temperature. Therefore, in addition to the previous studies, results are considered as a function of the trajectory length which is reduced stepwise from 30 to 2 h. Fig. 2.10 shows results obtained using the AT and the IST methods corresponding to the prescribed trajectory length. Results are exemplarily discussed for JAA, results from ERA differ only slightly.

The clearest results are those for Barrow. There, the explained variances obtained using the AT method are increasing by about 6 % with increasing trajectory length from 2 to 10 h while they remain nearly constant from 10 to 30 h. The corresponding curve based on IST shows a different behavior with a maximum of explained variance for 5 h. For the IST method the explained variance decreases for distances larger than R or for times larger than R_t, because the surface temperatures in remote areas are not any more correlated with the considered location. A similar decrease for the explained variance of the AT method is not seen, because all trajectories starting at time $t > R_t$ pass also the region close to the location with large impact.

For Barrow, biases and RMSE decrease by about 1 °C for trajectory lengths between 2 and 10 h and remain nearly constant for larger lengths using the AT method. The minimum RMSE using the IST method is found for trajectory lengths of about 10 to 20 h. The bias from IST increases for shorter trajectory lengths from −1 to 4 °C. Both methods suggest a value R_t =10 h for the characteristic time scale which corresponds to $R \approx 180\,km$ for an average wind speed of 5 m s^{-1}.

For Alert, the results using the AT method improve only slightly for longer trajectories. Distinct changes can be found in the curves for bias and RMSE of the IST method, which suggest R_t =10 h, as found for Barrow. Results for Tara with respect to R values are ambiguous. The curves for bias and RMSE using the IST method indicate a radius of impact of about 5 h, while

the results using the AT method hardly change with decreasing trajectory length. However, only one month of data is used for Tara which might not be long enough to draw reliable conclusions concerning the comparison of results for Tara and both other stations.

These results are supplemented by explained variances calculated using the TV method (Fig. 2.11). For Alert and Barrow, the explained variances increase monotonically with increasing trajectory length which shows that heat fluxes in remote areas can have a certain impact on the air temperature at a given location. However, the largest impact in this method is also seen in the first 10 h where the slope of the curves is the largest. Therefore, a radius of main impact can be defined by relating it to the region with the largest slope of the curves. By this definition, R_t is reached at the transition from steeper to shallower slopes. This transition is pronounced for all stations at a trajectory length of 10 h which is consistent with the results from the AT method.

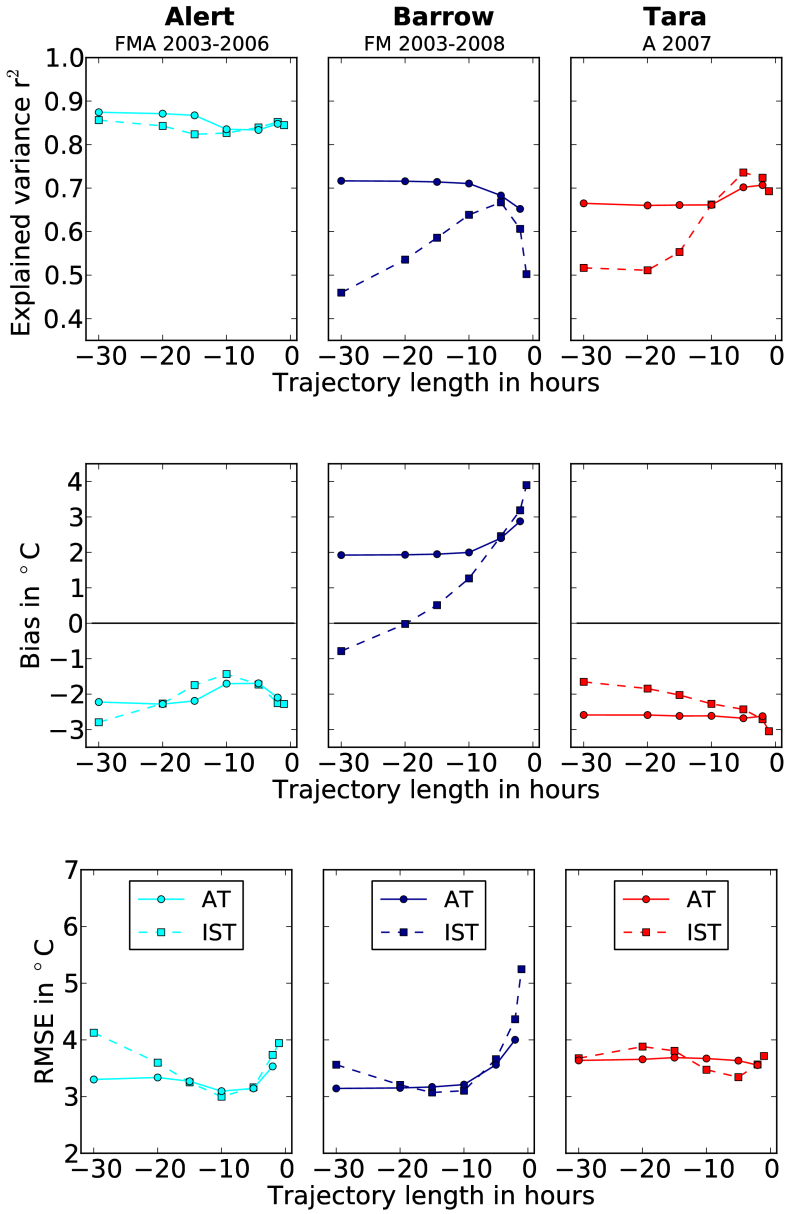

Figure 2.10: Explained variances (upper), bias (middle) and RMSE (lower) for Alert, Barrow and Tara (JAA) as a function of trajectory length using the IST and AT methods, with 350 m ABL depth in the latter.

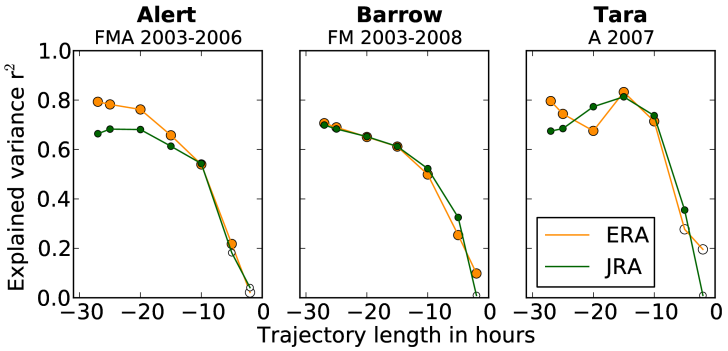

Figure 2.11: Explained variances between temperature difference of the model starting temperature and the observed 2-m air temperature at the station and mean sensible heat flux along the trajectories (TV method) for Alert, Barrow and Tara (AA) as a function of trajectory length using a ABL depth of 350 m. The filled circles are significant at the 95 % level.

Correlation length scales for surface air temperatures have also been calculated by Rigor et al. (2000). They correlated 12-hourly temperature data measured at land and ocean stations in the Arctic during 1979 to 1997. In winter, correlations decreased to about 0.8 (corresponding to an explained variance of 0.64) for separations between the stations of 300 to 400 km (their Fig. 5). Thus, despite the different methods used the results are of the same order of magnitude as the radius of impact found in the present study.

2.5 Discussion

One can see that the different methods having been applied explain the observed variances in general quite well. However, the RMSE values are as large as 3 to 4 °C. Possible reasons for these large differences of modeled and in situ temperatures are discussed in the following.

2.5.1 Uncertainties of input data

Comparing trajectory positions calculated from the surface wind fields of the two reanalyses reveals large differences in the order of 100 km after 15 h. This points to large uncertainties in the surface wind fields. Jakobson et al. (2012) compared wind speed profiles from tether-sonde sounding data at Tara to different reanalyses. Using 29 profiles, they found that the ERA and JRA reanalyses generally agree well but slightly overestimate the 10-m wind speeds by about 1 $m s^{-1}$ with an RMSE of only 1.5 $m s^{-1}$. Uncertainties of 1 $m s^{-1}$ can cause separations of trajectories in the order of 100 km after 30 h and will influence the flux calculations. Increasing the wind speed by 1 $m s^{-1}$ in a sensitivity study (not shown) caused changes of the model temperature by up to 1 °C for individual trajectories. However, the mean impact on the correlation and RMSE for the ensemble of trajectories was found to be small.

There are also uncertainties in the location of the trajectory points arising from the calculation method. In reality air motions are not only horizontal but air parcels also experience rising or sinking. Since wind speed and direction are usually changing with height, neglecting vertical motions leads to errors in the positions. Thus the representation of an air parcel as a box extending over the entire ABL with constant wind represents in most cases only a rough approximation of natural conditions.

Ice concentrations are available only on a daily basis with a grid spacing of 12.5 km (and 6.25 km for AA). This means that small scale features and ice concentration changes on shorter

timescales are not captured. Furthermore, there are also uncertainties in the retrieval method. Andersen et al. (2007) compared ice concentrations from SSM/I data using different algorithms to SAR data in winter. They found that the ASI algorithm tends to underestimate ice concentrations close to 100 % by 2.1 % and ice concentrations have an uncertainty range of 3.9 %. NT2 shows a smaller underestimation of 0.4 % similar to Bootstrap with 0.3 % with a larger uncertainty range of 4.9 % in regions with high ice concentrations. A comparison of the algorithms for AMSR-E data in the Arctic show that overall ASI ice concentrations are 1.4 % smaller than Bootstrap and 2.0 % smaller than NT2 ice concentrations (Spreen et al., 2008). Furthermore, Shokr and Kaleschke (2012) showed that ice concentrations are underestimated in the presence of thin ice below 12 cm thickness depending on the surface conditions. The impact of a constant error in the ice concentration of 5 % was investigated in sensitivity studies (not shown) and found to be small causing model temperature changes of less than 0.5 °C. Since ice concentration data along the trajectories are above 90 % in most cases (Fig. 6) the effect of an underestimated ice concentration by a few percent in the presence of thin ice can be expected to be small.

There are also uncertainties concerning the ice surface temperatures. Hall et al. (2004) compared MODIS ice surface temperatures to in situ measurements and found uncertainties in the order of 1.3 °C. In addition, the considered cases may still contain clouds which notably influences the ice surface temperature (Vihma and Pirazzini, 2005). There are uncertainties concerning the cloud mask and fog is sometimes not classified as clouds (Hall et al., 2006). Furthermore, even if there were no clouds present during the overpass of the satellite, there might still be cloudy conditions at the time of the trajectory path. An attempt to use cloud data from the reanalyses turned out to be impracticable due to the larger grid sizes. Additional uncertainties arise because of the inaccurate trajectory positions. A displacement of 20 km can cause uncertainties in the MOD29 ice surface temperatures of up to 2 °C (not shown). The impact of these large uncertainties is investigated by assuming a constant offset between MOD29 and real ice surface temperatures of 1 °C. The average changes in the modeled temperature were of the order of 1 °C resulting in changes of the bias and RMSE of up to 1 °C (not shown). This means that the largest source of uncertainties in the used methods is due to inaccurate ice surface temperatures which are mainly caused by inaccurate trajectory positions and by radiative effects from undetected clouds.

Despite these uncertainties the analyses show that spatial surface temperature variability in the surrounding of a location has a significant impact on 2-m air temperatures at this location. This shows that a good representation of ice concentration and ice thickness in models would improve not only temperatures but also surface winds since ice concentrations also influence the shape of the wind profile (Tisler et al., 2008) and even the atmospheric pressure patterns.

2.5.2 Impact of model assumptions

Several model assumptions and simplifications mentioned already in Sect. 2.3 should also be kept in mind for the interpretation of results obtained by the AT and the TV method. Additional uncertainties which might be responsible for the large RMSE arise, for example, from the used roughness lengths for momentum z_0 and heat z_T which are set constant in the model using the relation $z_T/z_0 = 10^{-1}$ for simplicity. For this reason, different constant values of z_0 and z_T over sea ice have been tested but the impact was moderate on both RMSE and biases and the explained variance changed only little. However, it cannot be excluded that variable values accounting for the sea ice topography (Andreas et al., 1984; Garbrecht et al., 1999, 2002; Vihma et al., 2003; Guest and Davidson, 1987; Lüpkes and Birnbaum, 2005; Stössel and Claussen, 1993) would have a larger impact. This cannot be tested here because the sea ice topography is dominated by pressure ridges in regions with large sea ice concentration and topography data are not available. Estimating the variability of drag coefficients by parametrisations accounting for

sea ice concentration (Andreas et al., 2010; Lüpkes et al., 2012a) shows that its impact on drag coefficients is only small in our case. This would be different during summer or in the marginal sea ice zones where the surface topography is determined by ice floe edges and edges at melt ponds so that it can be parametrised as a function of sea ice concentration as described in the above mentioned literature.

It should also be stressed that the present method does not allow to model the feedback mechanism of the atmospheric processes on sea ice, since ice concentrations and ice surface temperatures are prescribed from satellite data. This implies that, although only sensible heat fluxes occur as a direct source for temperature change in the model equation, also other processes which have contributed to the observed surface temperature variability are indirectly accounted for. Such processes are, for example, heat transport through ice and radiation. A variation of parameters like surface roughness would also affect the surface temperature and sea ice drift but this kind of interaction is excluded by prescribing the observed surface temperature. This means that the model underestimates the impact of sea ice variability which can only be obtained by a fully coupled ice-atmosphere model.

In addition, the ice concentration does only represent the mean ice conditions in one pixel of 12.5 km (or 6.25 km for AA). It does not contain any information about the spatial distribution of open water areas in the pixel area. Andreas and Cash (1999) have shown that the heat transfer from wintertime leads and polynyas is more efficient for small leads. They found transfer coefficients of $1.0{\cdot}10^{-3}$ for a fetch larger than 100 m and of $1.8{\cdot}10^{-3}$ for smaller fetches. Maslanik and Key (1995) calculated that a fetch increase from 10 to 100 m decreased sensible heat fluxes from an open water lead by 34 %. This means that the spatial distribution, size and orientation of open water areas influence the heat transfer and that our present estimation of open water impact can be seen as a lower limit and the real impact could be much larger (Marcq and Weiss, 2012).

2.6 Conclusions

The main goal of this study was to investigate the dependence of the 2-m air temperature on the surface temperature variability around three Arctic sites and to determine its characteristic radius of impact. These sites were Alert, Barrow and the French schooner Tara during its drift across the Arctic cean. Three approaches were used which are based on backward trajectories calculated from 10-m wind fields of the ERA-Interim and the JRA25 reanalyses. As a first step, the 2-m air temperature measured at the stations was correlated with the average MODIS sea ice surface temperature along the trajectory paths. For the other two methods, a simple Lagrangian box model, which was run along the trajectories, was applied to calculate the surface sensible heat fluxes and the air temperature evolution along the trajectories. Four different ice concentration data sets (SSM/I ASI, AMSR-E ASI, NASA Team 2 and Bootstrap) and MODIS ice surface temperatures were used. For the AT method the modeled temperatures at the stations were compared to the measured ones and for the TV method temperature changes between the model temperature at the trajectory starting point and in situ measurements at the stations were compared to mean sensible heat fluxes. The investigation was carried out for the cold season with only few clouds to restrict the study to conditions where a large impact of surface fluxes can be expected.

It is found that the AT method explains a large amount, namely 70 (Barrow) to 90 % (Alert), of the observed 2-m air temperature variability at all stations. All methods give slightly better results using ERA trajectories than using those derived from the JRA reanalysis. The results depend only weakly on the sea ice concentration products although they show significant differences in the sea ice distributions. For example, the correlation coefficient between measured and

calculated 2-m temperatures at the different sites changes only by 10^{-4} for a 5 % change of sea ice concentration. This small sensitivity can be explained by the independence of measured ice surface temperatures and ice concentrations. However, in an atmospheric model coupled with a thermodynamic sea ice model, such as ERA-Interim, the ice surface temperature adjusts to the ice concentration and ice thickness and thus changes of the ice concentration would have a larger effect (Lüpkes et al., 2008b).

In most considered cases, the IST method explains a smaller percentage of the 2-m air temperature than the AT method (though values ranging still between 46 % and 89 % for Barrow and Alert, respectively. This points to the fact that the spatial variability of the far field contributes noticeably to a local temperature that is otherwise dominated by the near field surface conditions.

The results show the highest sensitivity to uncertainties in the ice surface temperatures. These are mainly due to uncertainties in the trajectory positions and radiative effects from undetected clouds. The characteristic radius of impact of sea ice concentration and surface temperature variability was investigated by varying the trajectory lengths and was found to be of the order of 200 km assuming an average wind speed of $5\,\mathrm{m\,s^{-1}}$. This radius is robust for Barrow and Alert using all three methods.

In general, all results for Tara are less relevant compared with those for Alert and Barrow since only one month of data is used for the calculations. But at least the TV method also indicates a radius of impact in the order of 200 km which does not contradict the findings for the other two stations.

The present results should be viewed in the light of restrictive model assumptions and uncertainties of input data. Nevertheless, they reveal a large dependence of atmospheric boundary layer temperatures on heterogeneous surface temperatures in the Arctic which underlines the large importance of a very accurate representation of all processes influencing the surface temperature in climate and weather prediction models.

3 Influence of leads on the atmospheric boundary layer

In the previous chapter we demonstrated the large dependence of near-surface atmospheric temperatures over the Arctic Ocean on surface temperature heterogeneities. Under cloud-free conditions, most surface temperature heterogeneities in the Central Arctic are due to leads, whose surface consists of open water or thin ice. Thus, they have a much higher surface temperature than the surrounding thick ice. Previous investigations showed already that the convective plumes emanating from leads do not only influence atmospheric temperatures and sensible heat fluxes, but also have a large impact on atmospheric humidity, the wind vector, and ABL stratification and height. However, in situ measurements over leads are rare.

In this chapter we analyze the impact of leads on the atmospheric boundary layer based on aircraft measurements that were conducted during the campaign STABLE. We present case studies of measurements in the environment of four wide leads and analyze the downstream evolution of temperature, wind, and humidity, as well as the growth of the convective plume. Furthermore, the data are used to derive vertical profiles of turbulent fluxes of heat and momentum over and downstream of the leads. In addition, we use long transect flights to analyze the impact of leads on the near-surface atmospheric temperature on regional scales. These results will help improve our understanding of the interaction between leads and the atmospheric boundary layer, which is crucial for a better representation of the lead impact in climate models.

A large part of the results presented in this chapter is an extended version of the content published in Tetzlaff et al. (2015), while Sect. 3.4 and the resulting discussion are an additional contribution for this thesis.

3.1 Introduction

Sea ice cover prevents direct contact between the ocean and atmosphere and thus has a large impact on the exchange of energy, moisture, and momentum. A direct interaction is only possible over so-called polynyas and leads. The latter consist of elongated channels that form due to divergent sea ice drift and are either ice free or covered by thin ice. Their size can be quite variable with widths from a few metres to kilometres and lengths up to tens of kilometres (e.g. Lindsay and Rothrock, 1995; Marcq and Weiss, 2012).

Due to large temperature differences between the air and the lead surface, particularly in winter, convective plumes form over leads that can have a large impact on atmospheric processes in sea ice covered regions. This has been shown in the past on the basis of data from several campaigns and by modeling studies using different types of models ranging from Large Eddy Simulation (LES) models (e.g. Weinbrecht and Raasch, 2001; Esau, 2007) to mesoscale models (e.g. Dare and Atkinson, 2000). A comprehensive summary of previous studies on lead-atmosphere interactions can be found in Vihma et al. (2014) and Lüpkes et al. (2008a, 2012b), but some findings will be summarized in the following to demonstrate the relevance of the present study.

Processes over leads have been investigated, for example, because of their expected impact on the surface energy budget which is relevant for the polar ocean climate. Important campaigns addressing the near-surface atmospheric processes were LEADEX (Ruffieux et al., 1995; Persson et al., 1997), AIDJEX (Andreas et al., 1979), and SHEBA (Overland et al., 2000; Persson et al., 2002; Pinto et al., 2003). It was found that upward turbulent sensible heat fluxes over leads can exceed several hundred Wm^{-2} in winter, while fluxes over the surrounding thick sea ice are usually much smaller. Nevertheless, Overland et al. (2000) found that, averaged over the area of the SHEBA camp site, the upward heat fluxes from the leads were balanced by the negative fluxes over the thick ice. Lüpkes et al. (2008b) showed in a 1D modeling study that despite this equilibrium of upward fluxes over leads and downward fluxes over the sea ice, leads have a large influence on the atmospheric conditions. Namely, they found also that, under clear skies in winter, the increase of the lead concentration by 1 % caused an air temperature increase of up to 3.5 K after two days model runtime.

Another important result on the impact of leads was based on data from the campaign AIDJEX and other ones. Andreas and Murphy (1986) and Andreas and Cash (1999) found that the heat transfer is more effective over narrow leads than over wider ones, given the same atmospheric stability. A possible explanation is an interplay of forced and free convection over smaller leads. Marcq and Weiss (2012) applied this fetch dependent heat transfer parametrisation by Andreas and Cash (1999) to a lead width distribution derived from a satellite image. Since the open water fraction in the satellite image was dominated by narrow leads, the heat flux estimates using the parametrisation by Andreas and Cash (1999) were larger when they used the full lead width distribution instead of only an average lead width. Their analysis also demonstrates the shortcoming of the heat flux parametrisations currently used in climate models, which simply average the fluxes over open water and ice within a grid cell. This method can lead to an underestimation of the heat fluxes of up to 55 % compared to the situation when the full lead width distribution is considered.

A shortcoming of the above mentioned campaigns was that measurements were only conducted over the sea ice surrounding the leads. Flux measurements directly over a lead were carried out, however, during the Winter Arctic Polynya Study (WARPS, Lüpkes et al., 2012b) using a mast installed at RV Polarstern as well as the helicopter-borne turbulence probe HELIPOD (Bange et al., 2002). Besides a large sensitivity of the turbulent heat fluxes to the ice cover on the lead, this study showed that turbulent heat fluxes of the atmospheric boundary layer (ABL) were highest over wide leads. These results are only seemingly in contrast to the above-mentioned findings for near-surface fluxes over wide leads since the leads considered by Andreas and Cash (1999) were much smaller with a fetch below 100 m. This documents the complexity of the related processes and suggests that more measurements are necessary to obtain an improved understanding of ABL processes over the complete spectrum of different lead geometries.

Other modeling studies than those already mentioned concentrated for example on the formation of the plume, which is the region influenced by the individual convective elements (thermals) emanating from leads, and on the development of the convective internal boundary layer over leads. We define the ABL height as the height of the lower boundary of the capping inversion. The upper boundary of the growing plume is the height of the internal convective boundary layer (see also Fig. 1.3 in Sect. 1.2.). It starts with zero at the upstream edge of the lead and can reach the ABL height over the lead or in some distance downstream of it. In case of penetrating convection the plume influences the ABL height so that its upstream and downstream values can differ.

It was found that the plume characteristics depend on lead width, lead ice cover, wind speed, upstream stratification of the ABL, and the inversion strength (Glendening, 1995; Pinto et al., 1995; Zulauf and Krueger, 2003b,a; Alam and Curry, 1995). As shown by Lüpkes et al. (2008a)

such characteristics are important for the development of parametrisations for models whose grid sizes are small enough to resolve leads, but too large to resolve the detailed structure of convective plumes. They found that there is a core region in plumes with vertical heat transport along the vertical gradient of potential temperature, but with counter-gradient transport in the outer regions. Finally, with their non-local parametrisation accounting for the latter effect they could reproduce results of an LES model that was used earlier also by Weinbrecht and Raasch (2001). These studies were valid for wind speeds exceeding $2.5\,\mathrm{m\,s^{-1}}$. Esau (2007) showed that the flow structure over leads can be much more complex when the geostrophic wind speed is close to zero. Finally, all these studies reveal that the investigation of the lead impact is still in an early stage and more research is necessary to gain a better insight into the processes over leads and their impact on the polar ABL. Our present knowledge of the upper layer processes over leads is mainly based on modeling studies, since observations are rare.

Hence, the aircraft campaign STABLE (Spring Time Atmospheric Boundary Layer Experiment) was carried out over the Northern Fram Strait in spring 2013 to extend the available data base related to the lead impact on the ABL. The presentation and analysis of results from STABLE forms the main goal of the present work. The following questions are addressed: How strong is the impact of individual leads on the mean and turbulent quantities in a region of a few tens of kilometers downstream of the leads? How strongly does the heat input from leads influence the vertical and horizontal structure of the atmospheric boundary layer over leads? Which flight patterns (lead parallel or lead orthogonal flight sections) are most suitable to derive turbulent fluxes over leads? How do lead ensembles affect the near-surface atmospheric temperature on larger scales of a few hundred kilometers?

Here, we lay the focus on the small-scale analysis of measurements over four leads and on the related variability of the ABL impact dependent on the meteorological forcing and sea ice cover on the leads. In addition, we evaluate the lead impact on regional scales using transect flights of up to 300 km length to analyze the atmospheric temperature change related to a changing lead coverage. The STABLE dataset forms a valuable basis for future modeling studies since necessary input data, such as inflow profiles, surface temperatures, and geostrophic wind, are provided.

The study is organized as follows: Case studies of the ABL development over and downstream of four different wide leads are presented in Sect. 3.2. This includes the analysis of mean and turbulent quantities. The flux calculation procedure, as well as investigations of the optimal flight length and orientation of flight sections relative to the leads for flux measurements are presented in Sect. 3.3. The regional impact of a variable lead cover on the atmospheric temperature is analyzed in Sect. 3.4, followed by a discussion and conclusions in Sect. 3.5.

3.2 Case studies of the boundary layer development and turbulent fluxes over wide leads

To analyze the lead impact on the atmospheric boundary layer meteorological measurements were conducted in 2013 during the campaign STABLE over the sea ice covered region of the Fram Strait using the Polar 5 research aircraft of the German Alfred Wegener Institute. Since the largest impact of leads can be expected when temperature differences between the lead surface and the advected air are large, the campaign was carried out in March, when the near-surface air temperatures usually reach very low values between -20 and -35 °C during off-ice air flow from the north. In this section, results of the flight patterns over four individual wide leads are presented and analyzed. The flights took place on 10, 11, 25, and 26 March 2013. The flight patterns consisted of several short flight sections in the very close environment of the leads and aimed at the detailed measurement of the ABL structure. An overview of the flight sections is

given in Fig. 3.1.

It is important to understand that the selection of leads aboard the approaching aircraft at roughly 2000 m height was difficult due to the often curved shape and variable width along the leads. Another challenge was to estimate thin-ice conditions on the lead in advance, which was necessary since once the decision was made for a specific lead it could not be changed without significant loss of flight time. We tried to select straight lead sections with almost constant width, but this was not possible without compromise. Finally, four cases were found which differed strongly from each other with widths of 1.6, 2.1, 2.3, and 8.3 km, respectively, and lengths of lead sections from 5.0 to 20.5 km. Furthermore, all leads differed by their sea ice cover. A list of the lead characteristics can be found in Table 3.1. All four leads were chosen because the prevailing winds were nearly perpendicular to the leads and no clouds were present.

The flight patterns consisted of low-level flights roughly perpendicular to the lead and along the wind to study the near-surface impacts, supplemented by saw-tooth patterns on 11 and 25 March along the same direction that give insight into the vertical ABL structure downstream of the lead. In addition, lead parallel flight legs were conducted at different heights at various distances to the upstream lead edge. Thus, some sections were located in the convection regime over the lead and some in the region over ice. In the following, all indicated distances x will be relative to the upstream edge of the corresponding lead.

In the next sections, we describe the evolution of temperature, humidity, wind speed and direction, as well as the growth of the internal boundary layer downstream of the leads based on these flight patterns. Furthermore, we present profiles of turbulent fluxes of heat and momentum derived from the parallel flight legs. A detailed description of the flux calculation procedure and the data quality control can be found in Sect. 3.3.

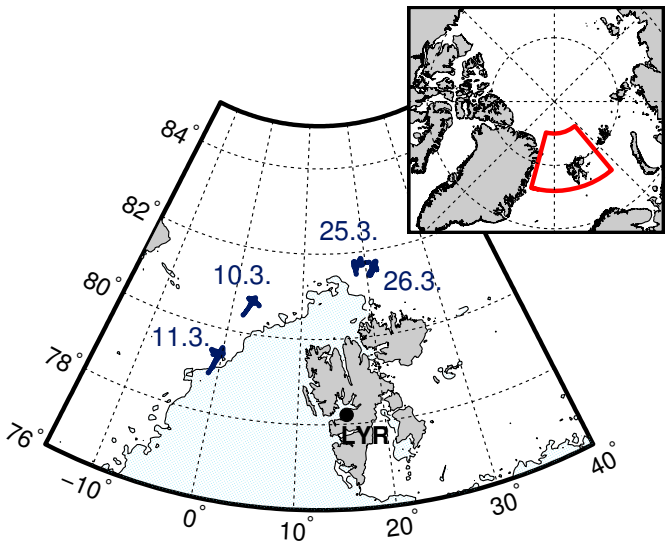

Figure 3.1: Lead patterns during STABLE over the Fram Strait. The contour shows the 70 % AMSR-2 ASI ice concentration on 25 March 2013 (data from http://www.iup.uni-bremen.de:8084/amsr2/). All flights were operated from Longyearbyen (LYR). The leads were located below the flight sections and oriented approximately in east-west direction.

Table 3.1: Lead characteristics

Date	Lead width (km)	Lead length (km)	T_s [a] (°C)	Wind speed ($m\,s^{-1}$)	Inflow angle[b] (°)
10 March 2013	2.3	6.5	-10.7 ± 3.9	5.5	85
11 March 2013	8.3	20.5	-6.6 ± 3.2	10.5	90
25 March 2013	2.1	15	-17 ± 0.4	8.0	110
26 March 2013	1.6	5	-5.8 ± 3.8	7.5	105

[a] mean surface temperature and standard deviation
[b] angle between wind vector and lead orientation; 90° represent a flow perpendicular to the lead

3.2.1 10 March 2013

In the first case study, we consider a lead of about 2.3 km width and 6.5 km length (Fig. 3.2a). It was covered by thin ice and fractional open water areas resulting in an average surface temperature (T_s) of about -10.7 °C (Fig. 3.2b). The flight pattern consisted of a low-level flight leg of about 15 km length at 45 m height orthogonal to the lead and along the direction of the surface wind. One stack of lead parallel sections was flown over the center of the lead at $x = 1.3$ km distance from the upstream lead edge and the second one at the downstream edge at $x = 2.3$ km. The small offset of only 1 km between the two staggered sections was chosen because sea smoke developing over the lead indicated only a small downstream drift of the plume. In addition, we conducted fast ascending or descending flight legs to derive profiles at the upstream and downstream sides of the lead, at $x = -7$ km and $x = 10$ km, respectively.

Measured meteorological variables along the cross-leg and the sensible heat fluxes derived from the parallel legs at 35 m height are shown in Fig. 3.3. Near-surface sensible heat fluxes were about 58 Wm^{-2} at the center of the lead and decreased to about 17 Wm^{-2} at the downstream

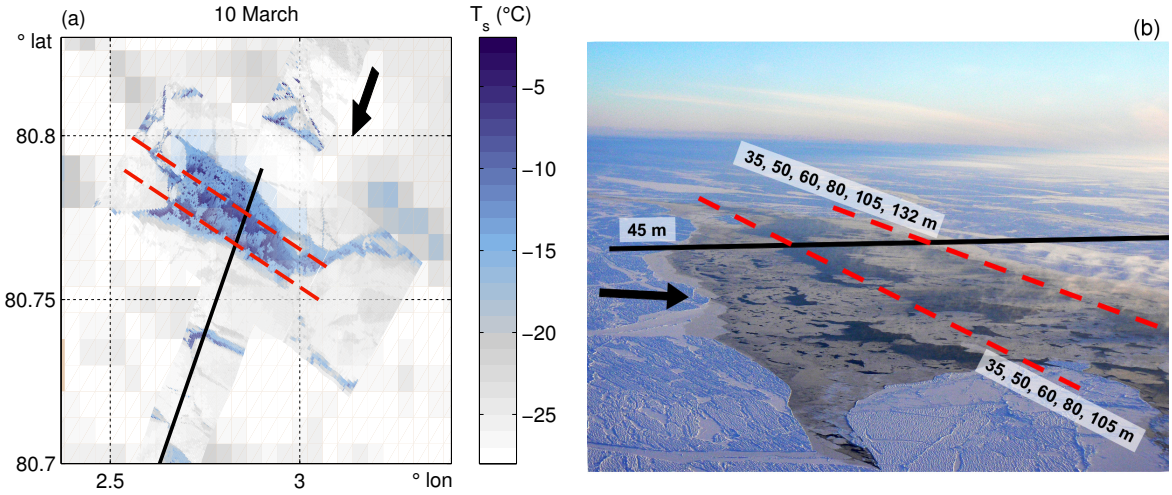

Figure 3.2: (a) Overlay of surface temperatures from MODIS (available through http://reverb.echo.nasa.gov) and the aircraft-based IR-scanner with flight legs orthogonal (solid line) and parallel to (dashed lines) the lead for the case studies on 10 March. The arrow denotes the wind direction. **(b)** Corresponding photograph of the same lead and flight legs. The numbers indicate the heights of the different legs.

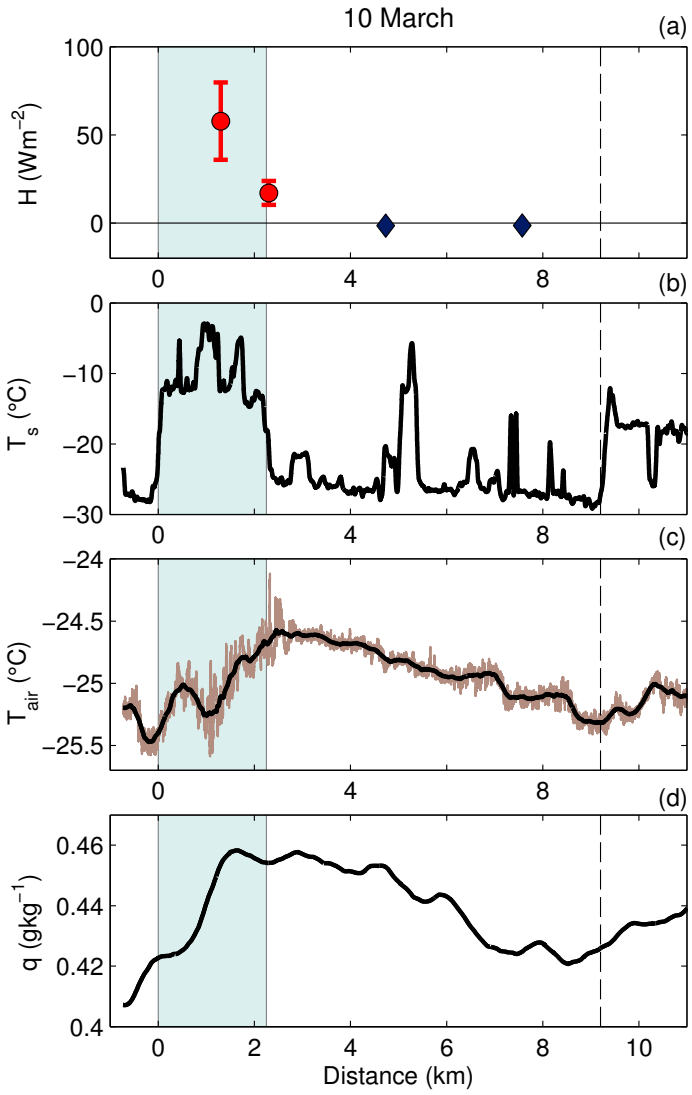

Figure 3.3: **(a)** Sensible heat flux derived from parallel (circles) and cross (diamonds) legs, **(b)** surface temperature, **(c)** air temperature, and **(d)** specific humidity on the cross leg on 10 March 2013 as a function of the distance to the upstream end of the lead. The flight height is approximately 45 m. The shaded area denotes the lead extent and the dashed line the starting point of a secondary lead. For temperature, a running mean over a distance of about 350 m (dark line) is shown in addition to the high-frequency data (light line).

edge. Here and in the following, positive values refer to upward sensible heat fluxes and negative ones to downward fluxes. The positive fluxes caused a total increase of the air temperatures (T_{air}) by about 0.8 °C over the lead. Downstream of the lead, between $x = 3$ km and $x = 9$ km, T_{air} decreased by 0.7 °C until a secondary lead was reached. This temperature decrease was related to small negative heat fluxes of about -1.5 Wm^{-2} in the newly developing internal boundary layer (IBL) over the ice. Here, data from the cross leg could be used to derive turbulent fluxes since ice conditions downstream of the lead were homogeneous enough. A similar behaviour as for temperature was found for the specific humidity with an increase of about 0.05 gkg^{-1} over the lead and a subsequent decrease at the downstream side.

We can get a first impression of the lead effect on the whole ABL column by considering the vertical profiles of potential temperature shown in Fig. 3.4a. The symbols represent averages

over each horizontal flight leg and the error bars indicate the standard deviation. Unfortunately, the potential temperature profile at x = -7 km upstream of the lead was located downstream of another lead and therefore the ABL stratification and temperature do not represent the inflow conditions very close to the upstream end of the lead. Nevertheless, we can use the profile to at least estimate the approximate ABL height upstream of the lead to about 95 m. The temperature profile derived from the horizontal stack at the lead center shows a slightly unstable and thus convective IBL of already 60 m thickness that was capped by an inversion.

Simultaneously, the sensible heat flux linearly decreased at this position from about 58 Wm^{-2} at 35 m height to 26 Wm^{-2} at 55 m, and nearly 0 Wm^{-2} at 65 m (Fig. 3.4b). The top of the convective layer is between 65 and 75 m at x = 1.3 km indicated by the lower shaded area in Fig. 3.4. At x = 2.3 km, the convective IBL had grown further to a height exceeding 100 m (upper shaded area in the figure) and the potential temperature at 60 m height had increased by about 0.5 K.

The IBL growth between x = 1.3 km and x = 2.3 km is also visible in the sensible heat flux profile at 2.3 km, where positive fluxes now occurred up to a height of 90 m and small entrainment fluxes of about -6 Wm^{-2} were present at 110 m height. During the horizontal flight legs above 60 m at the lead center and at 138 m at the lead edge, we observed intermittent turbulence indicating that in these levels the plume was penetrating the capping inversion (see below). The impact of the plume in the layer between 100 m and 140 m height is also evident from the large temperature difference of up to 4 K between the profiles at x = 2.3 km and x = 10 km. The profiles at 1.3 and 2.3 km show also a much less stably stratified layer than the upstream profile below 150 m height.

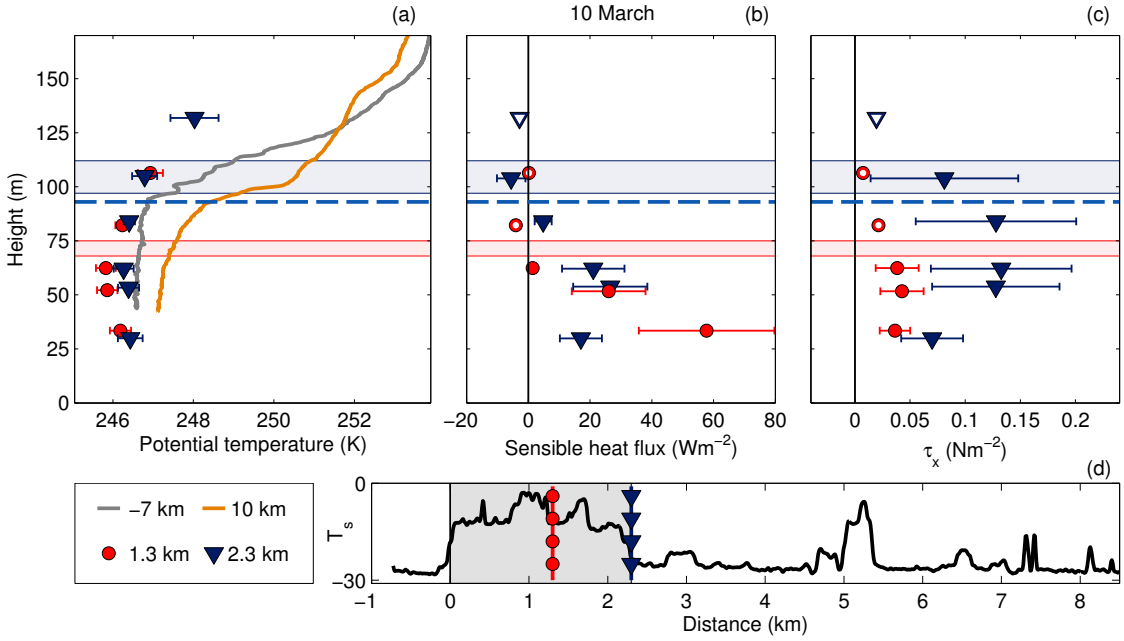

Figure 3.4: Profiles of **(a)** potential temperature, **(b)** sensible heat fluxes, and **(c)** momentum fluxes on 10 March. The different symbols represent the distance of the flight leg from the upstream edge of the lead. **(d)** The positions of the flight legs are indicated in the cross-section of the surface temperature. Open symbols mark legs with intermittent turbulence (see text). The horizontal dashed line and the horizontal shaded areas mark the upstream ABL height and the IBL heights derived from the potential temperature profiles.

The localized burst through the inversion layer is visible in the measurements of potential temperature and vertical wind along the horizontal legs above the inversion. Figure 3.5a,b shows an example of the flight leg in 138 m height at the downstream edge of the lead. The non-periodic fluctuations associated with intermittent turbulence are clearly different from the fully developed turbulence observed in the plume at 38 m height (Fig. 3.5c,d). The classical method for deriving turbulent fluxes is not applicable for intermittent turbulence. Nevertheless, we included the calculated flux values and marked them specifically in the figures to indicate heights at which intermittent turbulence is present.

The plume effect on the inversion is not any more visible in the temperature profile at 10 km downstream, where the inversion strength was comparable to the upstream conditions. The ABL over the ice was stably stratified starting already from the lowest measurement height of about 40 m and the height of the inversion base decreased again to 80 to 90 m, which was probably due to the cooling of the ABL over the ice downstream of the lead. Compared to the profile at the center of the lead, potential temperatures at 50 m height increased by about 1.5 °C, which demonstrates that the overall impact of the lead is still strong at a position 10 km downstream of it.

The profiles of sensible heat fluxes also provide useful information about the plume structure. At the downstream edge of the lead the maximum fluxes of 26 Wm^{-2} occurred at 55 m height, rather than near the surface, where smaller fluxes of only 17 Wm^{-2} were found. This decrease of the flux near the surface can be explained by the plume inclination over and downstream of the lead and by the development of a new stable IBL below the plume over the sea ice. At $x = 2.3$ km, the higher measurement levels were more in the center of the plume than the lowest level, while the flux at higher levels was still influenced by the convective plume emanating from the lead.

The momentum fluxes were very small over the lead center, with values below 0.05 Nm^{-2} (Fig. 3.4c). They increased over the downstream edge of the lead with maximum values of about 0.15 Nm^{-2} at the plume center between 60 and 90 m height. As for sensible heat flux the momentum flux downstream of the lead was smaller at 35 m height than at 55 m. A plausible explanation is that the higher level is influenced by the inclined convective plume with strong turbulence while the 35 m level is below the plume's lower boundary.

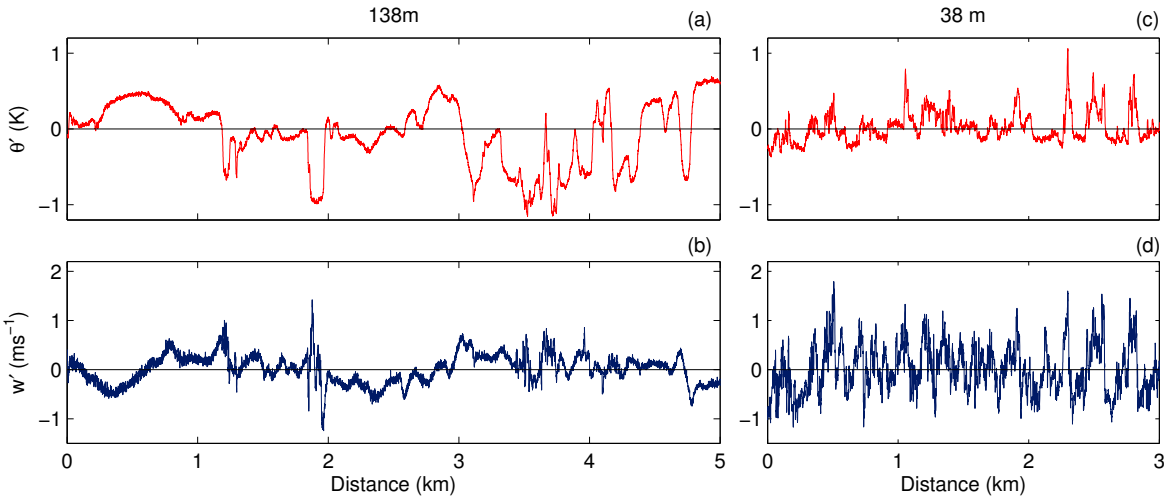

Figure 3.5: Turbulent fluctuations of potential temperature θ' **(a,c)** and vertical wind w' **(b,d)** on 10 March at heights of 138 **(a,b)** and 38 m **(c,d)**.

3.2.2 11 March 2013

For the second lead pattern on 11 March we consider a much wider lead of 8.3 km width and 20.5 km length with a complex ice cover and stronger winds of about 11 m s^{-1} (Fig. 3.6). The ice thickness increased in downstream direction, starting with an area covered by open water and frazil ice in the first 1.7 km (Fig. 3.7b). According to the visual observations during the flight it was followed by a region covered with grey nilas until the downstream end of the lead at $x = 8.3$ km. Further downstream of this region, white nilas was observed until thick pack ice was reached at $x = 28.1$ km. The observed surface temperatures were -2 °C over the frazil ice and gradually decreased to -15 °C over the grey nilas, followed by nearly constant surface temperatures of -15 °C over the white nilas and -21 °C over the thick pack ice.

The flight pattern consisted of a low level flight leg at about 50 m height orthogonal to the lead and parallel to the wind direction and of a vertical saw tooth pattern approximately along the same track (Fig. 3.6). Two stacks of lead parallel horizontal flight legs were located over the lead, in the grey nilas region at $x = 4.4$ km, and at $x = 10$ km over the white nilas region. Near-surface sensible heat fluxes derived from these cross legs were about 160 Wm^{-2} over grey nilas and decreased to about 58 Wm^{-2} over white nilas (Fig. 3.7a). As on 10 March, the cross leg could be used to derive near-surface turbulent fluxes further downstream. Sensible heat fluxes over the white nilas were still positive but with small values of 8 to 12 Wm^{-2}.

Along the cross-section at a flight altitude of approximately 50 m the air temperature increased continuously over the lead, from -23.2 °C upstream to about -21.6 °C at the downstream edge (Fig. 3.7c). Here, we use a linear approximation only to compare the temperature increase rates of different flight sections. The increase rate over the grey nilas region amounted to about 0.2 °C km^{-1}. The air temperature increase continued over the white nilas region, but with a

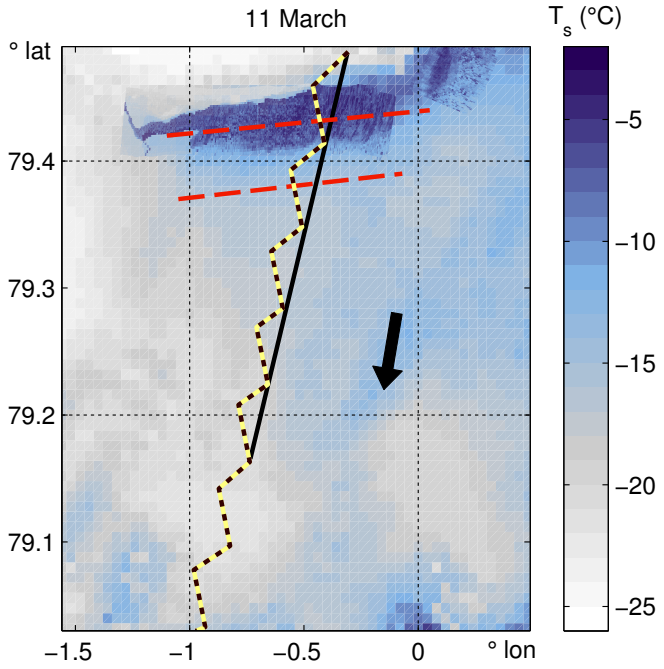

Figure 3.6: Overlay of surface temperatures from MODIS (available through http://reverb.echo.nasa.gov) and the aircraft-based IR-scanner with flight legs orthogonal (solid line) and parallel to (dashed lines) the lead for the case studies on 11 March. The zig-zag curve indicates the saw tooth pattern and the arrow denotes the wind direction.

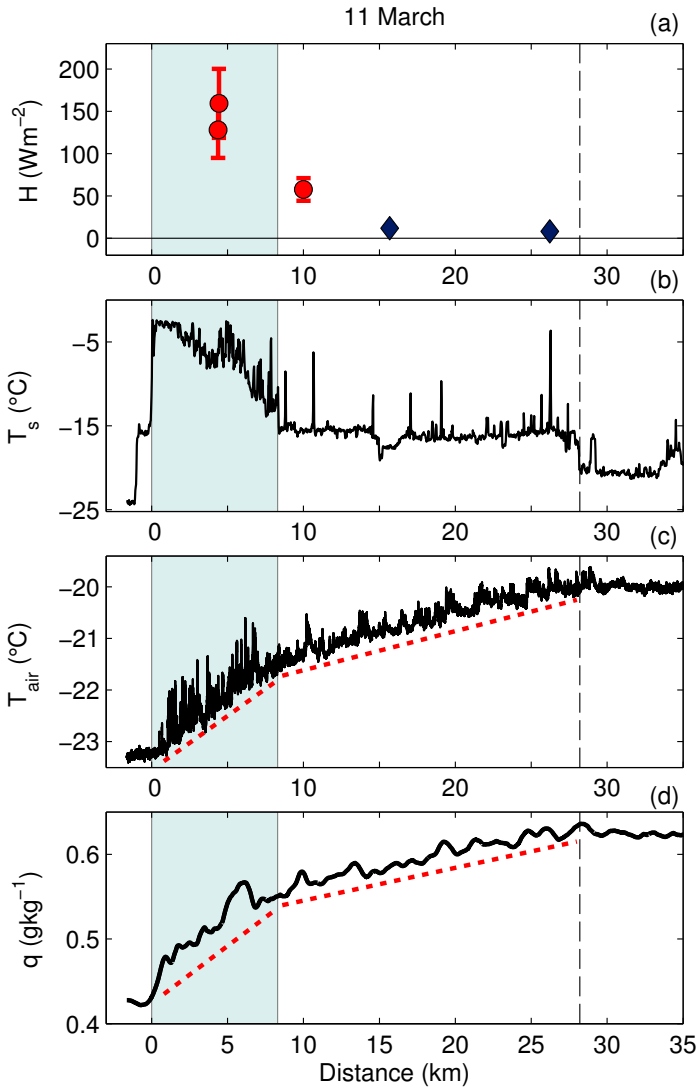

Figure 3.7: **(a)** Sensible heat flux derived from parallel (circles) and cross (diamonds) legs, **(b)** surface temperature, **(c)** air temperature, and **(d)** specific humidity on the cross leg on 11 March 2013 as a function of the distance to the upstream end of the lead. The flight height is approximately 50 m. The shaded area denotes the lead extent and the dashed line the starting point of the thick ice cover. Dotted lines in **(c)** and **(d)** indicate the rates of temperature and humidity increase.

slower rate of about 0.05 °C km^{-1}, to T_{air} =-20 °C at 28.1 km and stayed constant further downstream over the thick ice region. The specific humidity showed a similar increase (Fig. 3.7d) from 0.43 g kg^{-1} upstream to a constant value of about 0.63 g kg^{-1} over the thick ice. The saw tooth pattern orthogonal to the lead can be used to derive vertical cross-sections of potential temperature and wind speed (Fig. 3.8a,c). According to these cross-sections, the ABL was stably stratified upstream of the lead with a vertical gradient of potential temperature of about 0.018 Km^{-1} and an inversion height of about 190 m (Fig. 3.8b). Over the lead, a convective IBL developed whose thickness increased with increasing distance from the upstream lead edge reaching the inversion at $x = 10$ km. Its base was at this position in the same height as at the upstream side of the lead. Further downstream, the IBL continued growing to a maximum height of about 230 m at $x = 20$ km and thus penetrated the lower levels of the capping inversion (brown

profile in Figure 3.8a,b). The ABL was well-mixed between 10 and 35 km downstream of the inflow edge of the lead and returned to a stable stratification further downstream. Along the way, the whole ABL column warmed by about 3 °C. Thus, the stratification of the upstream profile was restored far downstream of the lead but on a warmer level.

The wind speed upstream of the lead showed a low level jet (LLJ) with a broad maximum of about 12.5 ms^{-1} at heights between 120 and 230 m (Fig. 3.8d). This LLJ was weakened further downstream, in the well-mixed region between $x = 10$ km and $x = 35$ km, with a wind speed of about 10.5 ms^{-1}. It reached its original strength when the ABL stratification stabilized downstream of $x = 35$ km.

Profiles of turbulent fluxes derived from the lead parallel flight legs are shown in Fig. 3.9. The sensible heat flux over the grey nilas, at $x = 4.4$ km, decreased from 160 Wm^{-2} at 45 m to about 56 Wm^{-2} at 85 m height. The saw tooth profiles of potential temperature suggest that the convective IBL had grown to a height of about 140 m at this position. As in the case of 10 March, the horizontal flight sections at 170 m height documented again intermittent turbulence, indicating the penetration of the plume into the inversion layer. It is notable, that at this position we measured counter-gradient fluxes. This means that there were positive sensible heat fluxes

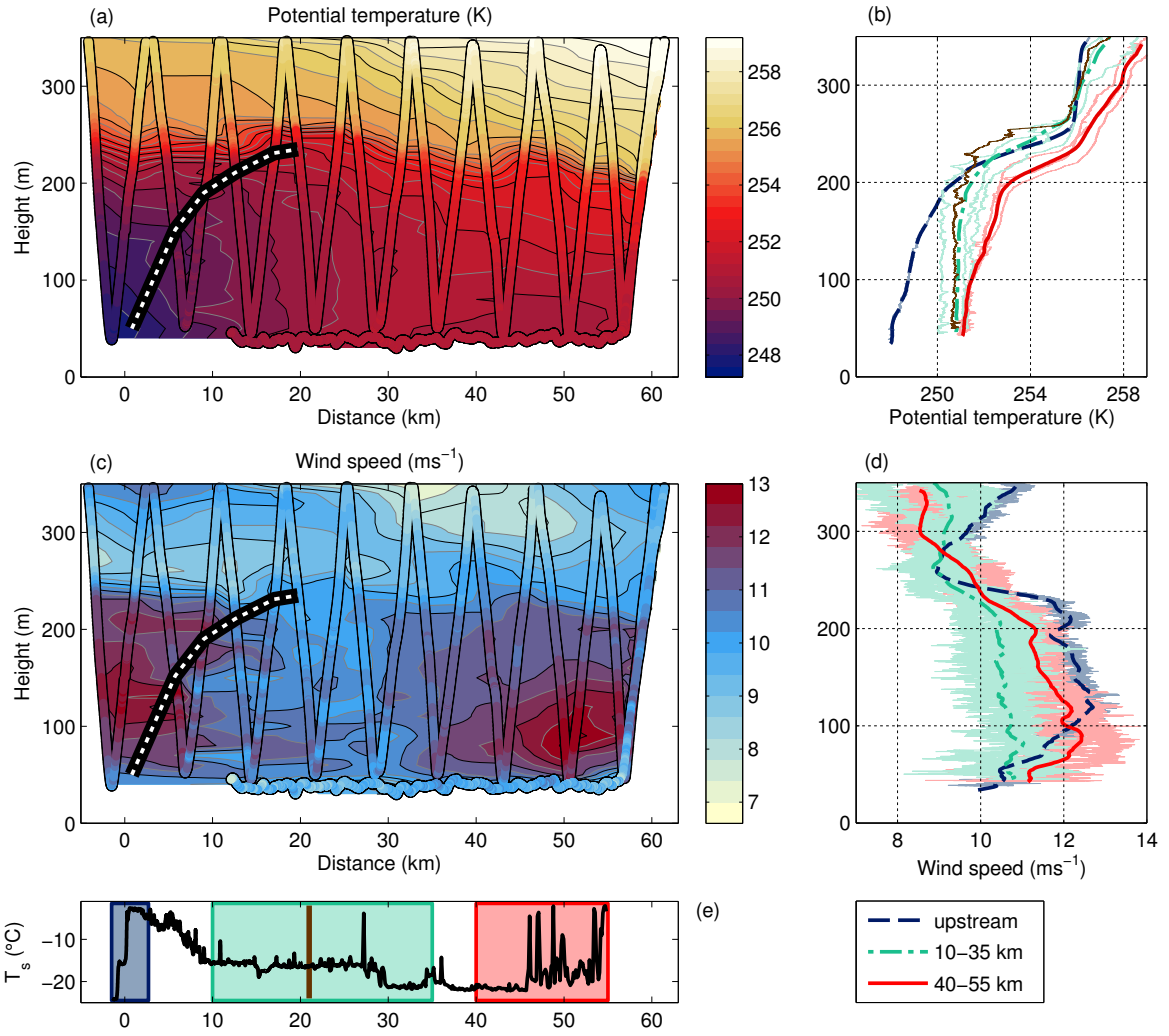

Figure 3.8: Horizontal cross-sections of **(a)** potential temperature and **(c)** wind speed derived from the saw tooth leg on 11 March 2013. The dashed line represents the height of the IBL. Profiles of **(b)** potential temperature and **(d)** wind speed averaged over the regions marked in **(e)**.

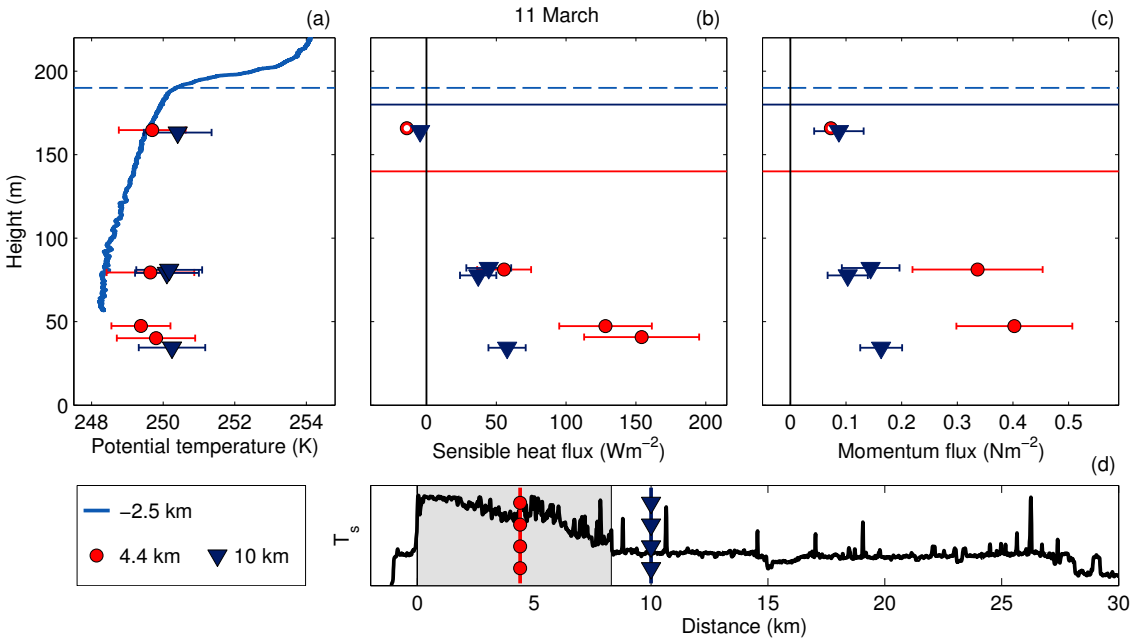

Figure 3.9: Profiles of **(a)** potential temperature, **(b)** sensible heat fluxes, and **(c)** momentum fluxes on 11 March. The different symbols and lines represent the distance of the flight leg from the upstream edge of the lead. The positions of the flight legs are indicated in the cross-section of the surface temperature **(d)**. Open symbols mark legs with intermittent turbulence (see text). The horizontal dashed line and the horizontal solid lines mark the upstream ABL height and the IBL heights derived from the potential temperature profiles of the saw tooth leg.

at 85 m height, even though the potential temperature gradient derived from the corresponding saw tooth profile between 60 and 100 m was also positive. Over the white nilas, at 10 km, the convective IBL had grown approximately to the inversion height of the upstream flow and sensible heat fluxes linearly decreased from about 58 Wm^{-2} at 40 m height to -5 Wm^{-2} at 170 m.

The profiles of momentum flux showed a similar behaviour (Fig. 3.9c). Near-surface momentum fluxes were larger over the grey nilas, with about 0.40 Nm^{-2} at 50 m, and decreased to about 0.16 Nm^{-2} at 40 m over the white nilas.

3.2.3 25 March 2013

A lead of 2.1 km width and about 15 km length could be studied on 25 March (Fig. 3.10). It was mostly covered by white nilas with small embedded areas of grey nilas and open water. The ice surface temperature was about -17 °C, resulting in a temperature difference to the surrounding thick ice of only 8 °C (Fig. 3.11b).

As for the lead on 11 March, a low level flight leg at 35 m was conducted perpendicular to the lead and nearly parallel to the wind direction, supplemented by a saw tooth leg at the same track (Fig. 3.10) approximately. Stacks of lead parallel flight legs at different heights were conducted over the center of the lead, at a distance of 1.3 km to the upstream edge, slightly downstream of it, at $x = 2.7$ km, and further downstream, at $x = 4.3$ km.

The relatively small difference between surface and air temperatures together with a moderate near-surface wind of about 7.5 ms^{-1} caused also small sensible heat fluxes (Fig. 3.11a) derived from the parallel legs. They amounted to only 13 to 16 Wm^{-2} over the lead center and slightly downstream of it and were thus much smaller than in all other cases. Further downstream, at

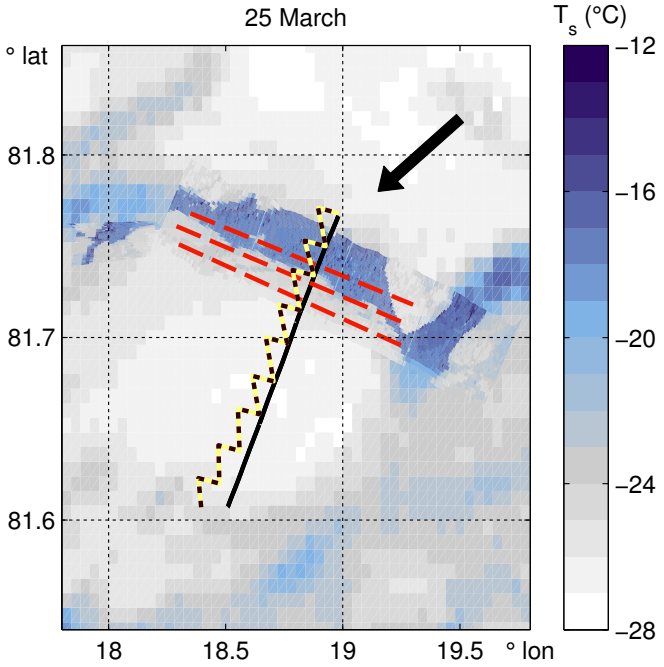

Figure 3.10: Overlay of surface temperatures from MODIS (available through http://reverb.echo.nasa.gov) and the aircraft-based IR-scanner with flight legs orthogonal (solid lines) and parallel to (dashed lines) the lead for the case studies on 25 March. The zig-zag curve indicates the saw tooth pattern and the arrow denotes the wind direction.

$x = 4.3$ km, they were even negative with a value of -5.5 Wm^{-2}. Fluxes derived from the cross leg indicate that heat fluxes remained negative over the ice up to a distance of 15 km.

It is remarkable that despite the small sensible heat fluxes over the lead, the air temperature increased by about 1.2 °C to -24.3 °C along the flight leg orthogonal to the lead at 35 to 40 m height (Fig. 3.11c). The air temperature reached a maximum value at $x = 8$ km and decreased further downstream to -25.4 °C at a distance of 16 km. The specific humidity (Fig. 3.11d) showed a similar behaviour along the cross leg with an increase over the first lead from 0.36 to 0.43 g kg^{-1}. However, the humidity did not return to the upstream value but showed a plateau of 0.39 g kg^{-1} between 10 and 14 km.

In the vertical cross-sections derived from the saw tooth pattern (Fig. 3.12), we found a similar situation as on 11 March. The figure shows that the ABL upstream of the lead was stably stratified already at the lowest flight level at 40 m. The observed potential temperature increased with height already near the surface by 0.014 Km^{-1} until the much stronger capping inversion was reached at 90 m height.

Over the lead, a convective IBL developed that penetrated about 20 m into the capping inversion reaching a maximum height of 110 m at a distance of about $x = 5$ km (Fig. 3.12a, see also Fig. 3.13a). Between $x = 5$ km and $x = 10.5$ km the stable stratification weakened and strengthened again downstream of 14 km (Fig. 3.12b).

It is again remarkable that on 25 March the wind pattern (Fig. 3.12c) was very similar to that on 11 March. Upstream of the lead and downstream of 14 km a distinct wind maximum was found near the inversion height (Fig. 3.12d). This LLJ was absent between $x = 4.5$ km and $x = 10.5$ km where the ABL stratification was near-neutral and probably influenced by the plume. The associated cross leg showed also an interesting pattern of the wind direction, smoothly

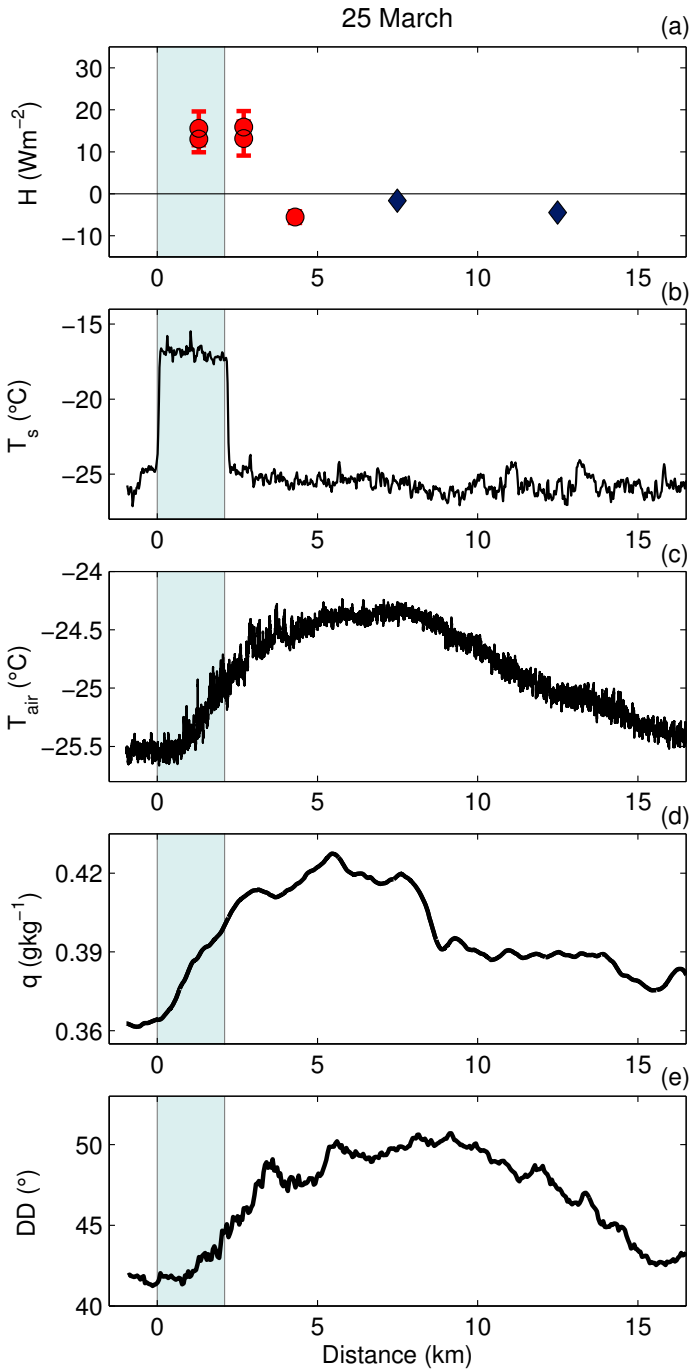

Figure 3.11: **(a)** Sensible heat flux derived from parallel (circles) and cross (diamonds) legs, **(b)** surface temperature, **(c)** air temperature, **(d)** specific humidity, and **(e)** wind direction on the cross leg on 25 March 2013 as a function of the distance to the upstream end of the lead. A running average over a window of 10 s was applied to the wind direction data. A wind direction of 45 ° represents wind from northeast. The flight height is approximately 35 m. The shaded area denotes the lead extent.

turning clockwise from 42° at the upstream lead edge to 51° at 8 km distance and back to 42° at $x = 15$ km (Fig. 3.11e). This turning of the wind direction in the low level flight coincided with the region of the weakened LLJ. From the profiles of the saw tooth flight it is evident that this change was only present in the lowest 60 to 80 m of the ABL (not shown). This might imply

that the change in wind direction was caused by a weaker wind shear related to the change of the LLJ. Such a pronounced change in wind direction was not observed on 11 March.

The profiles of sensible heat fluxes were very similar over the center of the lead and slightly downstream of it (Fig. 3.13b), with positive fluxes of about 15 Wm^{-2} at 35 m height and entrainment fluxes in the same order of magnitude of -21 to -12 Wm^{-2} at 60 m height. Entrainment fluxes were still present at 60 m height further downstream, at a distance of 4.3 km from the upstream edge. Near the surface, however, small negative sensible heat fluxes were found at this position, indicating that this level was already inside the newly developing internal boundary layer over the thicker ice. As in the previous two case studies, intermittent turbulence was observed at heights above the convective IBL.

The near-surface momentum fluxes were also very similar over the lead center and slightly downstream of it, with values of about 0.2 Nm^{-2}, and decreased to 0.1 Nm^{-2} at 4.3 km (Fig. 3.13c). At 60 m height, the maximum of the momentum fluxes of 0.15 Nm^{-2} was found at 2.7 km rather than over the lead center.

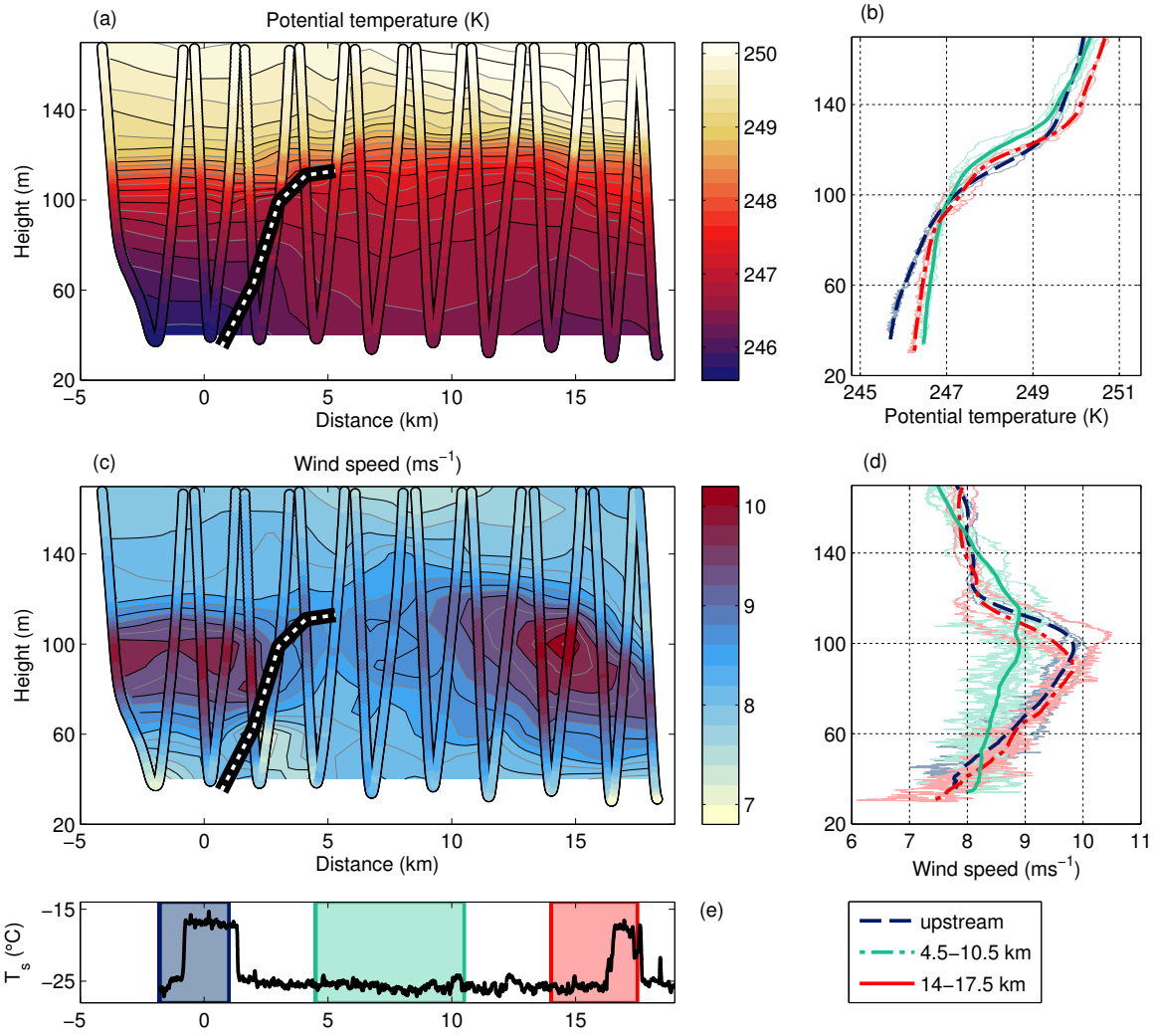

Figure 3.12: Horizontal cross-sections of **(a)** potential temperature and **(c)** wind speed derived from the saw tooth leg on 25 March 2013. The dashed line represents the height of the IBL. Profiles of **(b)** potential temperature and **(d)** wind speed averaged over the regions marked in **(e)**.

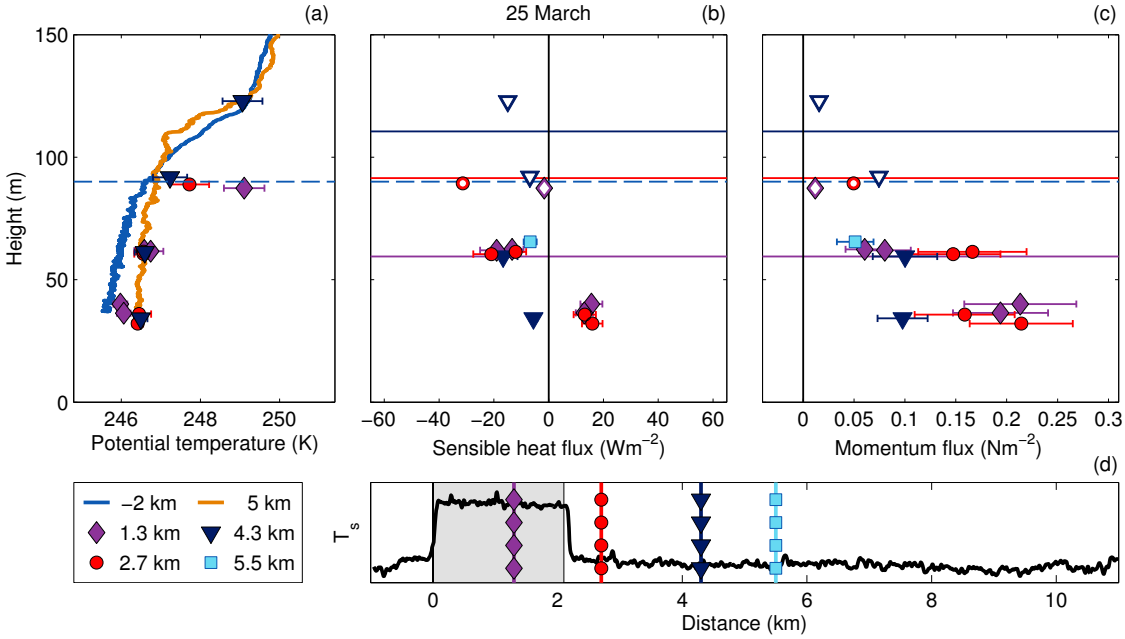

Figure 3.13: Profiles of **(a)** potential temperature, **(b)** sensible heat fluxes and **(c)** momentum fluxes on 25 March. The different symbols and lines represent the distance of the flight leg from the upstream edge of the lead. The positions of the flight legs are indicated in the cross-section of the surface temperature **(d)**. Open symbols mark legs with intermittent turbulence (see text). The horizontal dashed line and the horizontal solid lines mark the upstream ABL height and the IBL heights derived from the potential temperature profiles of the saw tooth leg.

3.2.4 26 March 2013

The lead section on 26 March was the smallest one of all considered cases with a width of 1.6 km and a length of only 5 km (Fig. 3.14). It was only a small part of a much longer lead, which contained, however too many curved sections to have a longer flight section than 5 km. The lead was mostly covered by open water and frazil ice, which resulted in a large surface temperature contrast to the surrounding thick ice of more than 20 °C (Fig. 3.15b) over the open water areas. The flight pattern consisted of a low level flight leg at 35 m height orthogonal to the lead and of four stacks of lead parallel flight legs at different heights over the lead and downstream of it. The wind direction was nearly parallel to the cross leg with a near-surface wind speed around 7.5 ms^{-1}. The near-surface sensible heat fluxes derived from the parallel legs at about 38 m height nicely illustrate the plume propagation (Fig. 3.15a). At the center of the lead ($x = 0.7$ km) upward sensible heat fluxes were relatively small with values of 20 to 30 Wm^{-2}. The reason for these small values is probably that the top of the convective plume had just reached the measurement height. However, large heat fluxes with a maximum of 180 Wm^{-2} occurred at the downstream edge of the lead, at $x = 1.5$ km and the plume impact was still well pronounced at $x = 3$ km where upward fluxes were still between 80 and 115 Wm^{-2}. Further downstream, the fluxes at the lowest flight leg decreased strongly and were around 0 Wm^{-2} at $x = 4.3$ km.

The large sensible heat fluxes caused large fluctuations of the air temperature at 35 m height with amplitudes of up to 1.5 °C (Fig. 3.15c). These fluctuations occurred only between $x = 1$ km and $x = 3$ km, which is in the region with the large upward fluxes. The temperature returned to its upstream value of -25.1 °C at about $x = 3$ km. Concurrently, the specific humidity increased by 0.06 gkg^{-1} to 0.42 gkg^{-1} (Fig. 3.15d). But unlike the temperature signal the humidity remained

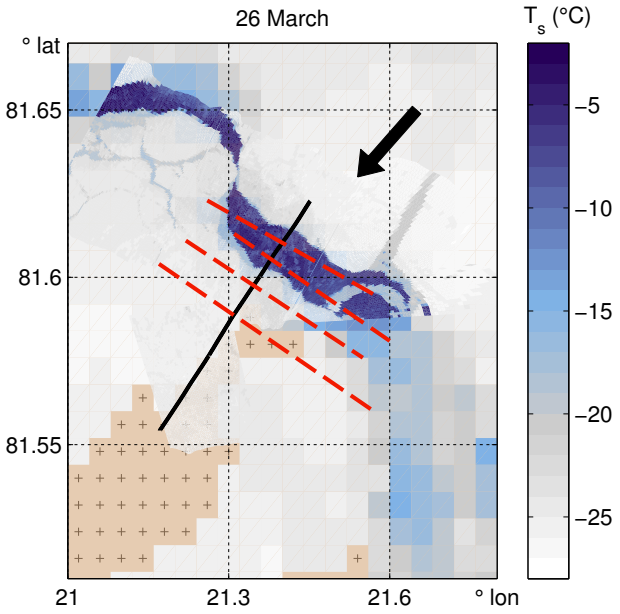

Figure 3.14: Overlay of surface temperatures from MODIS (available through http://reverb.echo.nasa.gov) and the aircraft-based IR-scanner with flight legs orthogonal (solid lines) and parallel to (dashed lines) the lead for the case studies on 26 March. The arrow denotes the wind direction. Pixels marked with crosses represent missing data.

at an elevated level around 0.39 gkg^{-1} up to $x = 4$ km before it started to decrease further downstream.

For this day, we have three positions for profiles of fluxes and mean meteorological parameters derived from the lead parallel flight sections. They were located at the downstream edge of the lead ($x = 1.5$ km) and further downstream at $x = 3$ km and $x = 4.3$ km. In addition, we consider a potential temperature profile derived from an ascent at the upstream side of the lead, at $x =$ -1.5 km.

The upstream potential temperature profile showed a nearly neutral stratification with a temperature gradient of 0.003 Km^{-1} in the boundary layer (Fig. 3.16a) whose top was at about 190 m (not shown). This is a much higher value than in all cases described so far. Consequently, the convective IBL over the lead grew to larger heights than in the other cases. At the downstream edge of the lead, at 1.5 km, there was an unstable stratification up to about 90 m, indicating that the convective IBL had already grown to a height exceeding 90 m. Downstream of the lead, at 3 km, the stratification was nearly neutral with an IBL height exceeding the highest leg at 140 m.

As on 10 March, the plume is also well visible in the profiles of turbulent fluxes (Fig. 3.16b,c). At the downstream edge of the lead, at 1.5 km, sensible heat fluxes (Fig. 3.16b) linearly decreased from 180 Wm^{-2} at 35 m height to 90 Wm^{-2} at 65 m, and to 33 Wm^{-2} at 95 m. Again, intermittent turbulence was found at the uppermost levels at 140 m height. Downstream of the lead, at $x = 3$ km, both the maximum sensible heat fluxes of 130 Wm^{-2} and the maximum momentum fluxes of 0.33 Nm^{-2} were found at 65 m height, rather than near the surface. This behaviour can be well explained with the inclination of the plume's core. Thus, the shape of the flux profiles indicates the presence of a further internal boundary layer growing below the plume over the pack ice downstream of the lead. This shape of the profile with an elevated maximum is still present further downstream, at 4.3 km, but with much smaller maximum fluxes at 65 m height of 21 Wm^{-2} and 0.20 Nm^{-2}, respectively.

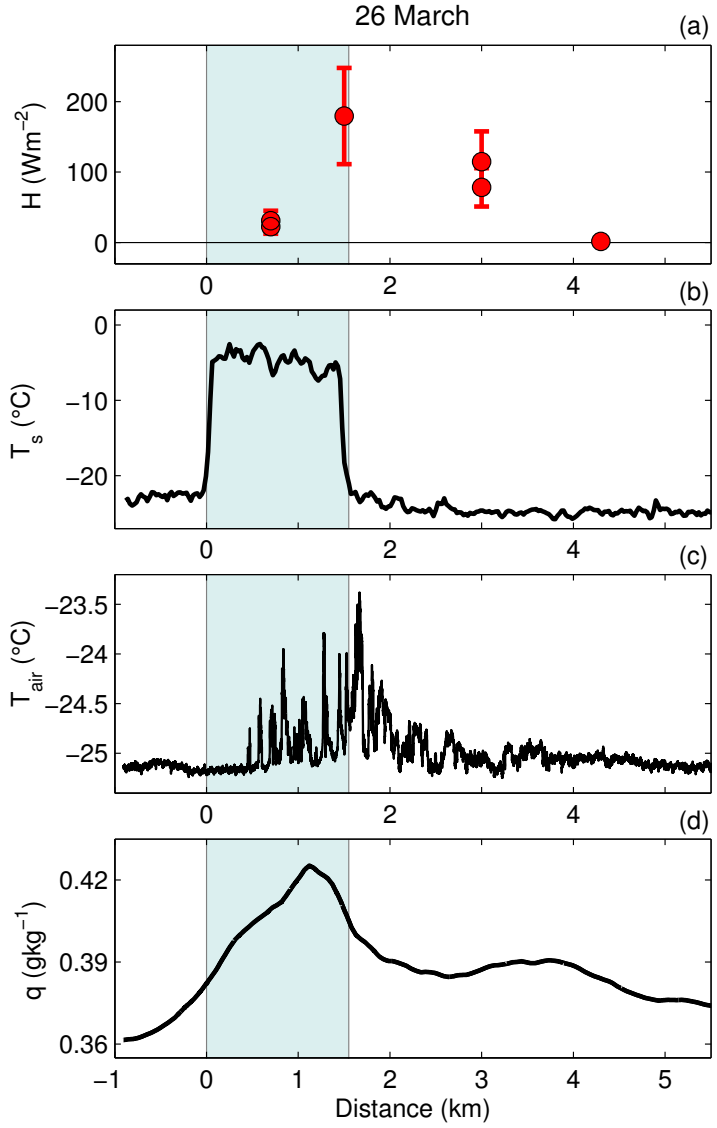

Figure 3.15: **(a)** Sensible heat flux, **(b)** surface temperature, **(c)** air temperature, and **(d)** specific humidity on the cross leg on 26 March 2013 as a function of the distance to the upstream end of the lead. The flight height is approximately 35 m. The shaded area denotes the lead extent.

3.2.5 Atmospheric response to leads

Our four cases show the strong impact of leads on the ABL structure (temperature, humidity, wind) not only near the surface but also throughout the entire ABL. The large differences between the cases document the large impact of external parameters since results differ strongly from each other with respect to the absolute values of fluxes, evolution of temperature and humidity, and boundary layer heights. The variability of processes as a consequence of external forcing parameters points to the difficulties that may arise in climate models when the meteorological forcing (e.g., ABL stratification and height, inversion strength, wind field) and sea ice forcing conditions (e.g., concentration and thickness of nilas) are only roughly reproduced. Differences on 11 March between atmospheric variables over the regions with grey and white nilas show, for example, the dramatic impact that an erroneous thickness of modeled new ice could have.

Especially interesting is the structure of the wind field in the two cases of 11 and 25 March,

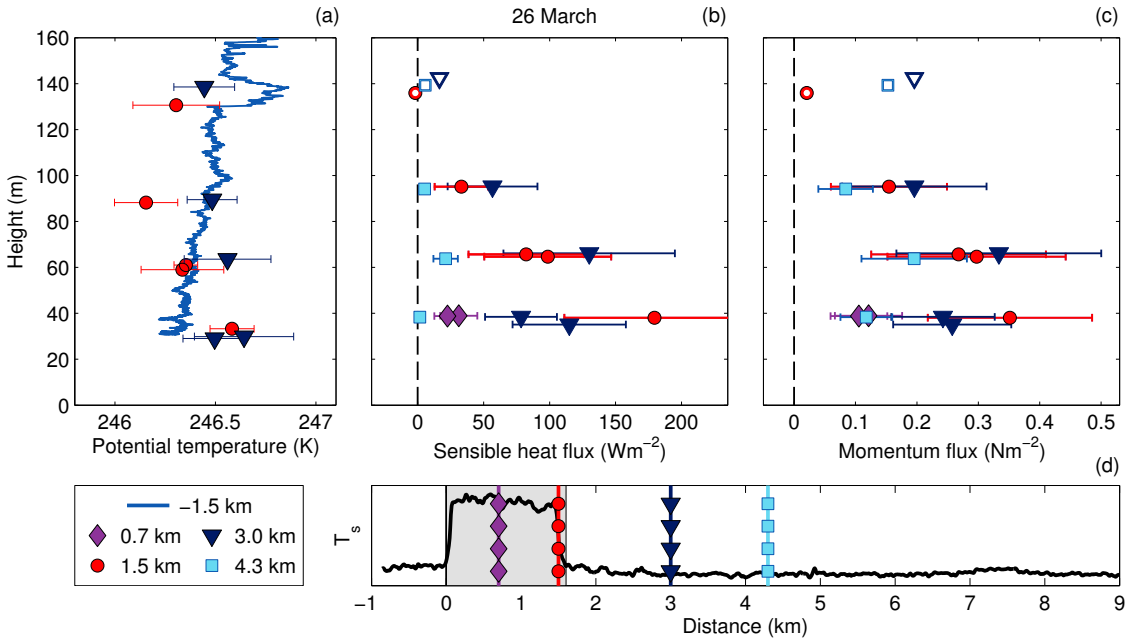

Figure 3.16: Profiles of **(a)** potential temperature, **(b)** sensible heat fluxes and **(c)** momentum fluxes on 26 March. The different symbols and lines represent the distance of the flight leg from the upstream edge of the lead. The position of the flight legs is indicated in the cross-section of the surface temperature **(d)**. Open symbols mark legs with intermittent turbulence (see text). The ABL height corresponding to the upstream potential temperature profile is 190 m (not shown).

where a low level jet was observed in the areas upstream and downstream of the lead. These jets are often found in the Arctic in cases with stable stratification (e.g. Vihma et al., 2014). Our new finding is that they disappeared, however, in the region influenced by the plume. To our knowledge, this kind of interaction has never been documented in previous studies. However, a slight hint to this phenomenon can be found in results of the LES model PALM used in Lüpkes et al. (2008a) (Lu08) showing a very weak LLJ on the upstream side of a 1 km wide lead that disappeared in the plume region. We stress that Lu08 considered a near-neutral stratification in the upstream area so that differences to the observations with stable inflow can be expected and therefore do not point to a model failure.

Dare and Atkinson (2000) modeled the wind fields over large polynyas. In one case they considered a polynya of 30 km width that is comparable in size with our case on 11 March. However, their ABL stratification was also near-neutral in the upstream area and the capping inversion was at a different height (500 m) than on 11 March. This might explain why no LLJ was produced by the model. But it does not explain the large differences concerning the increase in near-surface wind speed which amounted several ms^{-1} over and downstream of the polynyas in the model result compared with the measured increase of less than 1 ms^{-1} on 11 March.

Also the measurements of the plume development and turbulent fluxes can be compared to results of modeling studies. We consider once more the results of Lu08 and another study with PALM carried out by Weinbrecht and Raasch (2001). Both modeling studies differ from each other and from our cases by the external forcing. Even though Weinbrecht and Raasch (2001) modeled the plume growth in a stably stratified ABL, the considered lead was only 200 m wide and the maximum wind speed of 5 ms^{-1} was smaller than values observed in most of our cases. Despite these differences, the observed shape of our heat flux profiles agree well with their model

results. As in their study, we observed - as expected in homogeneous and stationary conditions - linearly decreasing heat fluxes with height over the center of the lead, but an elevated flux maximum over the sea ice area downstream of the lead indicating the core of the plume. Thus, we conclude that non-linear flux profiles can exist in the close environment of leads. These results are also in line with the findings by Lu08 despite the mentioned differences in the lead width and meteorological forcing.

Lu08 pointed out that a local closure is not suitable to model turbulent fluxes over leads. In particular, they found regions of gradient independent and even counter-gradient heat transport in the outer regions of the plume (see their Fig. 5). Despite the large differences in the inflow conditions with respect to stability, we observed indications of this process in our measurements. On 11 March, we observed a near-neutral or slightly stable stratification over the lead below 85 m height concurrent with upward sensible heat fluxes exceeding 50 Wm^{-2}. A similar situation was found on 26 March slightly downstream of the lead ($x = 3\,\mathrm{km}$), where upward heat fluxes were measured between 30 and 60 m height, even though the stratification was near neutral.

Of special interest in our measurements is also the observed entrainment. The plume penetration through the lowest levels of the capping inversion was evident from elevated inversion heights (especially in the case of 10 March) as well as from negative sensible heat fluxes and the presence of intermittent turbulence near the inversion levels. The large impact of the entrainment on the ABL temperature is visible in the case study on 25 March. Here, a large near-surface temperature increase exceeding 1 °C was observed, although the near-surface sensible heat fluxes were smaller than 50 Wm^{-2}. The comparison with the results of a corresponding modeled case in Lu08 (potential temperature increase $< 0.2\,\mathrm{K}$, heat flux 51 Wm^{-2}) shows that such a small flux could not explain this large temperature effect even if the very shallow boundary layer of only 90 m would be taken into account. In addition, the near-surface temperature maximum on 25 March was located about 6 km downstream of the lead, rather than directly at the downstream edge as on 10 March and in the Lu08 case. Such an increase of temperature downstream of the lead cannot be explained by an effect of surface fluxes. Thus, the large observed entrainment fluxes exceeding 30 % of the surface fluxes probably had a large contribution to the observed temperature increase.

3.2.6 IBL growth

The IBL growth derived from the saw tooth patterns of the two case studies on 11 and 25 March can be compared to different parametrisations of the IBL growth over leads and polynyas that are available in the literature. First, we consider a formula by Glendening and Burk (1992) for the maximum penetration height h_{max} of a plume originating from a lead in a stably stratified flow with a height constant potential temperature gradient in the whole layer, rather than for the height of the internal convective boundary layer. It is given by

$$h_{max} = \left(\frac{\overline{w'\theta'}_s \cdot X^2}{v \cdot \frac{\partial \theta}{\partial z}} \right)^{1/3}, \tag{3.1}$$

where $\overline{w'\theta'}_s$ is the surface temperature flux over the lead, X is the lead width, $\partial\theta/\partial z$ is the upstream mean vertical gradient of the ABL potential temperature, and v is the lead orthogonal wind component upstream of the lead. For a validation of this parametrisation we determined $\overline{w'\theta'}_s$ from our measurements by extrapolating the fluxes at higher levels linearly to the surface. Inserting our measurements (see Table 3.2) in Eq. 3.1 we obtained $h_{max} = 380\,\mathrm{m}$ on 11 March and $h_{max} = 120\,\mathrm{m}$ on 25 March. The value on 25 March is close to the observed maximum IBL height of 110 m, while the value on 11 March is much larger than the height of the upstream inversion

Table 3.2: Measurements used to calculate IBL heights

			11 March 2013	25 March 2013
Lead width	X	(km)	8.3 (28.1) [a]	2.1
Temperature flux	$\overline{w'\theta'}_s$	(Kms^{-1})	0.15 (0.06) [a]	0.04
Lead orthogonal wind speed	v, $\lvert\vec{v}\rvert$	(ms^{-1})	10.5	8
Potential temperature gradient	$\partial\theta/\partial z$	(Km^{-1})	0.018	0.014
10 m wind speed [b]	$\lvert\vec{v}_{10}\rvert$	(ms^{-1})	5 (3-7)	4.5 (3-6)
Entrainment rate [b,c]	β		0.09 (0-0.17)	0.28 (0.2-0.35)

[a] grey and white nilas, respectively
[b] values in parentheses give the possible range derived from the measurements
[c] ratio between entrainment flux and surface heat flux

of about 190 m. This illustrates that this parametrisation is only applicable when theoretical maximum plume penetration heights are smaller than the inversion height of the inflow, which is the case, for example, for narrow leads or small surface heat fluxes.

The growth of an internal boundary layer after abrupt changes of surface roughness, and surface temperature and humidity has been the subject in many previous studies. An overview can be found in Garratt (1990) and Savelyev and Taylor (2005). In the following we focus on surface temperature changes only and discuss selected parametrisations of the IBL growth.

A formulation for the upper plume boundary h, which is equivalent to the height of the internal convective boundary layer, as a function of distance to the position of the abrupt surface temperature change has been proposed by Venkatram (1986) for sea-breeze applications as

$$h(x) = z_i \left\{1 - \exp\left(-\frac{x}{bz_i}\right)\right\}^{1/2}. \tag{3.2}$$

In Venkatram's original formula x is a distance over land downstream of open water and he assumes constant upward heat flux over land. For our application over leads we can interpret x as the distance from the lead's upstream edge. The IBL growth is limited by the height of the upstream inversion z_i and thus entrainment within the inversion layer is not accounted for. b is an empirical dimensionless constant that was left to be determined. We can estimate the value of this constant to b = 40-60 over the leads using our IBL heights on 11 and 25 March. However, using these values the IBL height is strongly underestimated in the region downstream of the lead (not shown). Such a deviation can be expected because Vekatram's formula was derived only for the IBL growth over the heated area and not on its downstream side.

This was different in another but similar formulation that was derived by Lu08 for the IBL growth over a small lead. Their focus was on the evolution downstream of the lead and especially on the weakening of turbulence in this area. They arrived at

$$h(x) = z_i \left\{1 - \exp\left(-\frac{x}{D}\right)\right\}^{3/2}, \tag{3.3}$$

where the turbulence decay length scale D is defined as

$$D = \frac{3}{2a}\left(\frac{|\vec{v}|^3}{\frac{g}{\theta_0}\overline{w'\theta'}_s}\right)^{1/3} z_i^{2/3}. \tag{3.4}$$

a is the plume inclination, which they determined to a =2.3 for a neutral upstream stratification and for a lead width of 1 km. In contrast to Glendening and Burk (1992), Lu08 did not include the latter as a parameter in their equation since they considered mainly leads of the same widths. Figure 3.17 illustrates that this model captures the IBL growth reasonably well on 25 March but overestimates the growth rate during the first 3 km on 11 March. This overestimation can be well explained by the neglect of stratification since one can expect that a plume penetrates upward more slowly in a stable environment than under neutral conditions. Using a plume inclination constant of a =0.9 (assuming a more inclined plume) improves the agreement on 11 March. Thus, unlike the parametrisation by Venkatram (1986), the Lu08 parametrisation captures well the IBL growth both over the lead and downstream of it when the parameters are chosen adequately.

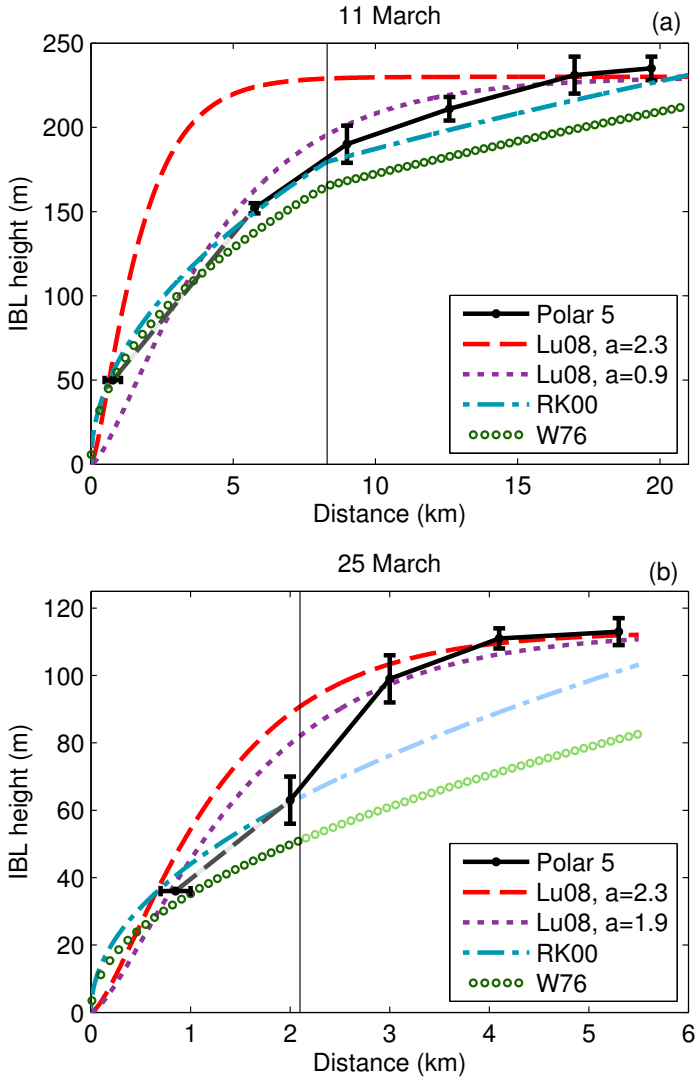

Figure 3.17: Height of the internal convective boundary layer as a function of distance to the lead on **(a)** 11 March and **(b)** 25 March. The full line represents the IBL height derived from the measurements and their uncertainty range. The IBL height calculated using the formula by Lüpkes et al. (2008b) with original plume inclination a is given as a dashed line and with adjusted a as a dotted line. The dashed dotted line represents the model by Renfrew and King (2000) and the circle line the model by Weisman (1976) with the values specified in Table 3.2.

Other models of the IBL growth suggest a dependence of h on the square root of the fetch x. For the growth of a thermal IBL over land during sea-breeze conditions Weisman (1976) (W76) proposed

$$h(x) = \sqrt{\frac{2 \cdot \overline{w'\theta'}_s}{\frac{\partial\theta}{\partial z}|\vec{v}_{10}|} \cdot x}, \tag{3.5}$$

where $|\vec{v}_{10}|$ is the wind speed at 10 m height. A similar analytical formulation can be derived using a model that was developed for the IBL growth over polynyas by Renfrew and King (2000) (RK00). Assuming constant surface fluxes, their equation for dh/dx can be analytically integrated. This results in Eq. 3.5 but multiplied with a factor $\sqrt{1+2\beta}$ where beta is the entrainment rate they introduced.

It is important to note that in this model x denotes the fetch over the polynya or lead area and therefore it is not applicable downstream of a lead. To determine h we used constant surface fluxes derived from our measurements (Table 3.2). Note that $\overline{w'\theta'}_s$ is x-dependent in the original formulation by RK00, while we used a constant value over the lead. The same value was also used to extrapolate the solutions to the downstream region for which the model was not developed originally.

Near-surface input values for $|\vec{v}_{10}|$ can only be determined very roughly from our aircraft measurements in or above 30 m height. It is also challenging to derive β from our measurements at discrete heights because we might not have captured the heights of the maximum entrainment flux. Nevertheless, we found that choosing these values in the range given in Table 3.2 suggested by our measurements the modeled IBL growth agrees very well over the leads on 11 March and on 25 March. On the downstream side, the extrapolation (see above) on 25 March underestimates h by up to 25 % at 3 and 4 km distance and reaches the capping inversion 1 km later than observed (Fig. 3.17).

It is evident from comparing the IBL growth using the models by RK00 and W76 that entrainment is an important factor. The W76 model without entrainment underestimates the growth speed of the IBL already over the lead (Fig. 3.17). On 25 March, where the entrainment rate amounted to about 30 %, the IBL height at $x = 2$ km was underestimated by 10 to 20 %.

3.3 Calculation of turbulent fluxes for horizontal flight legs

As mentioned in Sect. 3.2, profiles of turbulent sensible heat and momentum fluxes were derived from the flight legs parallel to the leads at different heights and different distances to the inflow margin. In the following sections, we describe details of the flux calculation procedure, error estimation, and data quality control. Furthermore, we analyze the optimal length of the flight legs used to derive turbulent fluxes and compare fluxes obtained from flight sections parallel and perpendicular to the leads.

3.3.1 Flux calculation and sampling error

Using the fast measurements of the nose boom we applied the eddy covariance method to calculate turbulent fluxes of heat (H) and momentum ($\boldsymbol{\tau}$), where H is given by

$$H = \bar{\rho} c_p \overline{w'\theta'}. \tag{3.6}$$

The prime denotes the turbulent fluctuations, $\bar{\rho}$ is the mean density and c_p =1005 J kg^{-1} K^{-1} is the specific heat capacity of air. For measurements at a fixed location the bar denotes temporal averaging. Assuming horizontal homogeneity and stationarity, this can be transformed to a spatial averaging for measurements from a moving platform, such as an aircraft. The surface

stress vector is

$$\boldsymbol{\tau} = (\tau_x, \tau_y) = -\bar{\rho}(\overline{u'w'}, \overline{v'w'}), \tag{3.7}$$

with the turbulent fluctuations u' and v' of the horizontal wind components. In the following, we consider the absolute value of the turbulent momentum flux:

$$|\boldsymbol{\tau}| = \bar{\rho}\sqrt{\overline{u'w'}^2 + \overline{v'w'}^2}. \tag{3.8}$$

An often used method to estimate the sampling error of turbulent fluxes has been suggested by Sreenivasan et al. (1978). It was derived from estimates of the integral time scale of the flux under stationary and near-neutral conditions. The relative sampling error is then given by

$$\varepsilon = \alpha\sqrt{\frac{z}{U\gamma}}, \tag{3.9}$$

where z is the measurement height, γ is the sampling interval, and U is the advection speed of the air along the measurement probe, that is the ground speed of the aircraft. α is an empirical constant that has been determined to $\alpha = 5$ for sensible heat flux under convective conditions over the Ronne Polynya by Fiedler et al. (2010). We used the same value for momentum flux since the results by Sreenivasan et al. (1978) suggest that α for momentum flux should not be larger than α for heat flux.

3.3.2 Data quality control and filtering

The complex shapes of leads pose difficulties in measuring turbulent fluxes since one requirement for using the eddy covariance method is horizontal homogeneity. When the inflow boundary of the lead is not straight the assumption of horizontal homogeneity is not always valid, as can be seen for the lead on 25 March in Fig. 3.18a.

Here, the geometric shape of the lead caused different fetch lengths over the lead along the flight legs parallel to the outflow boundary. This means that in case of a longer fetch (position P2 in Fig. 3.18b) the convective IBL at the aircraft position had already grown further and the near-surface temperatures were already higher than at positions with a smaller fetch (P1). The two positions marked in Fig. 3.18a had fetch lengths of 2 and 3 km, respectively, resulting in an air temperature difference of 0.7 °C. This caused a pronounced temperature variability along the flight section with horizontal wavelengths of about 4 to 5 km superimposed by microscale temperature fluctuations. This effect was observed in both flight legs and, less pronounced but still visible, also at higher altitudes (not shown). The time difference between the lowest and the highest legs was about 30 min, which indicates that this variability on a scale of about 4 km was caused by the lead geometry rather than by a non-stationary temperature field.

The impact of the curved inflow boundary was also visible in the frequency weighted cospectra of vertical wind and potential temperature (Fig. 3.18c,d, solid blue lines represent the unfiltered data), where there is power at low frequencies below 0.1 Hz. This additional power had mostly positive values for leg 1 and mostly negative values for leg 2 resulting in a large difference of the sensible heat fluxes for these two legs of about an order of magnitude (see below). Further insight into this issue can be gained by looking at ogives (Friehe et al., 1991). These are given by the cumulative integration of the cospectrum between the highest measured frequency and the lowest frequency:

$$O_{w,x}(f) = \int_{\infty}^{f} Co_{w,x}(\tilde{f})d\tilde{f}. \tag{3.10}$$

Here, x can be replaced by θ, u, or v for fluxes of sensible heat or momentum, respectively.

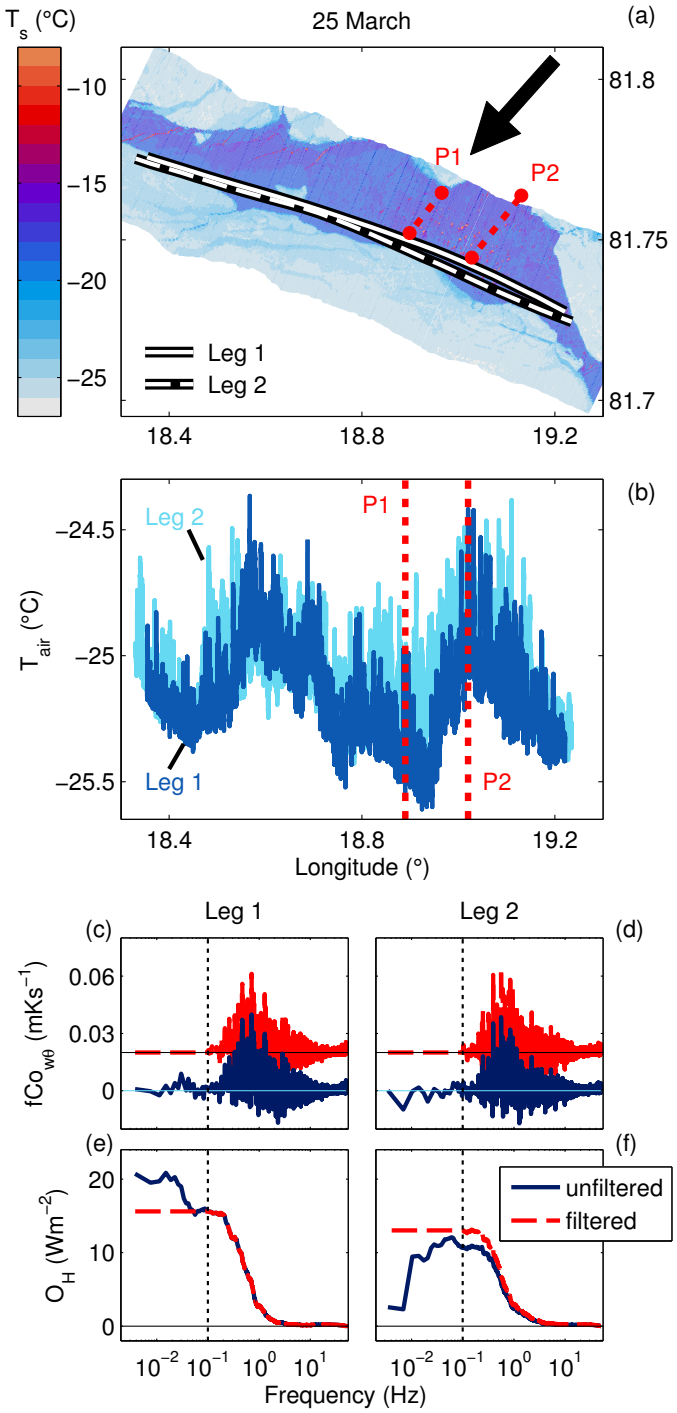

Figure 3.18: **(a)** Surface temperatures of the lead on 25 March 2013 measured with the IR-scanner. The solid and dashed lines represent two flight legs at 35 m height, the arrow denotes the wind direction and the dotted lines indicate the fetch over the lead. **(b)** Air temperatures along the two lead parallel flight legs. The dotted lines mark the same positions as in **(a)**. Frequency weighted cospectra of vertical wind and potential temperature for leg 1 **(c)** and leg 2 **(d)**. High-pass filtered cospectra at 0.1 Hz are additionally shown with red dashed lines. They are offset by 0.02 Kms^{-1} for clarity. Ogives for the sensible heat flux $H = \bar{\rho} c_p \overline{w'\theta'}$ for leg 1 **(e)** and leg 2 **(f)** derived from the original (blue lines) and filtered (red lines) cospectra.

Multiplying $O_{w\theta}$ with $\overline{\rho}$ and c_p gives the cumulative sensible heat flux (Fig. 3.18e,f, blue lines). The flux values of the unfiltered curves amount to 20.7 Wm^{-2} for leg 1 and 2.6 Wm^{-2} for leg 2. For stationary conditions, however, the values should be very similar for both legs and the ogives should resemble an S-shape.

We account for this heterogeneity induced by the curved upstream lead edge affecting the local fetches over the lead by applying a filter to the data. From Fig. 3.18c,d it is evident that the unfiltered ogives of the two legs are very similar for frequencies above 0.1 Hz but differ substantially for lower frequencies. Therefore, we choose a high pass filter with a cut-off frequency of 0.1 Hz and assume that all power in lower frequencies was only caused by the heterogeneity and not by other mesoscale phenomena. After filtering, the ogives (Fig. 3.18e,f, red lines) derived from the two legs agree much better and also the sensible heat fluxes with values of 15.6 and 13.0 Wm^{-2} differ only slightly between the two legs. Thus in the following, all data used for the flux calculations are high-pass filtered with a cut-off frequency at 0.1 Hz.

With a ground speed of the aircraft of about 64 $m\,s^{-1}$ a cut-off frequency of 0.1 Hz means that all structures larger than 640 m are neglected. But since the typical size of large convective eddies is 2.5 z_i (see also Fig. 3.19), where z_i is the mixed layer height, and z_i = 100-250 m in each of the four lead cases, we still account for the effect of these large eddies in the fluxes when this cut-off frequency is used.

Before calculating turbulent fluxes we applied a data quality control to all flight legs as in Friehe et al. (1991), Petersen and Renfrew (2009), and Fiedler et al. (2010). It included inspection of the power spectra of potential temperature and the components of the wind vector, the cumulative summation of the covariances, frequency weighted cospectra, and ogives.

Examples of power spectra for θ, u, v, and w are shown in Fig. 3.20a-d, respectively. The power spectra of the wind components decay with a slope of -5/3, as expected in the inertial subrange. This decay is clearly visible over two orders of magnitude, which documents the high quality of our turbulence probe. The power spectra for potential temperature show a slight drop for frequencies above 5 Hz, which points to a too slow sensor response for these wavelengths. However, these high frequencies only have negligible contribution to the total flux, as can also be seen in the ogives (see below, Fig. 3.20g).

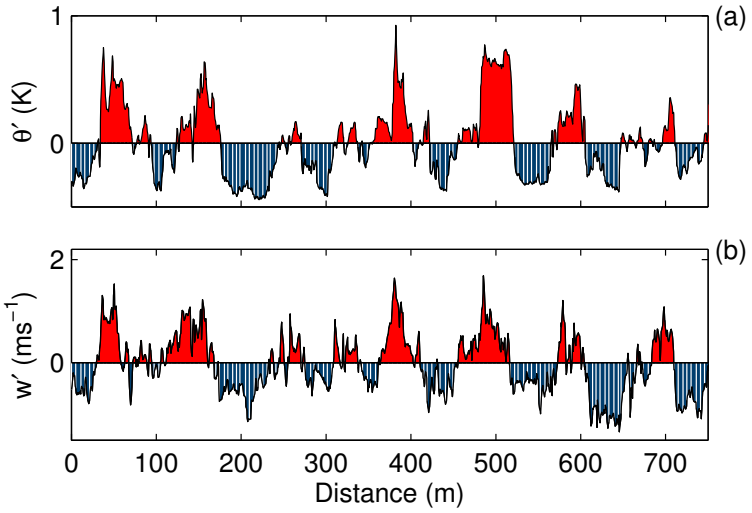

Figure 3.19: Turbulent fluctuations of potential temperature **(a)** and vertical wind **(b)** on parts of the low-level flight leg at 40 m height over the center of the lead at x = 1.5 km on 26 March.

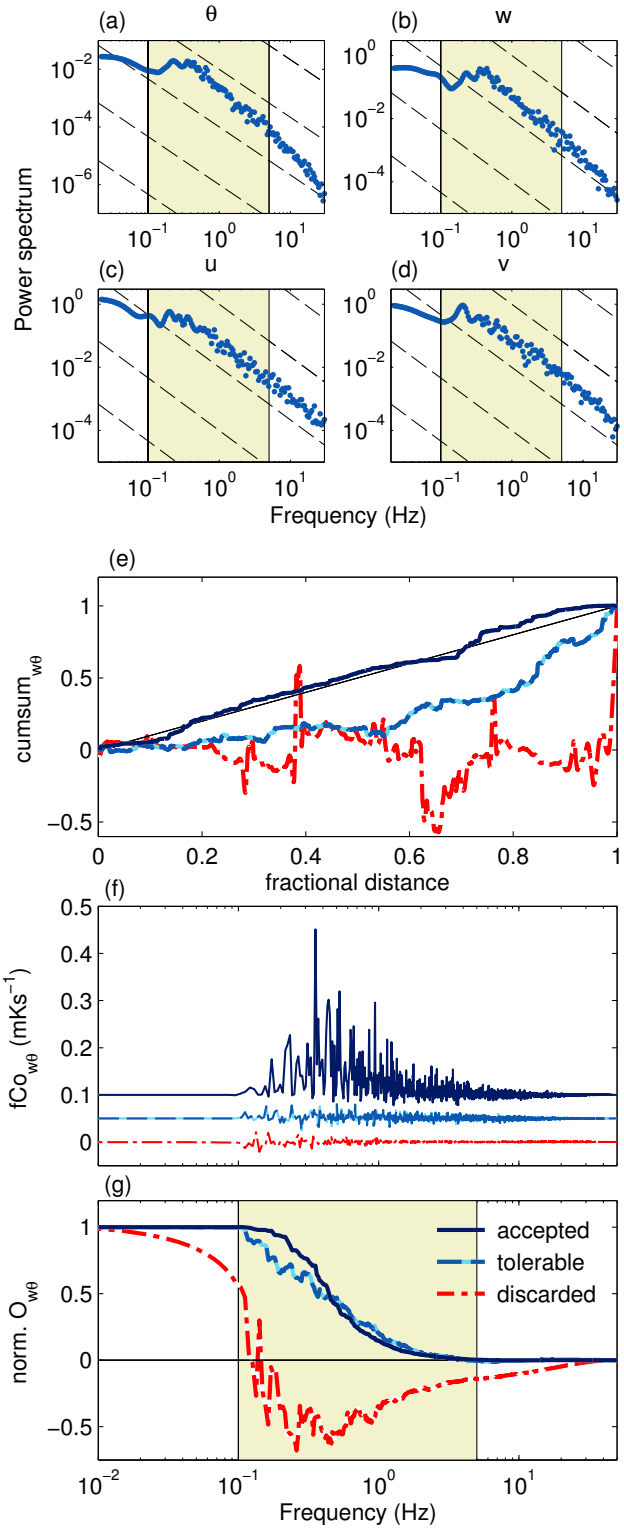

Figure 3.20: Power spectra of **(a)** potential temperature θ, **(b)** vertical wind w, and horizontal wind components **(c)** u and **(d)** v. The dashed thin lines in **(a)** - **(d)** represent the $f^{-5/3}$-slope. The shaded area marks the energy containing eddies. Further parts show **(e)** the cumulative sum of the covariance of w and θ normalized by the total covariance, **(f)** the frequency weighted cospectrum of w and θ, and **(g)** ogives of w and θ normalized by $\overline{w'\theta'}$. The different lines in **(e)** - **(g)** represent cases that were accepted (solid), tolerable (dashed) or discarded (dashed-dotted). The lines in **(f)** were offset by 0.05 mKs^{-1} for clarity.

The further quality control was based on the remaining quantities mentioned above. In the following, we show an example of our quality check with results for three flight legs, one with accepted data quality, another with just tolerable quality, and a third one which had to be discarded according to our criteria.

Figure 3.20e shows the cumulative sum of the covariances normalized by the total covariance. A constant slope indicates horizontally homogeneous fluxes. Flight legs with strongly changing slopes were discarded. In addition, frequency weighted cospectra (Fig. 3.20f) were inspected. For the calculation of the cospectra, the data were high-pass filtered with the cut-off frequency of 0.1 Hz for reasons already discussed above.

In general, it is evident from the ogives (Fig. 3.20g) that mostly frequencies between 10^{-1} Hz and 5 Hz contribute to the flux. Flight legs for which the ogives did not show a smooth S-shape were also discarded. In some cases the ogives were not completely smooth and the cumulative sum of the covariances showed small changes of the slope. We considered these cases as still "tolerable" and used them for the flux calculations.

3.3.3 Minimum leg length

Due to the large variability of a flow in convective conditions it is necessary to evaluate the minimum length of a flight leg over a lead that is required to get an accurate estimate of the turbulent fluxes. For this purpose, we divided the lead parallel flight legs into shorter sublegs and compared the average flux of the sublegs to the flux derived from the total length of the flight leg.

Figure 3.21 shows the turbulent fluxes of sensible heat and momentum averaged over all sublegs as a function of the length of the sublegs. To make results from different flight legs comparable the fluxes were normalized by the flux values derived from the total length of the legs without any splitting into sublegs. All flight legs of the four case studies that passed the quality control were used.

For sensible heat flux, averages of sublegs larger than 2.5 km deviate by less than 1 % from fluxes derived from the total leg length. However, they diverge strongly for smaller subleg lengths. For momentum flux, the spread is larger, with deviations of 2 % for leg lengths larger than 4 km in most considered cases. About 15 % of the considered cases, however, only agree within 7 %. Thus, we confirm the well known result (Kaimal and Finnigan, 1994) that the accuracy is higher for sensible heat flux than for momentum flux. Furthermore, these results confirm that, in homogeneous conditions, our shortest lead on 26 March with a length of only 5 km is long enough to derive fluxes with a sufficient accuracy.

The above analysis of minimum leg lengths cannot include the statistical error that arises due to non-homogeneity of the local fluxes along the whole length of individual leads. We estimated this effect by using sublegs of 2.5 km length and consider the flight legs over leads altogether. It was found that the standard deviation of the sensible heat fluxes related to each leg and then averaged over all 33 available horizontal legs is roughly 40 % of the leg averaged flux. The variability is slightly smaller for momentum fluxes with subleg lengths of 4 km. Here, the average standard deviation within each flight leg was only about 30 %.

3.3.4 Fluxes derived from cross legs

Measurements of the surface energy budget over a large sea ice covered region could be most effective when the flight patterns could be restricted to long transect flights directed straight ahead and crossing a large number of different leads. However, this is only possible when an arbitrary orientation of a flight track relative to the orientation of a lead is sufficient for the determination of fluxes. In order to estimate the uncertainties associated with this method, we

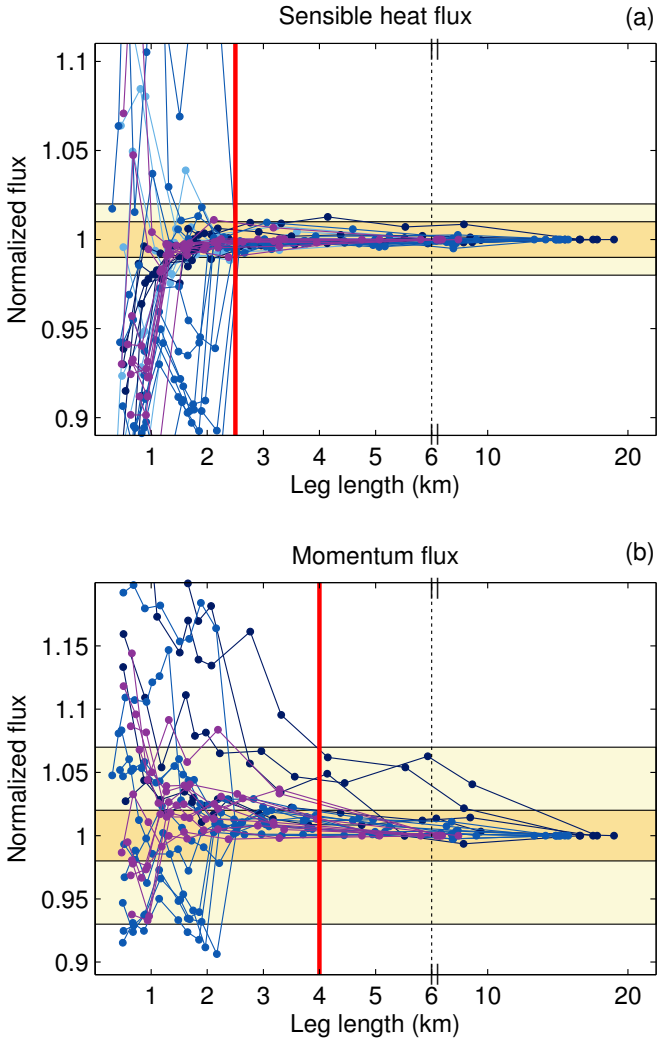

Figure 3.21: Averages of turbulent fluxes of **(a)** sensible heat and **(b)** momentum derived from total flight legs divided into sublegs. The flux is normalized by the value of the undivided leg and plotted as a function of leg length. The shaded areas denote the 1 and 2 % intervals **(a)**, and 2 and 7 % intervals **(b)**, respectively. The red vertical lines mark the derived minimum leg lengths of 2.5 km **(a)** and 4 km **(b)**, respectively.

compared sensible heat fluxes derived from parallel and cross legs to each other. Figure 3.22 exemplarily shows running averages of the sensible heat flux of the cross legs on 25 and 26 March at about 35 m height. We used averaging intervals of 0.5, 1, 2.5, and 4 km.

For the cross leg on 25 March (Fig. 3.22a), averaging lengths of 0.5 and 1 km are too short since they induce an oscillation of the fluxes around zero. On the other hand, using an averaging length of 4 km produces maximum fluxes of only 5 Wm^{-2} rather than 15 Wm^{-2}. An averaging length of 2.5 km, which is the minimum leg length derived in Sect. 3.3.3 and also the approximate width of the lead, only slightly underestimates the fluxes but does not reproduce the plume extent at the downstream edge of the lead.

An averaging length 2.5 km also reproduces the heat fluxes best on 26 March (Fig. 3.22b). However, it does not capture the asymmetric shape of the plume and therefore overestimates the fluxes over the lead center and underestimates the fluxes downstream of it. Here, the value of the maximum flux is very sensitive to the choice of the averaging length. While 2.5 km reproduces

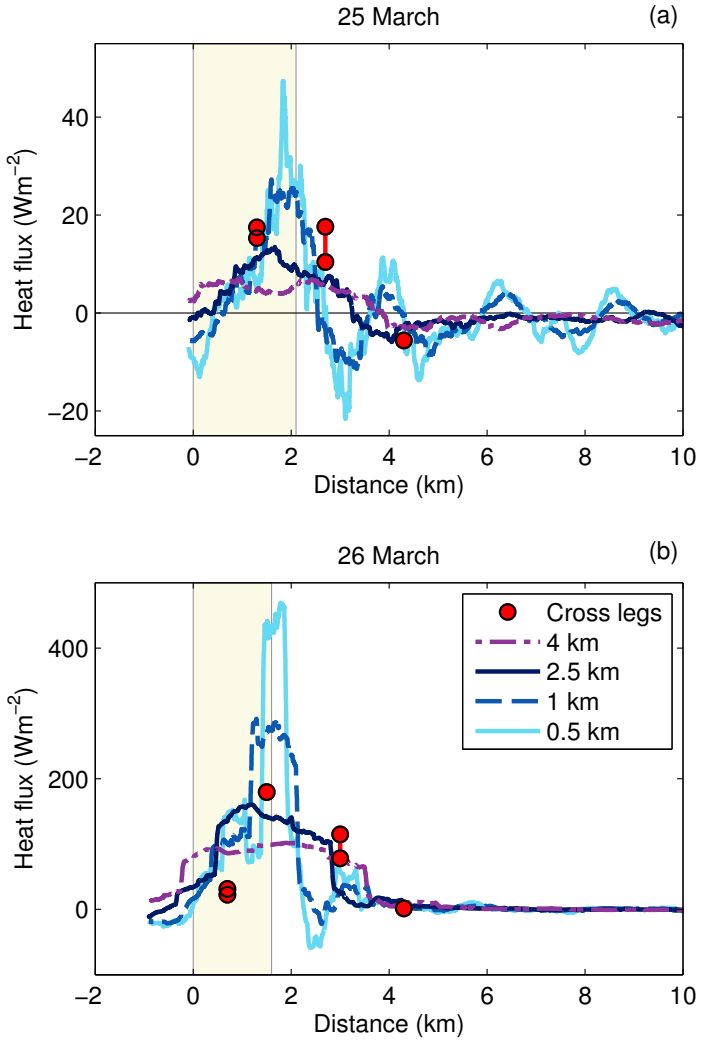

Figure 3.22: Turbulent sensible heat fluxes derived from the low-level cross legs on **(a)** 25 March and **(b)** 26 March. The lines represent different intervals of the moving average. The dots are flux values derived from the lowest parallel flight legs. The shaded areas mark the extent of the lead.

the flux of about 180 Wm^{-2} reasonably well, using an averaging length of only 1 km would cause an overestimation of 100 Wm^{-2} or 55 %. One can also expect that the optimal averaging length depends on the lead width. Therefore, we conclude from this analysis that the long parallel flight legs are indeed necessary to quantify fluxes over leads.

3.3.5 Conclusions on flight leg selection

The advantage of the four case studies presented in the previous sections compared with earlier airborne campaigns (Lüpkes et al., 2012b; Brümmer and Thiemann, 2002) was that the large range of the used aircraft allowed a combination of lead-orthogonal and lead-parallel flight sections, which were in some cases supplemented by a saw tooth pattern orthogonal to the lead. By this combination we obtained measurements representing the most detailed airborne investigation of the lead effect on the atmospheric boundary layer that is - to our knowledge - currently available.

We have shown that lead-parallel flight sections are necessary especially for the derivation of turbulent fluxes since they are very sensitive to the chosen averaging lengths. Large differences of up to 150 % were found between sensible heat fluxes derived from lead-parallel and lead-orthogonal flights. Thus large errors may result when sensible heat fluxes are determined along a straight transect flight of e.g. 100 km length over sea ice with leads without any specific lead pattern included. Depending on parameters like the lead size, true fluxes could be strongly overestimated but also underestimated. This finding is important when model results are compared with previous aircraft measurements based only on straight flight sections.

However, also the lead-parallel sections have to be considered with caution when relatively narrow leads are studied. Difficulties occurred due to the often curved structure of leads that causes large fluctuations of fluxes (see Sect. 3.3.2) by the sudden changes of fetch lengths over the lead area. We have approached this problem by the application of adequate filtering to the data. Furthermore, we also observed inhomogeneous fluxes caused by changing ice cover or heterogeneous upstream conditions along the leads.

We found that, assuming homogeneous conditions, the minimum required leg length to accurately derive turbulent fluxes over leads is about 2.5 km for sensible heat fluxes and about 4 km for momentum fluxes. Since the length of our flight sections along the leads were in some cases close to the required minimum flight length, we encountered large sampling errors. An alternative strategy for future investigations could consist of a repetition of the same tracks to reduce the statistical error. However, the drawback of this method is the reduction of flight time that is available for an additional investigation of the lead impact in the wider lead environment.

In addition, it is very useful to measure fluxes at more than one height. The measured fluxes on 25 March showed that it is difficult to derive sensible heat fluxes at 10 m height from only one flight leg at one height inside the IBL. For very shallow boundary layers and when entrainment is present it is not sufficient to extrapolate the profile linearly on the basis of two values, which are the measured flux at only one level and the flux at the inversion base that is assumed to be zero. We have shown that e.g. on 25 March this would have caused an underestimation of the heat flux at 10 m height by about 40 %.

Finally, we stress that important findings were not based on flux measurements alone, but horizontal flights at one level together with saw tooth patterns provided sufficient data to investigate the lead impact on the ABL on the basis of mean values of meteorological parameters. Such data can be helpful also as a basis for high resolution modeling.

3.4 Regional impacts of lead ensembles

In Sect. 3.2 we demonstrated the strong impact of leads on the atmospheric boundary layer in a downstream region of up to 30 km, while in this section we address the atmospheric impact of lead ensembles on regional scales of up to 300 km.

The climate models used for the fifth assessment report of the IPCC (Intergovernmental Panel on Climate Change), which are combined in the fifth phase of the Coupled Model Intercomparison Project (CMIP5) have resolutions of the atmospheric model components ranging from 0.5 to 4° with a median of about 1.3° (Taylor et al., 2012). The resulting grid sizes of 50 to more than 200 km are much larger than the widths of the four leads of up to 8.3 km that were studied in Sect. 3.2. This also holds for most reanalyses, such as ERA-Interim (Dee et al., 2011) or the NCEP/NCAR reanalysis (Kalnay et al., 1996) with horizontal resolutions of about 80 and 200 km, respectively. Even the Arctic System Reanalysis (Bromwich et al., 2009), which is currently the reanalysis with the highest resolution of about 30 km in the Arctic, can only treat very large leads explicitly, while the largest number of smaller leads remains sub-grid scale. Thus, to account for the regional impacts of lead ensembles the effect of the individual leads has to be parametrised in these models.

To demonstrate the importance of lead ensembles for the regional energy balance we analyze the impact of the lead concentration along selected flight legs (see Fig. 3.23) on the evolution of the near-surface atmospheric temperatures (Sect. 3.4.1). There, we find a warming in regions with a large lead coverage and a cooling when no leads are present. We analyze these regions of cooling and the associated downward sensible heat fluxes in more detail in Sect. 3.4.2.

One approach for a better representation of leads in models is the introduction of different ice thickness classes within each model grid cell. It is already implemented in some coupled climate models, such as CCSM3 (Community Climate System Model version 3, Holland et al., 2006) or CIOM (Community Ice-Ocean Model, Yao et al., 2000), for example. The thin ice forming on refreezing leads and the resulting heat transfer to the atmosphere is thus to some

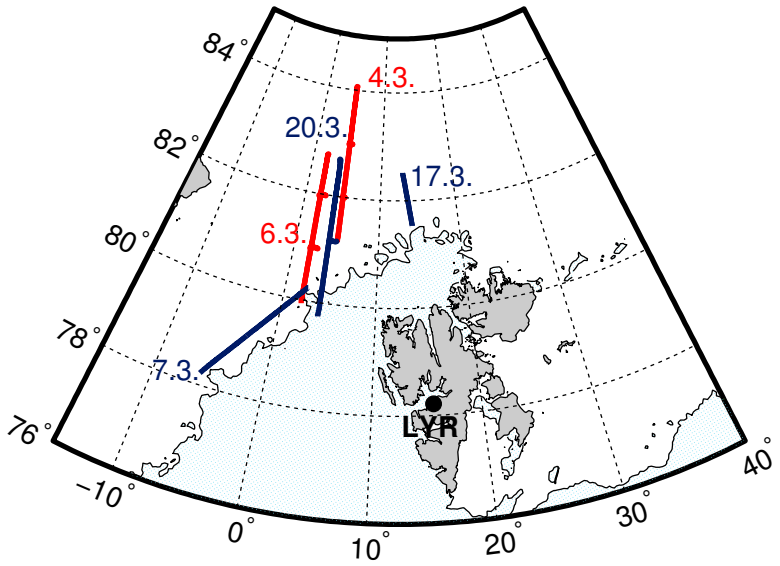

Figure 3.23: Flight tracks of the long low level flight legs on 4, 6, 7, 17, and 20 March 2013 used to derive lead characteristics (all, see Sect. 3.4.3) and to derive the large scale lead impact on near-surface atmospheric temperatures (red, see Sect. 3.4.1).

extent accounted for in these models. However, as already discussed in the introduction of this chapter (Sect. 3.1), different studies have shown that the heat transfer over leads also depends on the fetch and thus on the lead width and orientation within the grid cell. A first step towards accounting for the fetch dependence could be to include a sub-grid lead width distribution in the model. Therefore, we derive distributions of lead width and lead surface temperature in Sect. 3.4.3 and compare them to values in the literature. These distributions are based on the long low level flight legs of the five days indicated in Fig. 3.23.

3.4.1 Impact of lead concentration on atmospheric temperatures

It is already evident from the measurements of air and surface temperature of the low-level flight leg on 6 March that the air temperature is closely related to the area covered by leads (Fig. 3.24a). As discussed in detail in Sect. 3.2 and as shown in Fig. 3.24b,c, the air temperature usually increases in the first kilometers downstream of a lead and decreases again further downstream over regions with mostly closed sea ice cover. The aim of this section is to quantify the average impact of a lead ensemble on the near-surface air temperature. For the investigation we consider the long low-level flight legs on 4 and 6 March, where the winds were parallel to the flight legs with a cold off-ice flow. Due to the resulting large temperature differences between the air and the surface, we expect large sensible heat fluxes and thus a large lead impact under these conditions. Since the flights took place under nearly cloud-free conditions, we can exclude the cloud impact from our considerations.

We use an approach similar to the one used in a modeling study by Lüpkes et al. (2008b) (Lu08) who coupled a thermodynamic sea-ice model to a one-dimensional atmospheric model. The model was run for 48 h with constant prescribed ice concentrations between 90 and 100 % in steps of 1 %. They found that a decrease of ice concentration of 1 % caused an increase of the 10 m air temperature of 1 °C after 12 h model run time and of 3.5 °C after 48 h (their Fig. 4). The results of th 1D model can also be considered in a Lagrangian way, assuming that the model box is transported over a region with constant ice concentration. The distance travelled during the model run time is then determined by the wind speed.

To compare the results from our measurements to the model results with a constant ice concentration by Lu08 we divide the long flight sections into shorter sublegs with nearly constant ice concentration and air temperatures. To keep the air temperature changes within each subleg small the sublegs should not be too long. However, the sublegs also have to be long enough to include the effect of wider leads. These conditions result in a length of the sublegs in the order of 20 km.

The temperature changes found by Lu08 depend on the model run time, this means on the length of the time interval at which the air is in contact with the surface. For comparison of the Lu08 results with the observed cases it is necessary to define such an "interaction time" also for our measurements. We define it as the time interval that an air-parcel spends within each grid cell and calculate it using the measured wind speed. For the average wind speeds measured at 50 m height of about 11.5 $m s^{-1}$ on 4 March and 10 $m s^{-1}$ on 6 March, an interaction time of 30 min is appropriate for both days. This results in a length of the averaging intervals of 21 km on 4 March and 18 km on 6 March.

For the following analysis we use the sea ice concentration (SIC) and the air temperature averaged over each averaging interval. In principle, open water areas could be identified from the visible images of a downward looking photo camera that was mounted on the Polar 5 aircraft. However, it would be more difficult to detect areas covered by thin ice, especially, when a thin snow cover is present. To account also for these thin ice areas, we use the ice surface temperature measurements of the KT-19 (T_s) to derive the average ice concentration (SIC) within each averaging interval. Assuming a linear relationship between surface temperature and SIC, the SIC

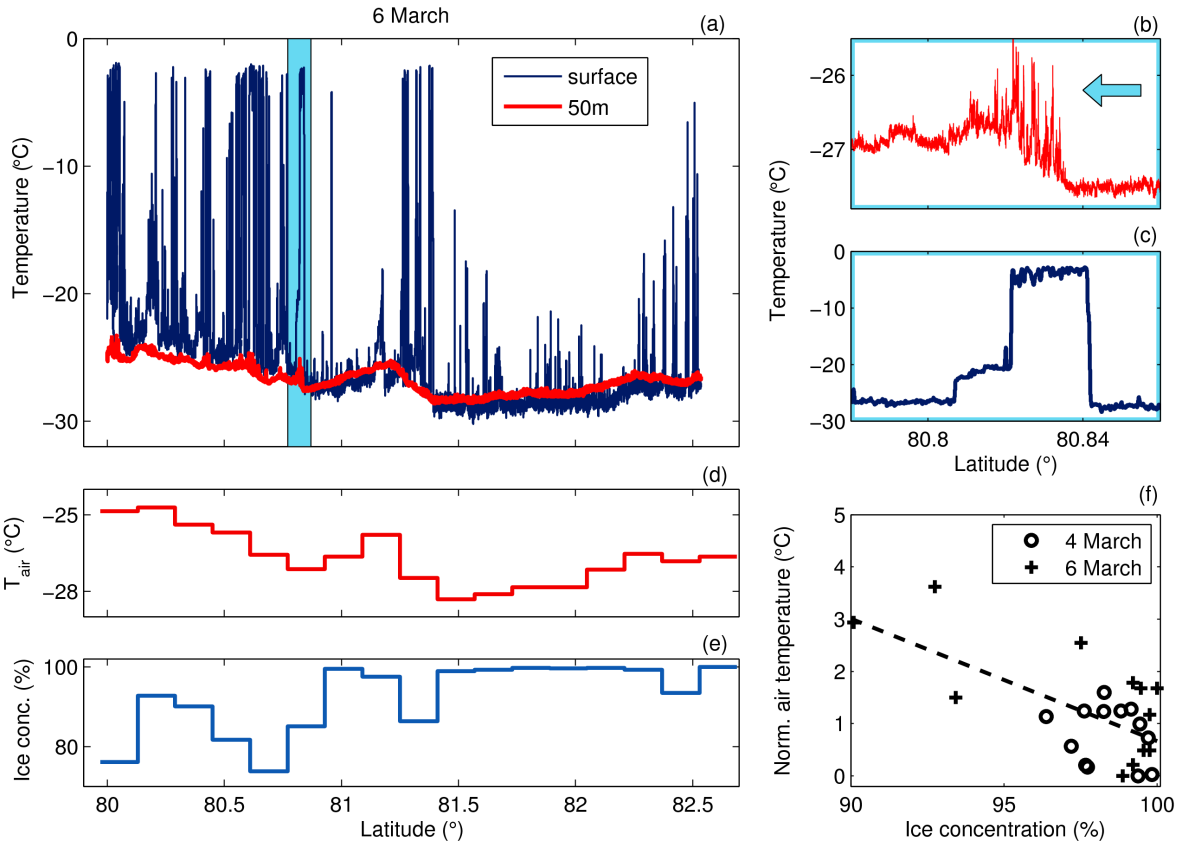

Figure 3.24: Near-surface temperature (red) and ice surface temperature (dark blue) on 6 March 2013 for **(a)** the whole flight leg and **(b,c)** a zoom in. **(d)** Spatial averages of the air temperature and **(e)** derived ice concentration on 6 March. **(f)** Relationship between ice concentration and near-surface air temperatures scaled with their minimum value for 4 and 6 March.

can be determined as:

$$\mathrm{SIC}(T_s) = \frac{T_w - T_s}{T_w - T_i}. \tag{3.11}$$

Here, T_w =-1.8 °C is the temperature of open water and the surface temperature of thick ice T_i is determined as the lowest 30 % of the ice surface temperature values inside the averaging interval. Since in this approach thin ice covered areas are treated as areas that are partly covered by open water and partly by thick ice, the resulting SIC is only an "effective ice concentration" and does not represent the actual open water fraction. The single SIC values are then averaged within each averaging interval. Examples of the averaged air temperatures and the derived effective ice concentrations are shown in Fig. 3.24d and e, respectively. To be able to compare data from different days, we scaled the air temperature by subtracting its minimum value along the whole considered flight track.

As in Lu08, we then compared the scaled air temperature to the effective ice concentration (Fig. 3.24f). To make the results comparable with those by Lu08 only effective ice concentrations above 90 % were considered. We found a correlation of r = -0.66 between the scaled air temperature and the sea ice concentration and a corresponding slope of the regression line of 0.25±0.10 °C/%. A linear extrapolation of the results by Lüpkes et al. (2008b) for model run times of 12 and 48 h to an interaction time of 30 min gives a temperature increase of about 0.20 °C/%. Thus, our measurements confirm well the findings of Lüpkes et al. (2008b) about the large impact of lead ensembles on near-surface atmospheric temperatures.

3.4.2 Downward heat fluxes over ice

In the previous section we demonstrated the impact of the lead concentration on the near-surface atmospheric temperatures. Different previous studies suggest that, on a larger scale, the heat released from leads is balanced by negative fluxes over the surrounding pack ice (Overland et al., 2000; Lüpkes et al., 2008b). However, negative and thus downward heat fluxes downstream of the leads were only measured during the case study on 25 March (-5 $\mathrm{W\,m^{-2}}$), while fluxes were close to zero during the other three cases. A possible explanation is that the downward heat transport might occur at lower heights than the flight altitudes of 20 to 50 m. Also, the horizontal extent of the flight patterns downstream of the leads might have been too small.

Thus, we try to find other examples of downward heat fluxes over thick ice downstream of a region with many leads. For this purpose, we used the long flight sections on 4 and 6 March (Fig. 3.23) and identified regions with a closed, thick ice cover downstream of regions with a higher lead coverage. The considered legs were at least 18 km long and had a homogeneous thick ice cover with standard deviations of T_s smaller than 1 °C. The two regions considered for each of the two flights are marked in Fig. 3.25a and b, respectively. Turbulent sensible heat fluxes were then calculated using the meteorological measurements at about 50 m height in these regions.

The sensible heat fluxes are negative for all four considered flight sections with values of about -8 $\mathrm{W\,m^{-2}}$ (Fig. 3.25c). We can estimate the flux variability by dividing the flight sections into subsections of 6, 8, and 10 km and calculating the standard deviations of the fluxes, respectively. Depending on the chosen length of the subsections we find a variability of 1 to 5 $\mathrm{W\,m^{-2}}$. Thus, even when this variability is accounted for the observed fluxes are still always negative, which supports the assumption that at least part of the heat released from leads returns back into the ice further downstream. Thus, we conclude that leads do not only contribute to a warming of the atmosphere but can also cause a regional increase of the ice surface temperature.

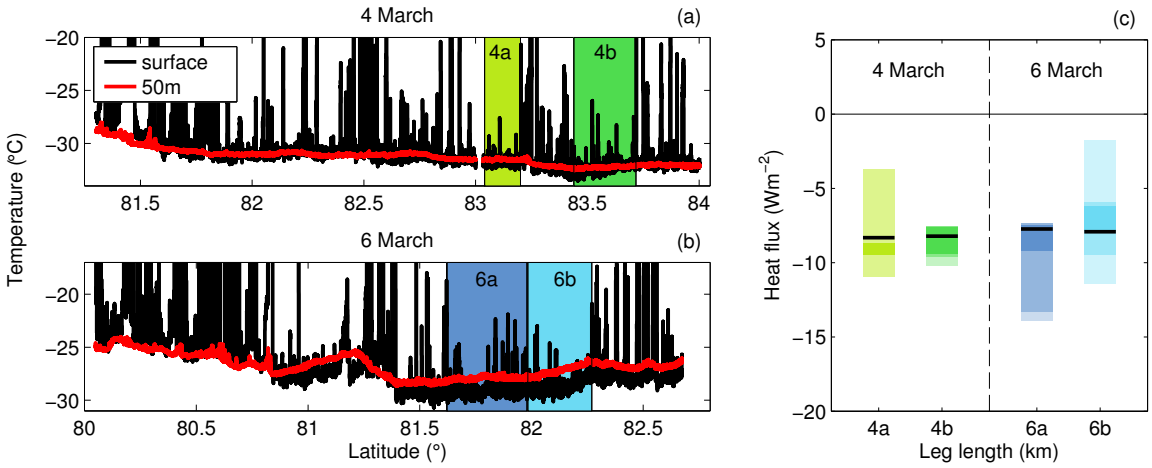

Figure 3.25: Flight sections on **(a)** 4 and **(b)** 6 March used to calculate sensible heat fluxes **(c)** over nearly lead-free ice cover. The black lines in **(c)** are the fluxes calculated over the whole marked flight sections, while the shaded areas indicate the standard deviation of fluxes when the sections are split into shorter subsections of 6, 8, and 10 km respectively.

3.4.3 General lead characteristics

This section gives an overview of the lead widths and lead surface temperatures observed during the STABLE campaign. This knowledge is not only useful for improving the sub-scale representation of leads in climate models but it can also be used to determine how often leads occur that have a similar size and ice cover as the four leads of the case studies in Sect. 3.2.

The lead characteristics are derived from long low-level flights on 4, 6, 7, 17, and 20 March (Fig. 3.23). During those flights the main lead orientation was mostly perpendicular to the flight legs and therefore the lead width can be derived from the KT-19 surface temperature data. Since all considered cases were nearly cloud-free, we can assume that surface temperature changes along the flight sections are only caused by the presence of leads. Thus, we define here a lead as a region with surface temperatures that are more than 5 K higher than the temperature of the surrounding thick ice. Due to the large integration time of the KT-19 of 1 s we only considered leads with widths larger than 100 m.

The distributions for the lead width and the surface temperature difference between the lead and the surrounding thick ice derived from all flights are shown in Fig. 3.26. About 10 % of the leads were wider than 1 km and the surface temperature difference exceeded 10 K for 25 % of the leads and 15 K for 10 % of them. Since all four leads considered in Sect. 3.2 were wider than 1.6 km with surface temperature differences ranging from about 8 to 19 K, they give a good representation of the observed variety of surface temperature conditions in March 2015 but only represent the largest observed lead widths.

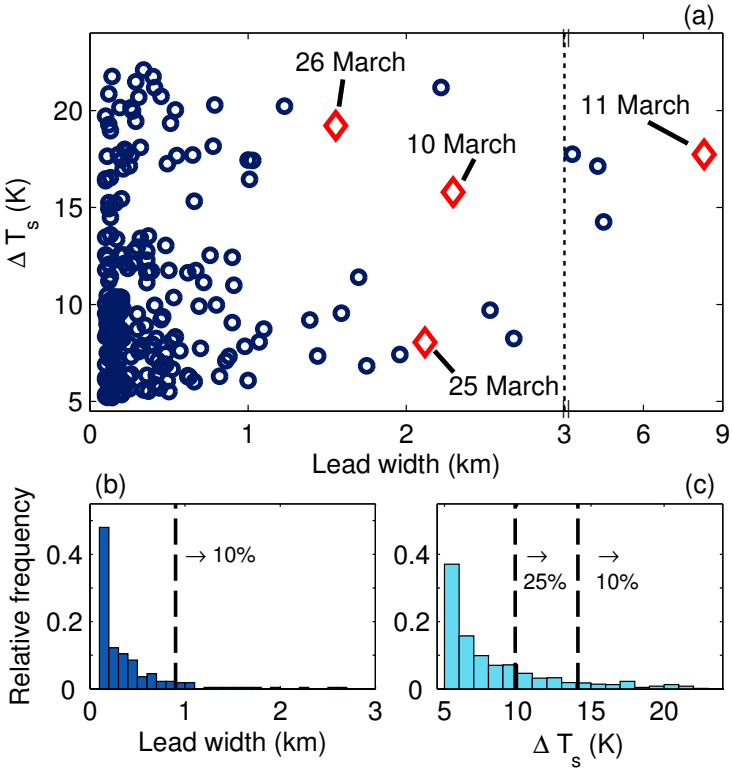

Figure 3.26: **(a)** Surface temperature difference ΔT_s between the lead and the surrounding thick ice as a function of lead width and corresponding distributions of **(b)** lead width and **(c)** surface temperature difference. Data are from the long low-level flight legs on 4, 6, 7, 17 and 20 March. The four leads of the case studies are shown as diamonds.

Various previous studies have shown that the lead width distribution follows a power law (e.g. Lindsay and Rothrock, 1995; Marcq and Weiss, 2012). Fitting a power law to our data we find an exponent of $b = 2.5$ for lead widths larger than 400 m (Fig. 3.27a). This value is in line with the results by Marcq and Weiss (2012), who found values between 2.1 and 2.6 in a visible SPOT image for lead widths between 20 m and 2 km, and by Wernecke and Kaleschke (2015), who found a value of 2.47±0.04 using CryoSat-2 data for lead widths above 600 m. However, all these results do not agree very well with the exponent $b = 1.60 \pm 0.18$ derived for scales between 1 and 50 km by Lindsay and Rothrock (1995) from aircraft-based infrared imagery during the SHEBA campaign. This discrepancy has already been discussed by Wernecke and Kaleschke (2015). Among other sensor-related reasons they considered a shift in the lead width distribution between the period from 1989 to 1995 studied by Lindsay and Rothrock (1995) and more recent years. For lead widths between 100 and 400 m, however, we find an exponent of only 1.83, which is much smaller than the results by Marcq and Weiss (2012) for these widths. Thus, in our dataset the power law is not completely scale invariant as has been discussed earlier by Lindsay and Rothrock (1995) and Marcq and Weiss (2012).

A large part of the detected leads are covered by thin ice. Since we use infrared measurements we can characterize the thin ice cover by its surface temperature. As a first guess we also assumed a power law behaviour for the surface temperature difference ΔT between the leads (T_{lead}) and the surrounding thick ice (T_i). Surprisingly, we found that the exponent is also $b = 2.5$ for temperature differences between 5 and 17 K (Fig. 3.27b) – the same value as for lead widths above 400 m. For temperature differences larger than 17 K the slope becomes much steeper with values exceeding $b = 8$. However, the temperature differences are highly dependent on the surface energy budget and thus have a large seasonal dependence. Thus, more data from all seasons are necessary to get a more robust, time-dependent estimate of the value of this exponent.

It is also necessary to account for the impact of regional and seasonal changes of the ice surface temperature, which are not related to changes of ice thickness. By considering normalized temperature differences it is possible to remove these effects from the data. We calculate the normalized temperature difference ΔT_n as

$$\Delta T_n = \frac{T_{lead} - T_i}{T_w - T_i}. \tag{3.12}$$

Here, the surface temperature difference is normalized by the maximum expected temperature difference between thick ice with temperature T_i and an open water lead with temperature T_w = -1.8 °C. The result are presented as a semi-logarithmic plot in Fig. 3.27c. In this presentation the values form a straight line for $\Delta T_n < 0.7$, which suggests that the distribution is better represented by an exponential function than by a power law fit. As for temperature differences, there is an abrupt change of the slope, which occurs at $\Delta T_n = 0.7$. This indicates that the distributions differ for leads covered by very thin ice and for leads covered by thicker ice.

It has already been demonstrated by Marcq and Weiss (2012) that a power law formulation of the lead width distribution increases the total heat flux estimates over a lead ensemble, when fetch dependent parametrisations of the heat flux are used. However, they assumed a constant surface temperature for all considered leads. Since we have shown that the temperature differences between the air and the surface are quite variable, it would be useful to also consider this variability when calculating heat fluxes. Such calculations would require a formulation relating the surface temperature differences to specific lead widths. However, much more data would be needed to derive such a joint distribution of the two parameters.

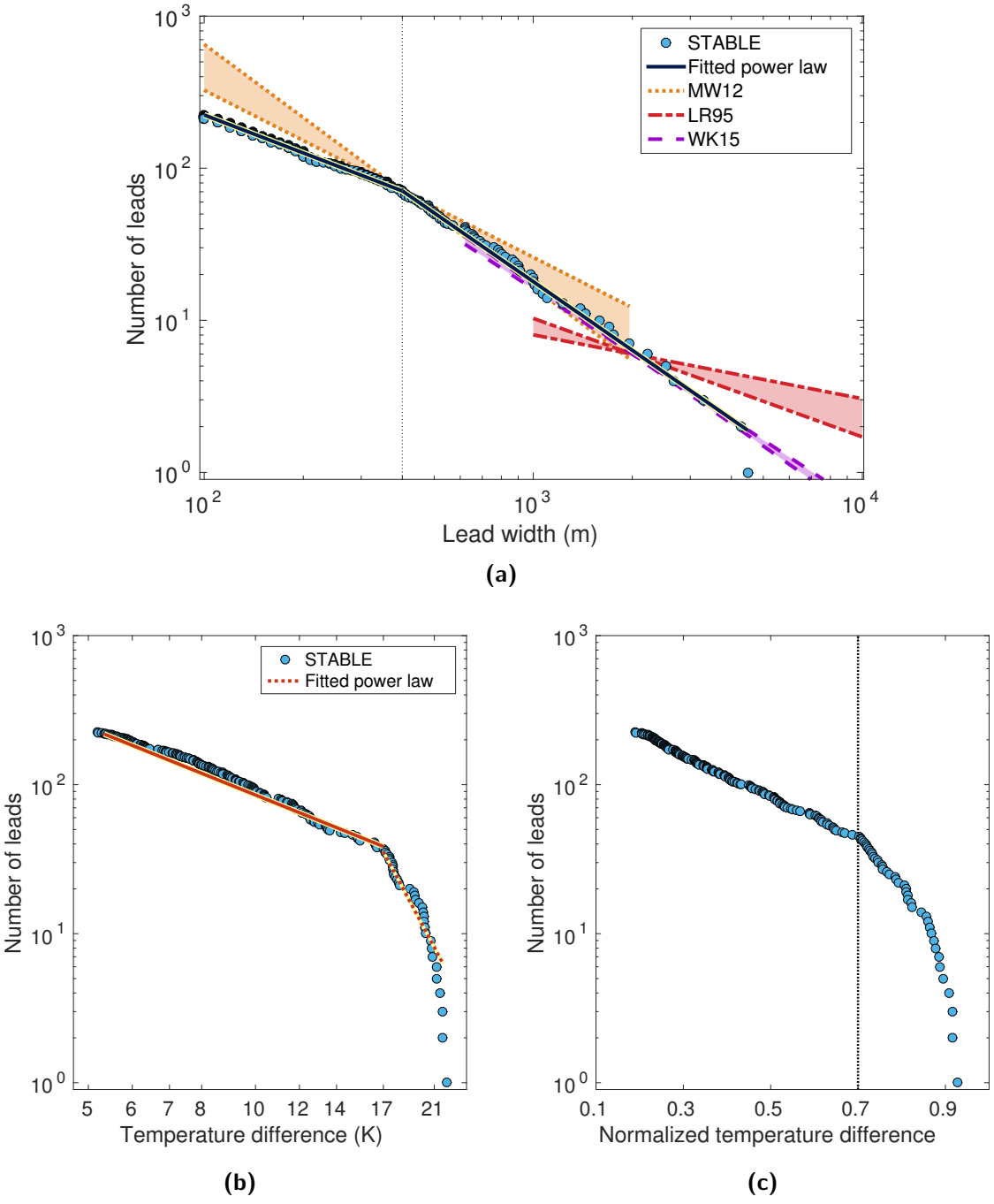

Figure 3.27: **(a)** Distribution of lead width derived from the long STABLE flight legs and corresponding power law fits. Power law distributions with exponents derived by Marcq and Weiss (2012), Lindsay and Rothrock (1995), and Wernecke and Kaleschke (2015) are shown for comparison. The shaded areas indicate the uncertainty range of the power law exponents given by the authors. **(b)** Distribution of surface temperature difference and corresponding power law fits. **(c)** Distribution of surface temperature difference normalized by the maximum possible temperature difference. The data are the same as in Fig. 3.26. Note that in **(a)** and **(b)** both axes are logarithmic, while in **(c)** only the y-axis is logarithmic.

3.5 Conclusions

Based on our four case studies we conclude that conditions over leads are strongly variable. This concerns the turbulent fluxes, as well as the mean variables wind, temperature, and humidity, which are strongly affected by the convection over leads. This is not only a consequence of modified surface fluxes but also of the interaction of the convective plumes with the inversion, which caused entrainment. The latter may play a large role for the ABL energy budget in regions with many leads since in all cases the plumes penetrated the lowest levels of the capping inversion causing entrainment fluxes of up to 30 % of the surface heat fluxes. There was clear evidence that this entrainment contributed significantly to the ABL warming downstream of the lead. This was visible by the position of the maxima of temperature and humidity, which were located at a few kilometres downstream of the lead rather than at the outflow boundary.

We found that plumes from leads have a large impact on the structure of the vertical flux profiles. The existence of these plumes explain why downstream of the leads both heat and momentum flux profiles can be non-linear with elevated flux maxima. This non-linearity of the flux profiles might lead to erroneous conclusions when surface fluxes are determined on the basis of measurements at only one level. Furthermore, our measurements showed that convective plumes over leads can be strong enough to diminish low level jets in the region influenced by the plume, which affects momentum exchange with the surface. It is obvious that such phenomena related to the convective plumes cannot be taken into account by models even when the used grid sizes are in the range of only one kilometre. However, they might be relevant also on larger scales when their effects on the ABL accumulate.

We used long transect flights to study these regional effects of leads on atmospheric temperatures and found a large correlation of r = -0.66 between the ice concentration and the near-surface atmospheric temperatures. Furthermore, for ice concentrations above 90 %, an ice concentration change of 1 % caused a temperature change of 0.25 K during the considered time periods of 30 min. This effect can sum up to large temperature changes when longer time periods are considered. These results demonstrate the importance of an accurate representation of leads in coupled climate models evaluated in polar regions. This especially holds for the Arctic, where the increased atmospheric warming rate compared to the rest of the globe has been observed in recent decades (e.g. Serreze and Barry, 2011). Even though the underlying causes are still under debate, a widely acknowledged hypothesis for this "Arctic amplification" is that the reduced sea ice cover plays an important role (Screen and Simmonds, 2010). Thus, a better understanding of the characteristics of leads and their impact on the polar atmospheric boundary is crucial for future predictions of a further warming in the Arctic.

Our measurements during STABLE are an important step in this direction. They also form a valuable dataset for validating modeling studies and parametrisations used in models. We could show the latter already for the parametrisation of the internal boundary layer height, where we pointed out the advantages and drawbacks of existing approaches. However, our analysis was based on four cases and five transect flights only and in light of the large variability of lead characteristics and possible forcing conditions, more case studies should be carried out in the future to generalize our findings of the lead impact.

4 Cold air outbreaks: observations and modeling

In the previous chapter we showed that convection over leads has a crucial impact on the ABL structure and on turbulent fluxes of heat and momentum in the inner Arctic regions. The convective plumes induced by leads influence the wind and temperature field and also modulate the atmospheric boundary layer height and its development on the downstream side of leads. In this chapter we focus on convective processes developing during cold air outbreaks (CAOs), which have a much stronger impact and influence regions often exceeding 1000 km length.

The development of temperature, humidity, wind, and turbulent fluxes in the convective boundary layer of a CAO, as well as the formation of cloud streets has been the topic of various previous aircraft campaigns and modeling studies, as already described in Sect. 1.3 in more detail. Chechin et al. (2013) found that the conditions in the upstream region - that is the region some 300 km on the upstream side of the ice edge - are important for the CAO development. However, despite the relatively large number of airborne observations of CAOs in the Fram Strait region, most available measurements did not include the conditions far north of the ice edge since the range of the used aircraft was not large enough. The modeling results by Chechin et al. (2013) also suggest that the strength of the ice-breeze jet – a wind speed maximum at a distance of 50 to 150 km downstream of the ice edge – depends strongly on the direction of the large scale geostrophic wind speed relative to the ice edge. Thus, it would be helpful to acquire more measurements for different orientations of ice edge.

Such data were obtained during the campaign STABLE, in March 2013, when the ice edge in the Fram Strait region was oriented from south-west to north-east. This was exceptional because the ice edge was usually oriented from west to east in the previous decades. To capture also the upstream conditions during CAOs, aircraft measurements far north of the ice edge were combined with dropsonde measurements over the open ocean. These measurements are presented in the following sections. Since the dropsondes measure with a lower resolution and a simpler instrumentation than the aircraft, it is useful to validate the quality of the dropsonde data against the aircraft measurements (Sect. 4.1), before the results obtained during CAOs are presented in Sect. 4.2. We analyse the downstream development of meteorological variables and the growth of the internal convective boundary layer during four CAOs. In addition, we assess the impact of the size of the Whaler's Bay polynya north of Svalbard on the strength of CAOs and on local temperature changes. Parts of this section are based on Tetzlaff et al. (2014).

Our measurements will be useful for future validation of modeling studies, however, this validation was not in the scope of the present thesis. Here, we only focus on a small side aspect of this topic concerning the parametrisation of turbulent sensible heat fluxes in the convective ABL within CAOs. In Sect. 4.3 we evaluate the performance of three different parametrisations in a 1D version of the mesoscale model METRAS. These include, amongst others, a newly implemented combined eddy-diffusivity mass-flux scheme. The METRAS results are compared to results obtained from large eddy simulation for verification. In addition, we test the sensitivity

of the three parametrisations to an increased vertical grid spacing.

4.1 Validation of dropsonde data against aircraft measurements

4.1.1 20 March 2013

On 20 March 2013 a dropsonde was launched at the northernmost point of the transect flight (see overview Fig. 1.4 in Chapter 1) in between an ascent and a descent of the Polar 5 aircraft (Fig. 4.1a). The aircraft profile obtained during the ascent extended from about 40 m to 2900 m while the profile of the descent ended at 500 m, which was the height of the subsequent southward horizontal flight section. The profile positions were located about 280 km north of the ice edge in a region with mostly closed ice cover with only few leads and AMSR2-ASI ice concentrations above 98 %. The prevailing winds were from south, so that the considered case represents an on-ice flow regime. The sky was mostly cloud free with only thin cirrus at high altitudes. The two aircraft profiles had a spatial distance of about 1.9 km with a standard deviation of 0.6 km and the time lag was 2 minutes at the profile top and 25 minutes at the surface. The distances between aircraft and dropsonde profiles were much larger and increased from about 10 km at 2500 m to almost 50 km close to the sea surface (Fig. 4.1b).

The dropsondes (Vaisala RD93) measure temperature, pressure, relative humidity (measured with a humicap), as well as GPS coordinates and height with a temporal resolution of 2 Hz (Lampert et al., 2012) for temperature, humidity, and pressure. Wind speed and direction are estimated from the drift of the sonde, which is less accurate than the aircraft wind vectors derived from direct measurements of dynamical pressure. The dropsonde fall speed is about 10 $m s^{-1}$ resulting in a vertical resolution of the dropsonde data of about 4 to 6 m. Since the aircraft measures with up to 100 Hz, the aircraft data are interpolated to the corresponding dropsonde heights for the comparison.

The dropsondes deliver heights derived from GPS. However, the GPS height is not a good reference for the absolute height due to uncertainties caused by changing satellite availability, ionospheric effects, and deviations of the real geoid from the reference geoid. These deviations

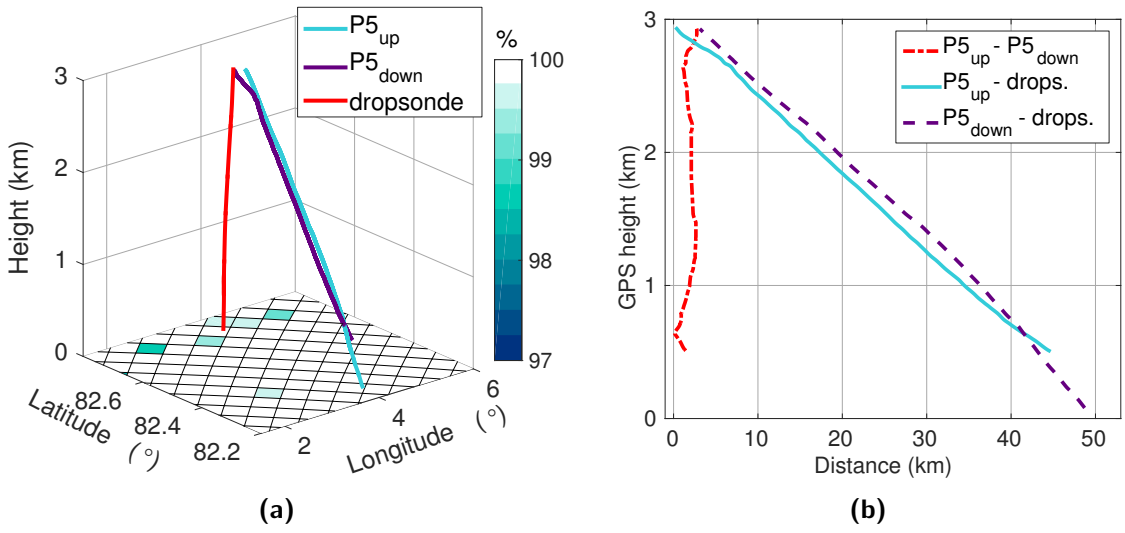

Figure 4.1: **(a)** Comparison of aircraft profile and dropsonde positions and **(b)** corresponding horizontal distances between the profiles. The surface shading in **(a)** is the corresponding AMSR2-ASI ice concentration.

from the real height above sea level can change with region and time. For the dropsonde on 20 March, for example, the GPS height overestimates the real height by about 25 m. This value can change with region and considered time, however. Thus, here and in the following sections, we estimate the "real" height from the barometric height, which is calculated by combining the hydrostatic equation with the ideal gas law for dry air, which results in:

$$\frac{\partial p}{\partial z} = -\frac{gp}{R_d T}. \tag{4.1}$$

Here, p is the pressure, z is the height, $g = 9.81\,\mathrm{ms}^{-2}$ is the acceleration due to gravity, $R_d = 287.1\,\mathrm{Jkg}^{-1}\mathrm{K}^{-1}$ is the specific gas constant for air, and T is the air temperature. After integrating over z we obtain

$$z_2 = z_1 + \frac{R_d \cdot \overline{T}}{g} \ln\left(\frac{p_1}{p_2}\right), \tag{4.2}$$

where z_1 and z_2 are two neighboring z-levels with measured data and $\overline{T}$ is the average temperature at z_1 and z_2. Equation 4.2 is evaluated stepwise starting at the surface and using the dropsonde measurements of pressure and temperature. The sea level ($z = 0$) is determined from the dropsonde's last measurement at the point where the measured GPS heights do not significantly change any more. For the aircraft measurements the most accurate height is measured with the laser altimeter. Thus, when data from the laser altimeter are available we use those heights to correct the uncertainties of the GPS heights.

A comparison of the dropsonde and aircraft profiles of temperature, relative humidity, wind speed, and wind direction is presented in Fig. 4.2. The overall agreement between the measurements is quite well, however, there are differences in the quality of agreement depending on the parameter. The best agreement is for temperature and, remarkably, for the wind direction, while the worst agreement is for relative humidity.

According to the figure the largest differences for all parameters occur when extrema, such as temperature inversions and layers with increased relative humidity values, are measured by both sensors but do not occur at the exactly same height. These differences are not necessarily caused by sensor problems but are probably due to the large horizontal distance between the profiles. The differences, which are discussed in more detail in the following, can thus be attributed to horizontal inhomogeneities.

For the calculation of mean differences we focus on the sensor related differences only. Thus, we restrict the calculations to a height interval where the influence of horizontal inhomogeneities is small. As can be seen from Fig. 4.2, these inhomogeneities have a large influence on the heights of the temperature inversion and the turning point of the wind direction below 800 m. They also influence the heights of the layer with increased relative humidity values above 2000 m. To exclude these regions, we only consider values between 800 and 2000 m for the following sensor comparison. The resulting mean differences and standard deviations are given in Table 4.1. Due to the small spatial and temporal differences of the two aircraft profiles the observed differences of the measured variables were also very small (see Table 4.1). Thus, we focus mainly on the comparison of dropsonde and aircraft profiles in the following.

The temperature of both measurements (Fig. 4.2a) show similar strengths and positions of the two temperature inversions near the surface and at about 600 m. But there are also differences. For example, between 800 and 2000 m the dropsonde shows a warm bias of 0.38 °C, which is about twice the value of the sensor accuracy. Due to the lower temporal resolution of the dropsonde the temperature profile in the layer between 800 and 1600 m is smoother than the aircraft profiles.

A more detailed comparison of the potential temperature profiles in the lowest 500 m (Fig. 4.3a) shows also some differences. While the height of the inversion top at about 100 to 120 m agrees

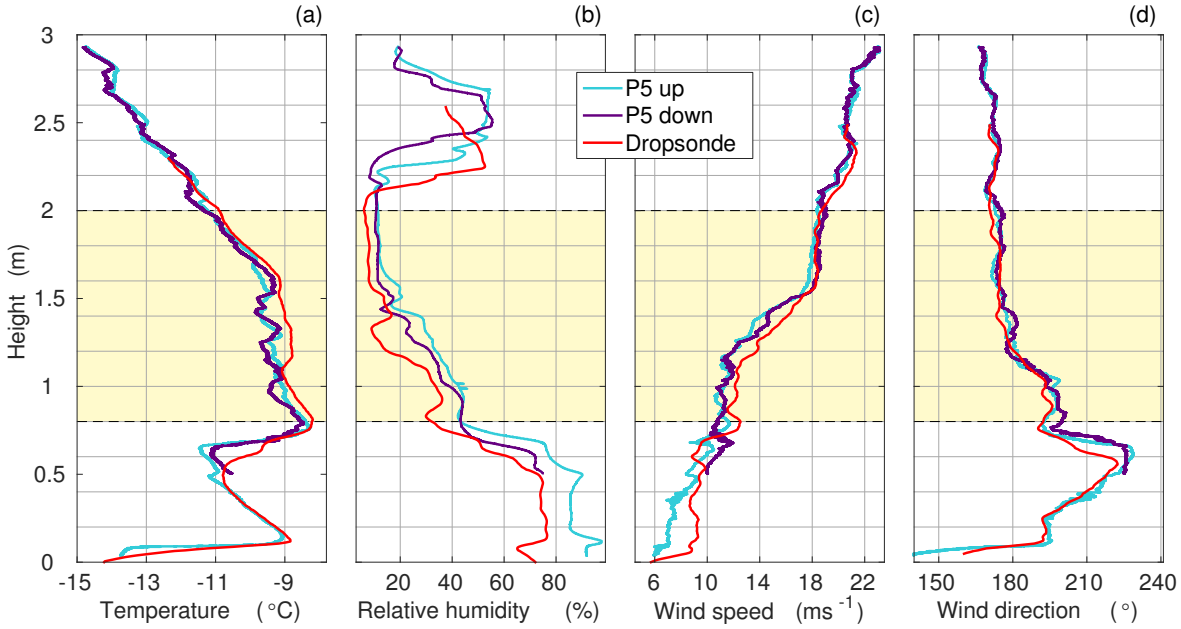

Figure 4.2: Vertical profiles of **(a)** temperature, **(b)** relative humidity, **(c)** wind speed, and **(d)** wind direction from up- and downward aircraft profiles and the corresponding dropsonde on 20 March 2013. The shaded area denotes the values used for the calculation of differences in Table 4.1.

well for aircraft and dropsonde profiles, there are substantial differences in the lowest 100 m. The potential temperature profile of the dropsonde shows a surface-based inversion of nearly constant strenght, while the aircraft profile shows a weaker stably stratified layer below 80 m with a strong capping inversion layer above. However, this does not point to instrumental problems. Since the profiles are almost 50 km apart near the surface, these differences can be attributed to local differences of the surface conditions, for example the presence of leads, which influence the boundary layer height and stratification.

The largest differences between aircraft and dropsonde occur for relative humidity. Below 2000 m the dropsonde humidities are always lower than those measured by the aircraft (Fig. 4.2b).

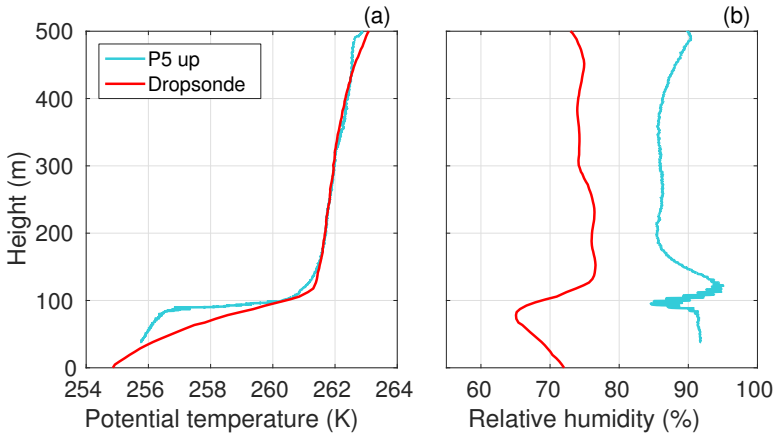

Figure 4.3: Vertical profiles of **(a)** potential temperature and **(b)** relative humidity from the upward aircraft profile and the corresponding dropsonde on 20 March 2013.

Table 4.1: Mean differences and standard deviations between the upward and downward aircraft profiles ($P5_{up}$ - $P5_{down}$) and between the aircraft profiles and the dropsonde (P5 - dropsonde) at GPS heights between 800 and 2000 m.

Variable	Unit	Accuracy[a]	$P5_{up}$ - $P5_{down}$	P5 - dropsonde
Temperature	°C	0.2	0.06 ± 0.19	-0.38 ± 0.19
Relative humidity	%	2	3 ± 2	8 ± 5
Wind speed	ms	0.5	-0.3 ± 0.3	-0.7 ± 0.7
Wind direction	°	N/A	-1 ± 2	2 ± 3
Pressure	hPa	0.4	0.04 ± 0.02	-7.4 ± 0.2

[a]approximate values for the dropsondes given by the manufacturer, from Lampert et al. (2012)

The relative humidity measured by the dropsonde in the layer between 800 and 2000 m is 7 % lower than the aircraft values, corresponding to a difference of the specific humdity of about 0.15 g kg^{-1} (not shown). These results are in line with the findings by Vance et al. (2004) who reported a dry bias of humidity measurements by this dropsonde type compared to aircraft and radiosonde data. The bias is even more pronounced below 500 m (Fig. 4.3b) with differences exceeding 10 %. In addition, it is evident from the aircraft measurements that the humicap does not respond fast enough to rapid humidity fluctuations, which causes an oscillating behavior of the measured values.

The profiles of wind speed and direction show a very good agreement between the dropsonde and aircraft measurements. The wind speed measured by the dropsonde between 800 and 2000 m is about 0.7 m s^{-1} larger than the wind speed of the aircraft profiles (Fig. 4.2c), which is in the order of the measurement accuracy for GPS derived wind speeds. Below 400 m the dropsonde wind speed is about 2 m s^{-1} larger than the aircraft derived wind speed, which can be again attributed to local differences of the boundary layer structure. The wind direction differences between all three profiles are impressively small with only 2° on average (Fig. 4.2d).

4.1.2 26 March 2013

We also consider the differences between two dropsonde profiles at the same position but with a time lag of 2 h. The two dropsondes were launched on 26 March 2013 over the sea ice close to the pack ice edge northeast of Svalbard (at 81.173° N, 19.93° E). They were the first in a series of dropsondes launched to study the cold air outbreak north and east of Svalbard during that day with prevailing off-ice flow from the northeast (see location of the north-easternmost sonde in Fig. 4.5d). The profiles were located about 50 km northeast of the ice edge in a region with varying ice concentration between 50 and 100 %. Convection related to the cold air outbreak had already started in this region and low level convective clouds were present.

The launch times were 11:54 UTC for sonde 1 and 14:13 UTC for sonde 2, resulting in a time difference of about 2.3 hours. The second sonde was located slightly further to the northwest, but the mean spatial distance between the sondes was only about 100 m with maximum values of about 170 m near the ground. Since the spatial differences are so small and the analysis in Sect. 4.1.1 showed that the sondes work well, a large part of the observed differences between the two sondes can be attributed to temporal changes.

A comparison of the profiles in Fig. 4.4 shows that the differences are largest for relative humidity and wind speed, while they are smaller for potential temperature and wind direction.

The potential temperature profile shows only very small differences above the top of the capping inversion whose base remains nearly unchanged within the 2 hours. There are changes only below 100 m, where sonde 1 shows a weakly stable ABL with a potential temperature gradient of about 0.006 Km^{-1} below the inversion, while the ABL of the sonde 2 is nearly well mixed with a gradient of 0.001 Km^{-1}. Sonde 1 has a thicker capping inversion extending upward to about 500 m while sonde 2 has a stronger but shallower inversion layer extending only to about 320 m.

The relative humidity profiles of the two sondes below 700 m agree quite well within 5 % (Fig. 4.4b), while differences are much larger above this height. These differences could be related to the presence of cloud layers of different thicknesses, whose presence cannot be measured directly by the dropsonde. However, it is likely that clouds are present in layer where the air is saturated with water vapor. In the following, we describe the method used to determine these saturated layers. The relative humidity value given by the humicap is based on the saturation humidity with respect to water. For temperatures below freezing, however, ice clouds are often present and thus saturation with respect to ice is more applicable. One way to calculate the different saturation water vapor pressure values over water $e_{s,w}$ and over ice $e_{s,i}$ is the empirical formula

$$e_s(T) = 6.112\,\text{hPa} \cdot \exp\left(\frac{a \cdot T}{b + T}\right), \tag{4.3}$$

with the constants $a_w = 17.62$ and $b_w = 243.12\,°C$ for water, and $a_i = 22.46$ and $b_i = 272.62\,°C$ for ice (WMO CIMO Guide, 2008). T is the air temperature in °C. Since the relative humidity is $RH_w = 100 \cdot e(T)/e_{s,w}(T)$ over water and $RH_i = 100 \cdot e(T)/e_{s,i}(T)$ over ice, the ratio $e_{s,i}/e_{s,w} \cdot 100$ is then the relative humidity value with respect to water at which saturation with respect to ice occurs. These values are indicated by the shaded area in Fig. 4.4b. It is evident that the saturated layer - which is probably identical to the cloud layer in this case - for sonde 1, extending from about 500 to 1300 m, is much thicker than for sonde 2, extending only from about 400 to 800 m, which demonstrates the large temporal variability of the cloud layer in this case.

The gusty nature of the wind speed is clearly visible in Fig. 4.4c. Besides these local gusts, the wind speed below 700 m decreased by about 1 ms^{-1} between sondes 1 and 2, while it increased by about 1 ms^{-1} above 700 m. Between the two sondes the wind vector turned clockwise by about

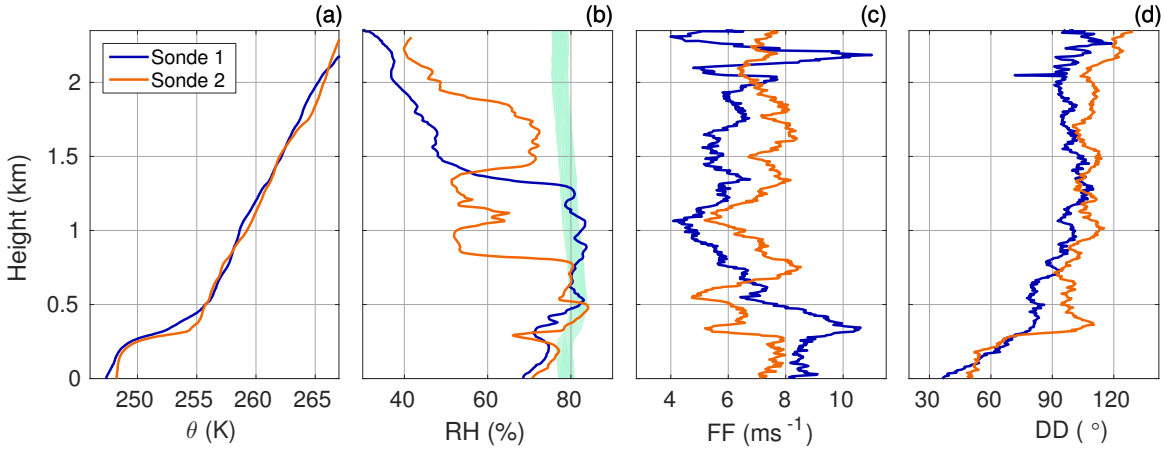

Figure 4.4: **(a)** Potential temperature, **(b)** relative humidity, **(c)** wind speed, and **(d)** wind direction from dropsondes 1 and 2 on 26 March 2013 at 11:54 and 14:30 UTC, respectively. The green shaded area in **(b)** denotes the relative humidity value with respect to water at which ice saturation is achieved. The width of the shaded area is ±2 % to account for the measurement uncertainty of the humicap (see Table 4.1).

10 to 20° towards the south above the mixed layer (Fig. 4.4d) and also in the lowest 50 m of the ABL. This turning of the wind vector might also explain the changed ABL stratification, if the incoming flow had passed over areas with different ice concentrations, due to the presence of a lead for example.

4.1.3 Summary

Our validation of dropsonde data against aircraft measurements showed a generally good quality of the dropsonde measurements. Especially the GPS derived wind vectors compare very well with the direct aircraft measurements. Shortcomings are the dry bias in the humidity measurements and the reduced captured temperature variability due to the low measurement frequency. Nevertheless, dropsondes are a very valuable way to save flight time compared to more time-consuming profile flight legs of the aircraft. Dropsondes also enable measurements in cloudy or foggy conditions, when direct aircraft measurements are difficult. Dropsonde profiles are also advantageous when measurements are compared to model results. In contrast to the tilted profiles derived from ascent and descent flights of the aircraft dropsonde profiles are nearly vertical and thus represent the local stratification of the air column. An additional comparison of two successive dropsondes at the same location revealed that the overall changes of the measured profiles are quite small over the considered time period of 2.5 h. The largest differences occur for the extent of cloud layers and the ABL stratification.

4.2 Case studies of cold air outbreaks observed during STABLE

4.2.1 Overview

Cold air outbreaks were observed during four of the flights during STABLE, namely on 4, 6, 7, and 26 March 2013. An overview of the four cases is given in Fig. 4.5. During the four cases northerly or northeasterly winds prevailed over the ocean in the northern Fram Strait and in the ice free region north of Svalbard, commonly referred to as the Whaler's Bay polynya. The wind direction was more variable over the sea ice in the upstream regions of the CAOs with directions ranging from northwest (6 March) to northeast (26 March). The cold air flow off

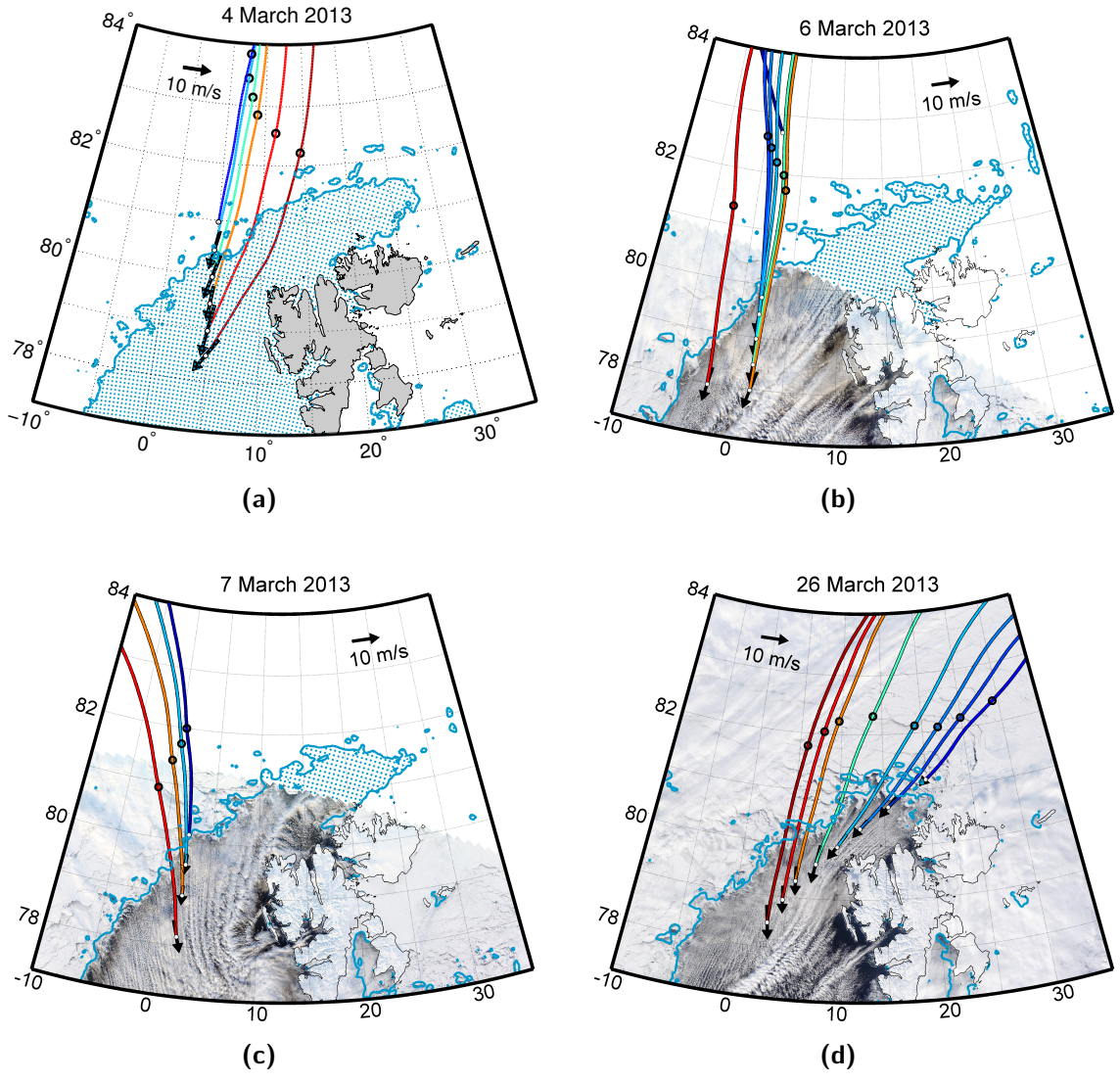

Figure 4.5: Ice edge based on a 70 % threshold value of the AMSR2-ASI ice concentration during days with cold air outbreaks: **(a)** 4 March, **(b)** 6 March, **(c)** 7 March, and **(d)** 26 March 2013. The arrows denote the vertically averaged wind in the boundary layer at the positions of the dropsondes. The lines are HYSPLIT backward-trajectories at 10 m height and the dots mark 10 h. Backgrounds of **(b)**-**(d)**: corresponding MODIS visible images at 13:10 UTC, 12:15 UTC, and 12:45 UTC, respectively (data from http://lance-modis.eosdis.nasa.gov/cgi-bin/imagery/realtime.cgi).

the ice caused strong convection over the ocean associated with convective rolls that are clearly visible as cloud streets in satellite images (Fig. 4.5). To study the downstream development of mean meteorological variables, dropsondes were released over the open water region. On 4, 6, and 7 March these measurements were supplemented by aircraft profiles over the ice covered area further to the north. An overview of the profile locations of the four cases is given in Fig. 4.5.

Backward-trajectories initialized at the profile positions are used to visualize the corresponding flow field. They are calculated for a height of 10 m using the HYSPLIT (HYbrid Single-Particle Lagrangian Integrated Trajectory) transport and dispersion model by NOAA (Draxler and Rolph, 2013). The trajectories are also used to obtain a rough estimate of the length of the path over open water of the air parcels (fetch) corresponding to the measured profiles. It is clearly visible in Fig. 4.5 that in all four cases the backward trajectories agree well with the measured wind vectors averaged over the ABL (arrows) and with the roll orientations observed in the satellite images. Thus, the front conclusion that can be drawn from these cases is that even in this complex situation with strong convection and thus strong small scale motions HYSPLIT is a reliable tool for trajectory estimation.

The good agreement between the wind vectors and the roll orientation is also remarkable because on 7 and 26 March the satellite image was taken up to 3.5 h after the measurements took place. This indicates that the rolls remained stationary over this period, which is consistent with the nearly constant large scale flow fields in the considered regions (according the the surface pressure fields of the GFS analysis at 6, 12, and 18 UTC).

4.2.2 Downstream development of mean meteorological variables and ABL growth

4 March

The CAO on 4 March 2013 was caused by a strong high pressure system over Greenland and a low pressure channel expanding over the Barents and Kara Seas. Vertical profiles of wind, temperature, and humidity were obtained from five dropsondes released along 5° E in distances of 0.5° latitude, supplemented by aircraft profiles at four positions as far as 400 km north of the ice edge (Fig. 4.5a). We found the typical vertical temperature structure of a convective case with a well mixed layer between the surface and a strong capping inversion together with an increasing temperature and atmospheric boundary layer height with distance from the ice edge (Fig. 4.6a). This documents the convective character of the ABL as found earlier by several campaigns measuring Fram Strait CAOs (Brümmer, 1997; Hartmann et al., 1997; Chechin et al., 2013; Lüpkes and Schlünzen, 1996; Wacker et al., 2005).

Over the sea ice north of the ice edge we observed a shallow atmospheric boundary layer of about 200 m thickness. The potential temperature gradients within the ABL indicate a strongly stable stratification at 400 km north of the ice edge that changed to a nearly neutral stratification downstream of about 300 km until the ice edge was reached (Fig. 4.7a). The near-surface temperature increased already over the pack ice region by about 4 K between 400 km and 64 km north of the ice edge (Fig. 4.6a). As already shown in Sect. 3.4.1 this temperature increase is related to leads within the pack ice. Over the ocean the observed temperature increase was much larger. The vertically averaged ABL potential temperature increased from 243 K at 64 km north of the ice edge by 18 K at 214 km south of it. Simultaneously, the boundary layer height increased from 150 m to about 2500 m.

The ocean is also an important humidity source, which can be seen from the increase of the specific humidity at 100 m height from 0.3 $g\,kg^{-1}$ near the ice edge to more than 1.2 $g\,kg^{-1}$ downstream of 150 km south of the ice edge (Fig. 4.7b). The impact of the cold air outbreak is also visible in the wind speed. This CAO on 4 March is characterized by strong winds of 13 $m\,s^{-1}$ averaged over the ABL already over the ice (Fig. 4.7c). With decreasing surface roughness over

the ocean the wind speed increases to about 16 ms^{-1}. A further increase to more than 20 ms^{-1} could be observed downstream of 150 km.

The observed increases in potential temperature and specific humidity are in the range of previous observations in the literature. The most comprehensive data set of aircraft measurements in the convective ABL of CAOs is from Brümmer (1997) who measured the downstream development of meteorological variables in eight CAOs in the Fram Strait during the aircraft

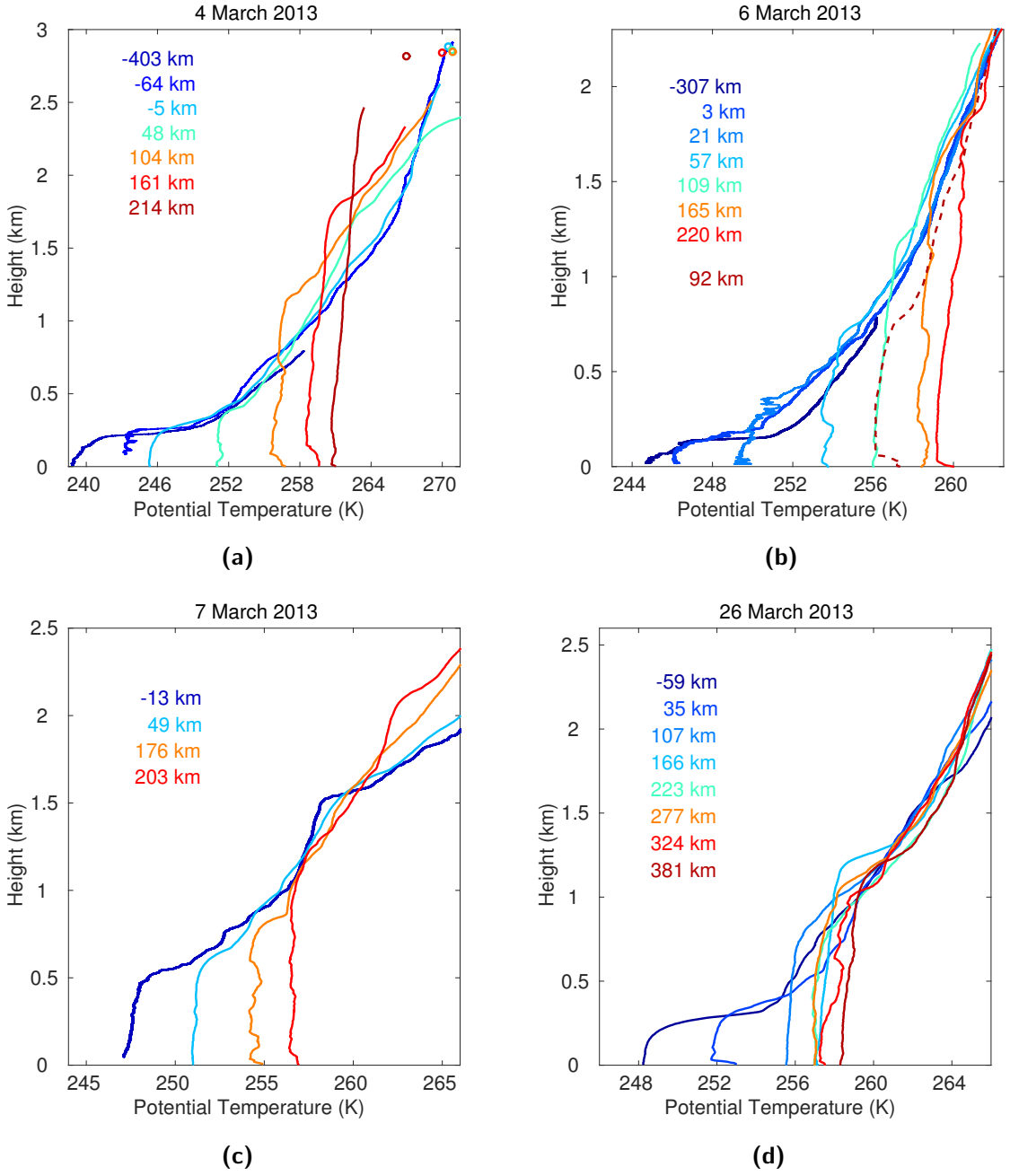

Figure 4.6: Potential temperature profiles from aircraft and dropsonde data as a function of distance from the ice edge along the flight path on **(a)** 4 March,**(b)** 6 March,**(c)** 7 March, and **(d)** 26 March 2013. The dots in **(a)** are aircraft measurements at the dropsonde release points. The dashed line in **(b)** marks the westernmost dropsonde located at about 2° W.

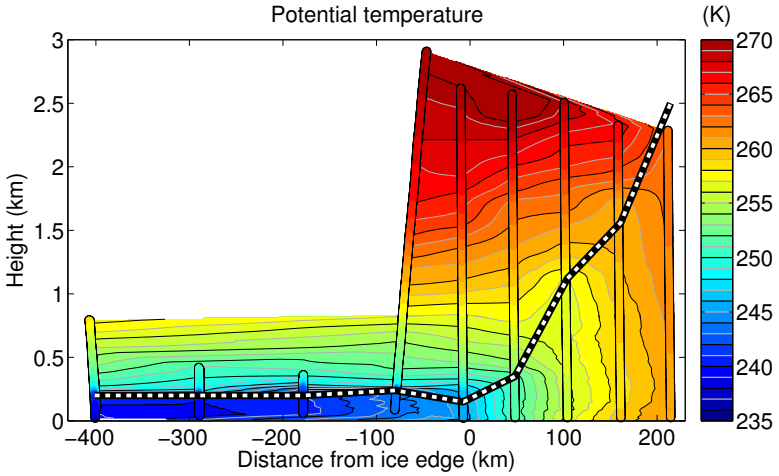

(a)

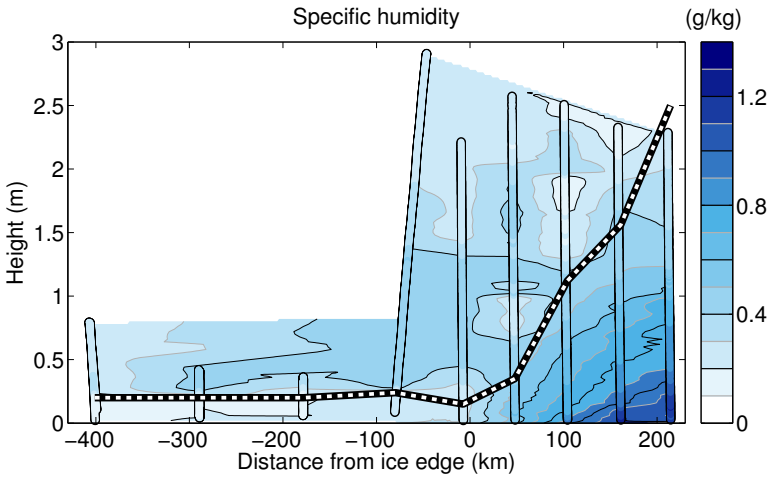

(b)

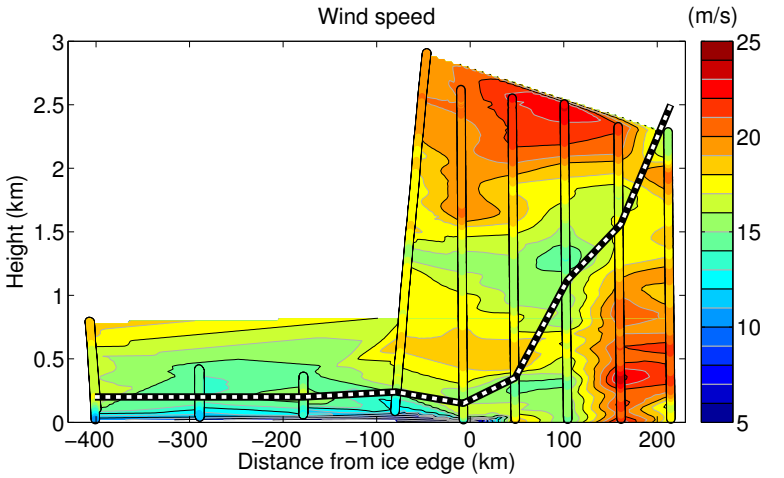

(c)

Figure 4.7: Vertical cross-sections of **(a)** potential temperature, **(b)** specific humidity, and **(c)** wind speed on 4 March 2013 derived from dropsonde and aircraft data. The dashed line indicated the atmospheric boundary layer height. The distance from the ice edge is calculated along the 5° E meridian.

campaign ARKTIS '93 in March 1993. In three of those cases the increase of the vertically averaged ABL potential temperature exceeded 17 K and 0.9 g kg^{-1} for the averaged specific humidity over a distance of 200 km over the open ocean downstream of the ice edge. In one of these cases the averaged ABL wind speed also exceeded 20 m s^{-1}.

However, the observed maximum ABL height of 2500 m is larger than any value published in the literature for this northern position (e.g. Brümmer, 1997). Since we did not observe much stronger winds or much lower air temperatures than in this study, another possible reason for the extreme ABL height at this latitude can be found by considering the open water fetch. A rough estimate of the latter can be derived from the HYSPLIT backward trajectories. For the southernmost dropsonde the fetch of 350 km was much larger than just the north-south distance to the ice edge of only 214 km. In this case the fetch is strongly increased due to north-easterly winds in contrast to the most frequent north-south orientation of CAOs, which explains the unusually large ABL height in this region. Comparing our measurements to the ARKTIS '93 results (Fig. 4.8) - a year when the Whaler's Bay polynya north of Svalbard was nearly closed - we find that our boundary layer height of 2500 m on 4 March, located at 78.5° N, was larger than in all observed cases during ARKTIS '93. The largest boundary layer height observed by Brümmer (1997) was only about 2100 m at 77.5° N, which is 100 km further to the south.

The much longer fetch compared to the north-south distance from the ice edge makes it also difficult to draw conclusions about entrainment in this case. Considering only Fig. 4.6a one might conclude that the profiles at 104, 161, and 242 km indicate strong entrainment since the ABL is rapidly growing to values which are higher than the intersection point between the considered and the previous profile. However, this growth might also be due to the different fetch lengths over open water. Problems arise especially for the two southernmost dropsonde profiles, where the fetch was about 50 and 150 km larger than the distance to the ice edge parallel to the flight section, respectively. This example demonstrates that conclusions on the role of entrainment that are based on measured profiles only have to be considered with caution when horizontal inhomogeneities are present. This aspect has not been mentioned yet in previous studies.

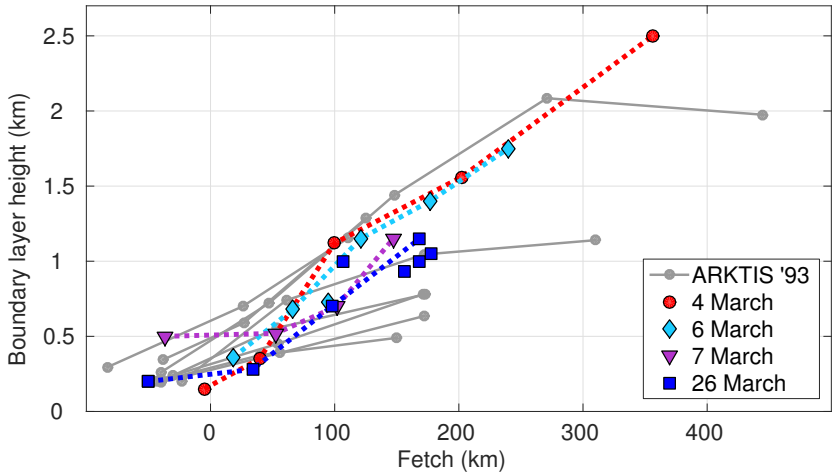

Figure 4.8: Boundary layer height on 4, 6, 7, and 26 March as a function of open water fetch and data from ARKTIS'93 (Brümmer, 1997) for comparison (gray).

6 March

The synoptic situation on 6 March was very similar to the one on 4 March, with comparable high wind speeds of 11 to 13 $m\,s^{-1}$ at 100 m height over the sea ice. Profiles were obtained from 4 dropsondes released along 2° E over the ocean and four aircraft profiles ranging up to 300 km upstream over the sea ice. The difference to the CAO on 4 March can be seen from the backward trajectories (Fig. 4.5b). Here, we find a classical case of CAOs observed earlier in the Fram Strait region where the trajectories only show a north-southward orientation and are parallel to each other. This means that at any position the distance over open water to the ice edge along the flight path is equivalent to the open water fetch.

For this reason, despite the similar wind speed, upstream ABL height, and inversion strength, the increase of the potential temperature over the ocean is much smaller than on 4 March, with only about 13 K over a distance of 220 km (Fig. 4.6b) compared to 18 K on 4 March. We also found a smaller maximum ABL height of only 1800 m at a position 220 km downstream of the ice edge. However, if the fetch is considered instead of the distance to the ice edge we find a large agreement of the ABL growth with respect to fetch (Fig. 4.8).

The comparison of the downstream evolution of wind speed and specific humidity between 4 and 6 March is also not inconsistent with the smaller fetch lengths on 6 March (Fig. 4.9). The average ABL wind speed increased from 11 $m\,s^{-1}$ at a position 300 km north of the ice edge to

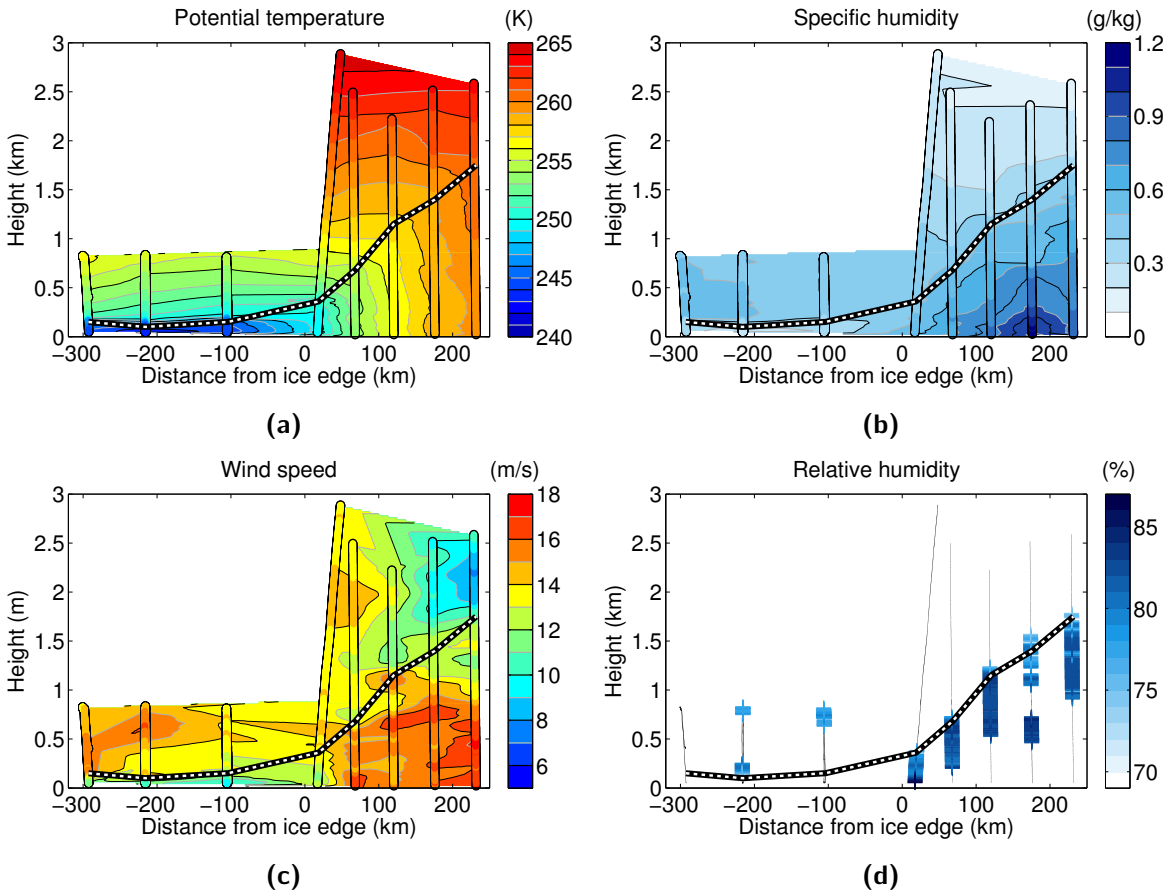

Figure 4.9: Vertical cross-sections of **(a)** potential temperature, **(b)** specific humidity, **(c)** wind speed, and **(d)** relative humidity in saturated areas on 6 March 2013 derived from dropsonde and aircraft data. The dashed line indicated the atmospheric boundary layer height. The distance from the ice edge is calculated along the 2° E meridian.

a maximum of about 17 $m\,s^{-1}$ downstream of 150 km (Fig. 4.9c), while the observed maximum wind speed on 4 March was more than 20 $m\,s^{-1}$. The specific humidity at 100 m height increased from about 0.3 $g\,kg^{-1}$ over the ice to only 0.9 $g\,kg^{-1}$ at 220 km downstream of the ice edge (Fig. 4.9b). However, we observed a local humidity maximum at 165 km with values around 1.1 g kg^{-1} below 150 m.

An indication for the presence of cloud layers can be received by considering the saturation relative humidity with respect to an ice surface (see Sect. 4.1.2). Over the ocean it is reasonable to assume that within the ABL enough condensation nuclei are present to allow for cloud formation when the air is saturated. Thus, the relative humidity values downstream of the ice edge which are shown in Fig. 4.9d represent the extent of the layer in which clouds could possibly be present. Such a cloud layer is present in all profiles downstream of the ice edge. The cloud top is always near the inversion base and the height of the cloud base increases rapidly with distance. The cloud thickness is about 400 m near the ice edge and increases to a maximum of 800 m at 200 km distance. In one case a second cloud layer exists in the center of the ABL. In the other three CAO cases many sondes did not indicate a cloud layer, which might be either due to the dry bias of the dropsondes or because the sondes were dropped in the cloud-free regions between the rolls. Therefore those results are not presented in this analysis.

An additional dropsonde was launched at approximately 78° N, 2° W, which is already close to the marginal sea ice zone along the eastern coast of Greenland. Even though this sonde was located at the same latitude as the last dropsonde launched at the 2° E flight leg (see Fig.4.5) the potential temperature profiles of these two sondes show large differences with respect to mean ABL temperature and ABL height (see lines for 92 and 220 km in Fig. 4.6b). This can again be attributed to the different fetch lengths caused by the northeast-southweast orientation of the ice edge. The additional dropsonde has only a fetch of 92 km and therefore the mean ABL temperature agrees much better with the sonde with a distance of 109 km to the ice edge launched at the 2° E flight leg. However, the ABL heights between these two sondes still differ substantially.

7 March

On 7 March the backward trajectories show northerly winds over the sea ice with an increasing westerly component over the ocean towards the south (Fig. 4.5c). This results in slightly smaller fetch lengths over open water compared to the distance between the dropsonde position and the point where the aircraft crossed the ice edge. Vertical profiles from aircraft and three dropsondes are located along the 2.5° E meridian, starting 13 km north of the ice edge and extending to 203 km south of it. The observed wind speeds within the ABL are slightly smaller than in the previous two cases. They increase from about 6 $m\,s^{-1}$ at 100 m height over the ice to 13 $m\,s^{-1}$ at 203 km downstream of the ice edge (Fig. 4.10c). The increase of the specific humidity with 0.5 $g\,kg^{-1}$ over a distance of roughly 200 km is also slightly smaller than in the previous two cases (Fig. 4.10b).

The initial ABL height of about 500 m over the ice is larger than for the other three considered cases. There was only a very small increase of less than 30 m of the ABL height until 49 km south of the ice edge. However, the potential temperature increased by 3.5 K between these two profiles (Fig. 4.6c). This process, where no entrainment of air from within the inversion layer into the ABL is present and thus the ABL growth does not exceed the inversion above, is called encroachment. The encroachment process continues for the other two profiles, resulting in a maximum ABL height of 1150 m at a distance of 203 km south of the ice edge and and overall temperature increase of 9 K over a distance of roughly 200 km.

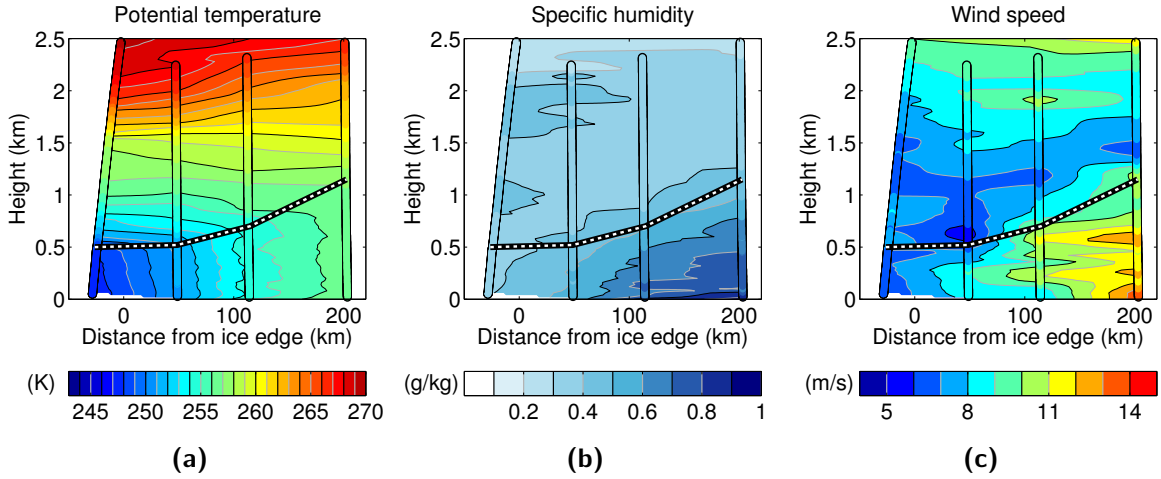

Figure 4.10: Vertical cross-sections of **(a)** potential temperature, **(b)** specific humidity, and **(c)** wind speed on 7 March 2013 derived from dropsonde data. The dashed line indicated the atmospheric boundary layer height. The distance from the ice edge is calculated along the 2.5° E meridian.

26 March

The case on 26 March was very unusual because the large ice free Whaler's Bay polynya north of Svalbard enabled a CAO that was oriented from northeast towards southwest (Fig. 4.5d). Eight dropsondes were realeased over the polynya, starting at 81.2° N, 19.9° E until 78.5° N, 3.3° E. Along the flight path the wind direction turned from northeast to nearly north. Only the first four dropsondes located in the northeasterly part of the flight section show a nearly continuous evolution of the ABL. Due to the orientation of the ice edge together with the turning of the wind vector the fetch lengths over open water stayed at a nearly constant value of 170 km for the last four dropsondes located in the southwesterly part of the flight section. For this reason, the ABL height and mean meteorological variables show nearly no changes for these four dropsondes (see Fig. 4.6d and 4.11), which is a remarkable situation.

The first four dropsondes are not affected by these anomalous fetch conditions and show an increase of the mean boundary layer potential temperature from 248 K over the pack ice to 257 K at the north-western corner of the Svalbard archipelago (Fig. 4.6d). Simultaneously, the boundary layer height increased from 200 to a maximum of more than 1100 m at a position 166 km downstream of the ice edge. Even though this maximum value is in the usual range of convective ABL heights during CAOs, it is quite unusual for a latitude north of 80° N (see e.g. measurements by Brümmer (1997), Fig. 4.8). Average boundary layer heights north of Svalbard are mostly below 300 m in winter according to an ERA-40 climatology from 1957 to 2002 by Wetzel and Brümmer (2011, their Fig. 7).

As for the other three cases there is also an increase of the wind speed and the specific humidity downstream of the ice edge (Fig. 4.11). The maxima of both variables occurred at a distance of 223 km, which is roughly 60 km further downstream than the observed maximum ABL height. It is also interesting to note that there is a distinct change in wind speed at the inversion height. Wind speeds within the ABL range from 7 $m s^{-1}$ over the ice to a maximum of almost 18 $m s^{-1}$, while the wind speed above the inversion is mostly between 5 and 8 $m s^{-1}$.

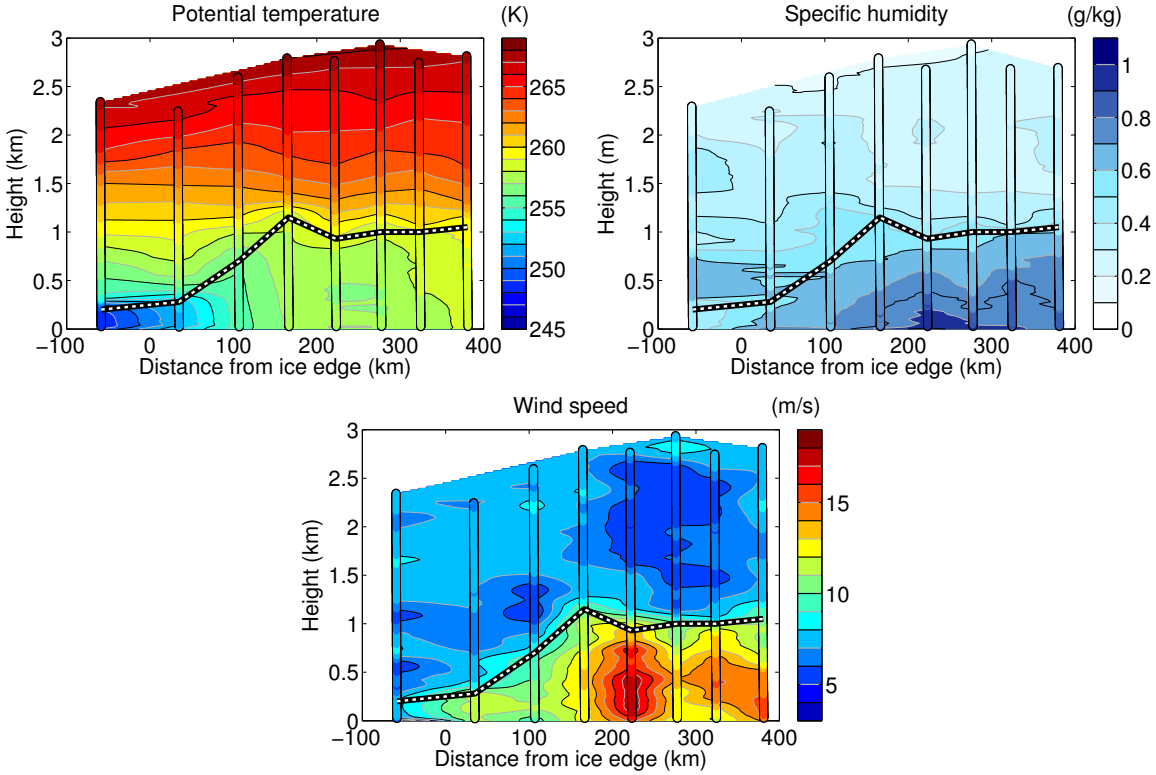

Figure 4.11: Vertical cross-sections of **(a)** potential temperature, **(b)** specific humidity, and **(c)** wind speed on 26 March 2013 derived from dropsonde data. The dashed line indicated the atmospheric boundary layer height. The distance from the ice edge is calculated along the aircaft flight path from northeast to southwest.

4.2.3 Impact of the size of the Whaler's Bay polynya on CAOs

We showed that the large ABL heights observed during the two case studies on 4 and 26 March are unusual compared to observations during previous campaigns in this region (e.g. Brümmer, 1997; Hartmann et al., 1997). They are only present because of the large size of the Whaler's Bay polynya north of Svalbard in March 2014. This sensible heat polynya forms due to the West Spitsbergen Current that causes upwelling of warm Atlantic water (Aagaard et al., 1987; Ivanov et al., 2012). Based on remote sensing data, Ivanov et al. (2012) observed a decrease in the ice concentration north of Svalbard in winter and spring by more than 10 % in the period between 1999 and 2011 compared to the period between 1979 and 1995. Using a similar method, Onarheim et al. (2014) found an ice reduction of 10 % decade^{-1} north of Svalbard between 1979 and 2012. They identify a temperature increase of the inflowing Atlantic water as a major driver for this long-term trend, while the year-to-year variability is also influenced by wind direction. Both studies also found an increase in the near-surface air temperatures in the European Centre for Medium-Range Weather Forecasts (ECMWF) Re-Analysis Interim (ERA-Interim) data in this area, which is in line with the decreasing ice concentration in the last decades. In the following two sections we show that the extent of the Whaler's Bay polynya north of Svalbard was much larger in the years 2012 to 2014 than ever observed in the previous two decades. We demonstrate that the strong atmosphere–ocean interaction above the polynya alters not only the structure of the ABL during CAOs but can also have a large impact on the local temperatures around Svalbard.

Polynya size from 1992 to 2015

The wintertime (January-March, JFM) variability of the Whaler's Bay sea ice cover between 1992 and 2015 is studied using daily SSM/I ice concentration data provided by Ifremer/Cersat (`http://cersat.ifremer.fr`) with a spatial resolution of 12.5 km on the basis of the ASI retrieval algorithm by Spreen et al. (2008).

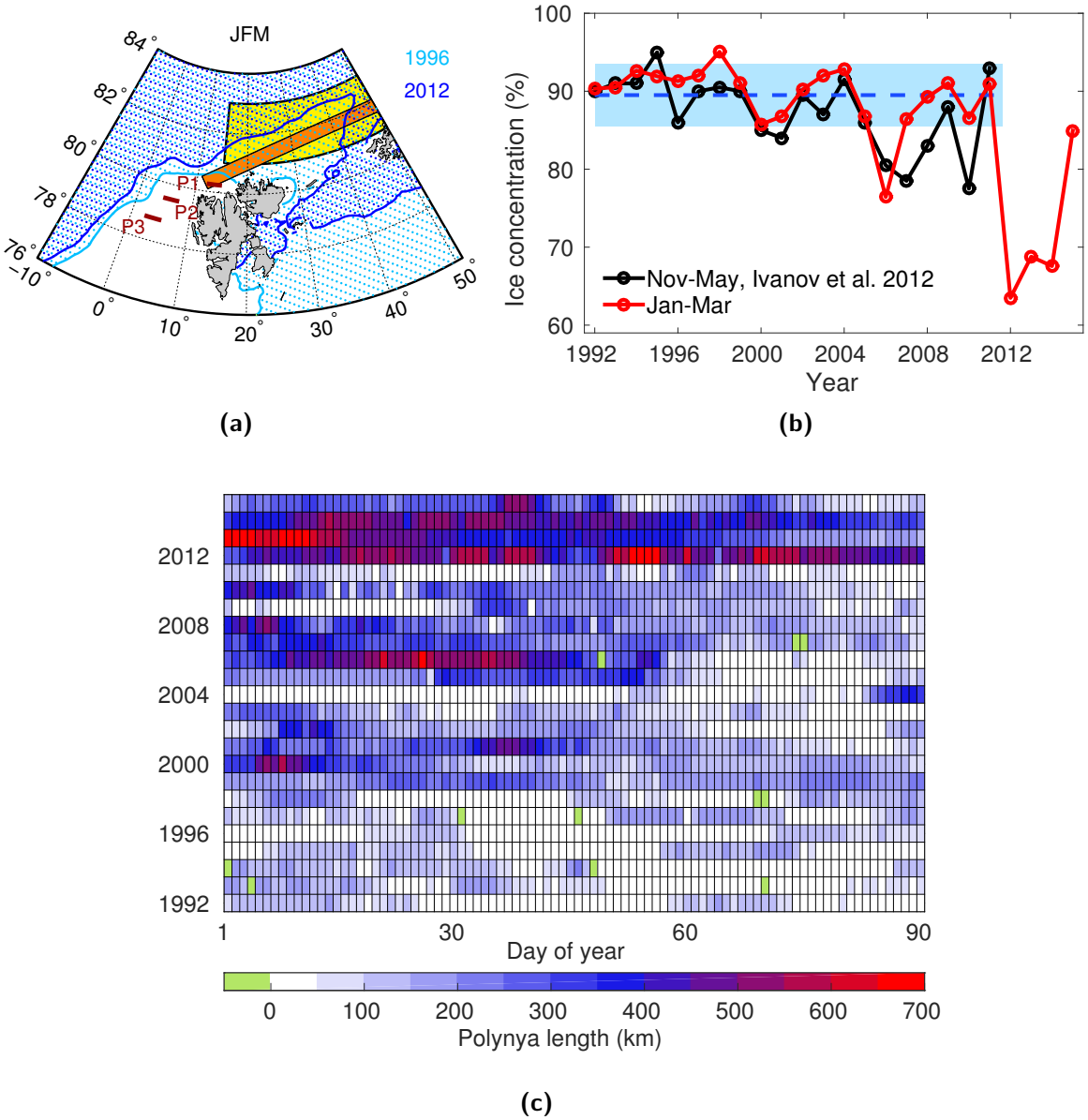

Figure 4.12: **(a)** Mean JFM ice edge (based on 70 % SSM/I-ASI ice concentration) in 1996 (light blue) and 2012 (dark blue), and areas used for calculation of the mean ice concentration in the Western Nansen Basin (WNB, yellow) and the length of the Whaler's Bay polynya (orange). The three positions (P1–P3) used for the temperature analysis are marked in dark red. **(b)** Time series of the winter mean sea ice concentration in the WNB (red) with the 20 year mean and one standard deviation (blue). Data from Ivanov et al. (2012) are shown for comparison (black). **(c)** Polynya length for the years 1992 to 2015 as a function of day of the year. Green color denotes missing data.

We calculate the JFM mean ice concentration as in Ivanov et al. (2012) in a region northeast of Svalbard expanding from 15 to 60° E and 81 to 83° N (Fig. 4.12a) referred to in the following as the Western Nansen Basin (WNB). Although Ivanov et al. (2012) considered the period from November till May and used ice concentration data with 25 km resolution, the two time series of mean ice concentrations show the same general characteristics (see Fig. 4.12b). We find a 20 year mean of 89.5 ± 4.0 % from 1992 to 2011 which compares reasonably well with the value of 87.5 ± 5.0 % by Ivanov et al. (2012) for this period. In the winters of 2012 to 2014, however, there is a sudden decrease of the mean ice concentration to below 70 %, which is more than four standard deviations below the 20 year mean. However, these three years with a very large polynya size do not imply a general shift of the regime to lower ice concentrations. In 2015 the mean ice concentration in the polynya region increased again to about 84.9 %, which is closer to the values before 2012 but still one standard deviation below the 20 year mean.

Another useful quantity is the polynya length, which – as has been shown in the previous sections – is an important factor influencing the evolution of the convective atmospheric boundary layer during CAOs. We define the polynya length as the cumulative open water path along the yellow area in Fig. 4.12a, starting at the northwestern edge of Svalbard. Here, we consider pixels with ice concentrations below 70 % as open water areas. The polynya length is then the distance to the ice edge, i.e. the first pixel exceeding 70 % ice concentration. Daily values of the polynya length are shown in Fig. 4.12c. In the winters of 1992 to 1998 the polynya length hardly ever exceeded 200 km while lengths exceeding 300 km occurred more frequently between 1999 and 2011. As for mean ice concentration, 2012 to 2014 were also exceptional in terms of the polynya length with values exceeding 400 km more than 40 % of the time. 2014 is also a remarkable year because the polynya length decreased from more than 500 km at the end of January to nearly 0 km in mid-April. The polynya remained closed until mid September (not shown).

Polynya impact on atmospheric temperatures

It is also interesting to consider the impact of polynyas on local atmospheric temperatures (e.g. Raddatz et al., 2013; Ebner et al., 2011; Fiedler et al., 2010). Using ERA-Interim data, Onarheim et al. (2014) found an air temperature increase of 7 K in the Whaler's Bay polynya between 1979 and 2012 associated with the observed decrease in sea ice cover. The close connection between

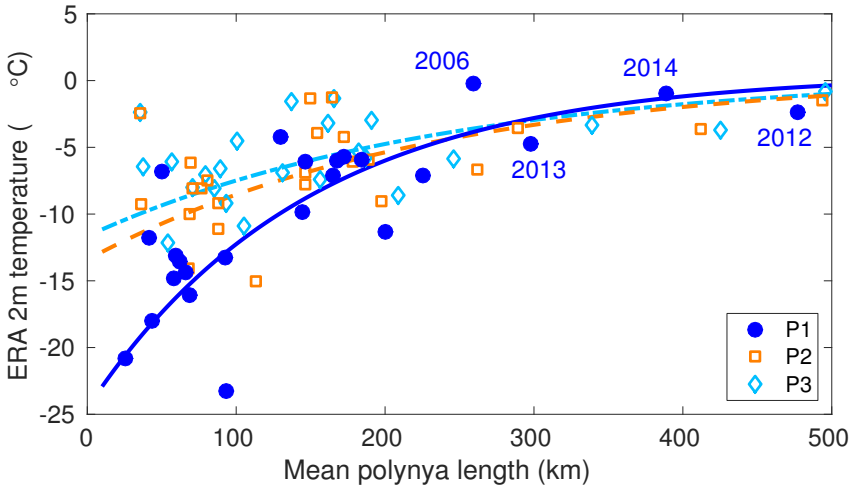

Figure 4.13: JFM mean ERA-Interim 2 m air temperature at three positions (P1–P3) north and west of Svalbard (see text) during times with wind from NE as a function of polynya length from 1992 to 2015 (symbols). The lines represent exponential fits.

the size of the Whaler's Bay polynya and the local temperature in the polynya region can be seen in Fig. 4.13. There, we show ERA-Interim (Dee et al., 2011) 2 m air temperatures that are available every six hours to determine the impact of the polynya size on local temperature conditions. The temperature is considered at grid points located north of Svalbard (80.25° N, 12–15° E , P1, see Fig. 4.12a) and for north-easterly winds (30–60°) only, which are identified from the 10 m wind field of ERA-Interim.

The relationship between the JFM mean temperatures during north-easterly winds and the mean polynya length of the considered cases is probably not linear since temperatures will roughly approach the water temperature for larger polynya lengths. Therefore, we calculate the Spearman rank correlation that can be used to test the strength of a non-linear relationship. We find a strong correlation of $r_s = 0.77$. This is in line with the more general findings by Ivanov et al. (2012), who concluded that air temperature trends in the Western Nansen Basin based on ERA-Interim data are consistent with the observed ice loss. Thus, depending on the temperature of the inflowing air masses, near-surface temperatures north of Svalbard can be more than 20 K higher in years with a large polynya extent compared to years with a closed ice cover.

To estimate how far south air temperatures are influenced by the polynya size, we repeat the calculations for two additional points further downstream. They are located north-west of Svalbard at 79.5° N, 4.5–7.5° E (P2 in Fig. 4.12a) and at 78.75° N, 2.25–5.25° E (P3 in Fig. 4.12a). The results are also shown in Fig. 4.13. The Spearman rank correlation gradually decreases to $r_s = 0.52$ at P2 and $r_s = 0.43$ at P3. Thus, an effect is still visible more than 200 km downstream. At ERA-Interim grid-points even further to the south, the air temperatures are nearly in equilibrium with the water temperatures and no significant correlations can be found.

Increased boundary layer heights could also lead to a thicker cloud layer with enhanced precipitation. However, the analysis of ERA-Interim results did not show a significant correlation (not shown). It would be interesting to examine polynya related changes in snowfall and a possible impact on the surface mass balance of glaciers in northern Svalbard in the future.

4.2.4 Remarks on modeling applications

Aircraft measurements of meteorological variables in CAOs, such as the ones presented here, are very useful for testing and improving parametrisations of turbulent fluxes within the ABL and of entrainment fluxes near the inversion layer. As a simplification and to save computing time an often used approach is to set up a quasi two-dimensional model domain with only few grid points in the cross wind direction (e.g. Chrobok et al., 1992; Lüpkes and Schlünzen, 1996).

Only two (6 and 7 March) of our four cases are suitable for comparison with such a 2D simulation since there the backward trajectories are mostly aligned with the flight track. However, the situation is more complicated on 4 March, where the fetch was increased due to a north-easterly wind component, and on 26 March, where orographic effects of the Svalbard mountains modify the flow field. It would be interesting to study these two cases in a full 3D model setup to gain more insight into the effects of a changing flow field with distance to the ice edge.

4.3 CAO 1D modeling aspects

4.3.1 Turbulence parametrisations

The turbulent fluxes of sensible and latent heat, and momentum represent non-linear terms in the conservation equations of energy and momentum. Due to these terms the set of equations is not closed and cannot be solved directly in mesoscale and climate models but have to be parametrised. Many different parametrisations have been suggested to solve this turbulence closure problem. In the following, we focus on those parametrisations that are relevant for the modeling of the temperature evolution and ABL growth in the convective boundary layer in CAOs. Thus, we only consider parametrisations of sensible heat fluxes. For simplicity, we assume a dry atmosphere and neglect the influence of humidity.

We test the performance of three different turbulence closures for the calculation of sensible heat fluxes in a convective atmospheric boundary layer that is typical for CAOs. For this purpose, we use a 1D version of the MEsoscale TRAnsport and Stream model (METRAS, Schlünzen, 1988), which is non-hydrostatic and anelastic. The applied parametrisations are a mixing length closure (ML), a counter-gradient closure (CG), and a so-called eddy-diffusivity mass-flux closure (EDMF), which are described in the following sections. The ML and CG closures have already been implemented in METRAS and their performance was tested in Lüpkes and Schlünzen (1996) for CAOs. The EDMF closure has not yet been used in METRAS and was implemented in the framework of this thesis. It is based on a formulation proposed by Siebesma et al. (2007), which we improved by ensuring continuous fluxes between the surface layer and the layers above.

Mixing length approach (ML)

The simplest and most commonly used parametrisation of the vertical temperature flux is a local closure of the form

$$\overline{w'\theta'} = -K_H \frac{\partial \overline{\theta}}{\partial z}, \tag{4.4}$$

where $\partial\overline{\theta}/\partial z$ is the local gradient of potential temperature and K_H is an eddy diffusivity coefficient. For simplicity, a dry atmosphere is considered. A variety of different parametrisations for the eddy diffusivity exists in the literature. The one implemented in METRAS is a mixing length scheme based on Herbert and Kramm (1985) with a stability correction that goes back to functions traditionally used for surface fluxes by Dyer (1974). This results in:

$$K_H = \begin{cases} l_n^2 |\frac{\partial v}{\partial z}| (1 - 5Ri)^2 & 0 \leq Ri \leq 0.2 \\ l_n^2 |\frac{\partial v}{\partial z}| (1 - 16Ri)^{3/4} & -5 \leq Ri \leq 0. \end{cases} \tag{4.5}$$

Ri is the local Richardson number and l_n is the mixing length for neutral stratification that is specified according to Blackadar (1962) as

$$l_n = \frac{\kappa z}{1 + \frac{\kappa z}{\lambda}}. \tag{4.6}$$

$\kappa = 0.4$ is the von Kármán constant and the maximum mixing length λ is specified as a function of the ABL height z_i. We use the relationship $\lambda = 0.15 z_i$ derived by Brown (1996) from LES simulations under neutral conditions.

Counter-gradient approach (CG)

Local closures work well in stable conditions, however it has been shown in different studies (e.g. Holtslag et al., 1995; Lüpkes and Schlünzen, 1996; Siebesma et al., 2007) that it has limitations in convective conditions, where the vertical heat transport is not only governed by local gradients but a large part of it is caused by plumes and thermals of rising warm air. To account for this additional upward transport also in regions with a local increase of potential temperature with height a so-called counter-gradient term Γ is added so that

$$\overline{w'\theta'} = -K_H \left(\frac{\partial \overline{\theta}}{\partial z} + \Gamma \right). \tag{4.7}$$

The specification of the counter-gradient term and the eddy-diffusivity in METRAS follow the suggestions by Holtslag and Moeng (1991) and Lüpkes and Schlünzen (1996) (LS96). The counter-gradient term is

$$\Gamma = 3 \frac{w_f \overline{w'\theta'}|_s}{\overline{w'^2} z_i}, \tag{4.8}$$

where $\overline{w'\theta'}|_s$ is the temperature flux at the surface and w_f is a convective velocity scale that can be expressed as

$$w_f = \left(\frac{g}{\theta_s} z_i \overline{w'\theta'}|_s \right)^{1/3}. \tag{4.9}$$

The eddy diffusivity between the lowest model grid level z_p and the ABL height z_i is specified as

$$K_H = \frac{\kappa u_* z_p}{\Phi_H - \frac{\kappa z_p}{\theta_*} \Gamma|_{z_p}} \left(\frac{z_i - z}{z_i - z_p} \right)^2 \frac{u_* \kappa z + w_f z_i (z/z_i)^{4/3}}{u_* \kappa z + w_f z_i (z_p/z_i)^{4/3}}, \tag{4.10}$$

with the variance of the vertical velocity $\overline{w'^2}$ according to Holtslag and Moeng (1991):

$$(\overline{w'^2})^{3/2} = \left(1.6 u_*^2 \left(1 - \frac{z}{z_i} \right) \right) + 1.2 w_f^3 \left(\frac{z}{z_i} \right) \left(1 - 0.9 \frac{z}{zi} \right)^{3/2}. \tag{4.11}$$

Eddy-diffusivity mass-flux approach (EDMF)

In the counter-gradient closure the impact of the convective thermals is parametrised. Another possibility is to treat the flux caused by thermals explicitly, as is commonly done in parametrisations of convective clouds (e.g. Tiedtke, 1989; Bechtold et al., 2001). Siebesma et al. (2007) combined this so-called mass-flux approach with the local eddy-diffusivity closure for applications in the cloud free convective ABL. One of the advantages of this approach is that it is easily matched with mass-flux parametrisations for the cloud layer, which allows for a unified parametrisation for the cloud topped ABL.

For the derivation of the parametrisation, the fields of potential temperature and vertical wind are divided into contributions by strong updrafts (denoted by the subscript u) that cover a small area fraction a_u and by the environmental values that can be approximated by the spatial mean fields (denoted by an overbar). An overview is given in Fig. 4.14. The heat flux is then parametrised as a mass-flux contribution (MF, second term in Eq. 4.12) of the updrafts and a diffusive contribution (ED, first term in Eq. 4.12) in the environment:

$$\overline{w'\theta'} = -K_H \frac{\partial \overline{\theta}}{\partial z} + M(\theta_u - \overline{\theta}), \tag{4.12}$$

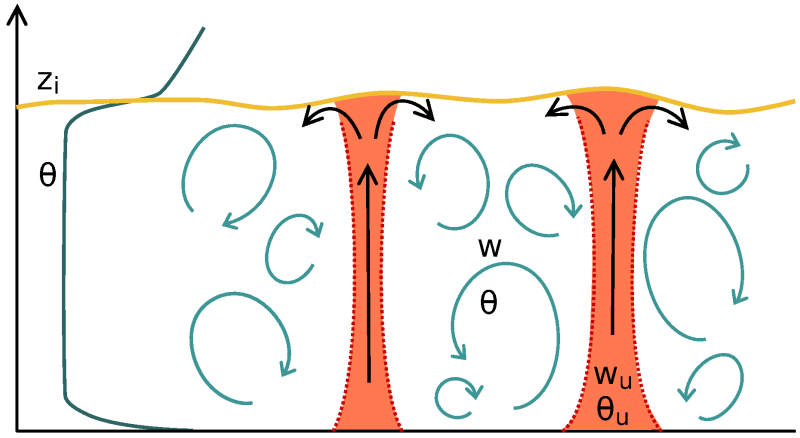

Figure 4.14: Overview sketch of the EDMF principle. Adapted from Siebesma et al. (2007).

with the mass flux

$$M = a_u w_u \approx 0.3\sigma_w. \tag{4.13}$$

Here, M is approximated as a function of the standard deviation of the vertical velocity σ_w for which the following empirical relationship has been derived by Holtslag and Moeng (1991) from LES data:

$$\sigma_w = 1.3 w_f \left(\left(\frac{u_*}{w_f} \right)^3 + 0.6 \frac{z}{z_i} \right)^{1/3} \left(1 - \frac{z}{z_i} \right)^{1/2}. \tag{4.14}$$

Siebesma et al. (2007) assumed that $\theta_s = 300\,\mathrm{K}$ for the calculation of the scaling parameter for vertical velocity w_f defined as in Eq. 4.9.

The EDMF parametrisation requires steady-state updraft equations for potential temperature and vertical velocity that are derived from mass continuity equation and steady state Boussinesq equation as

$$\frac{\partial \theta_u}{\partial z} = -\epsilon(\theta_u - \overline{\theta}) \tag{4.15}$$

and

$$\frac{\partial w_u^2}{\partial z} = -\frac{1}{0.7}\epsilon w_u^2 + \frac{g\beta}{0.35}(\theta_u - \overline{\theta}). \tag{4.16}$$

ϵ is the fractional entrainment rate that described the lateral entrainment of air into the updrafts. Siebesma et al. (2007) derived the following empirical formulation from LES data:

$$\epsilon \simeq 0.4 \left(\frac{1}{z + \Delta z} + \frac{1}{z_i - z + \Delta z} \right). \tag{4.17}$$

They introduced the additional terms Δz to avoid singularities near the ABL height z_i.

For each time step the diagnostic equations for updraft potential temperature (Eq. 4.15) and vertical velocity (Eq. 4.16) are evaluated stepwise starting from the lowest model level z_p using the initial values

$$\theta_u(z_p) = \overline{\theta}(z_p) + \frac{\overline{w'\theta'_s}}{\sigma_w(z_p)} \tag{4.18}$$

and

$$w_u(z_p) = 0. \tag{4.19}$$

The diagnostic equation for the updraft vertical velocity is used to derive the ABL height. Here,

the top of the ABL is defined as the height where $w_u = 0$. An example of the updraft velocity and the corresponding ABL height are shown in Fig. 4.15a. The results were obtained using a 1D version of METRAS using the initial conditions and the model setup described in Sect. 4.3.2.

For the eddy diffusivity coefficient in Eq. 4.12 Siebesma et al. (2007) use the following profile relationship:

$$K'_H(z) = \frac{\kappa z u_*}{\Phi_H} \left(1 - \frac{z}{z_i}\right)^2. \tag{4.20}$$

In general, it is important that for any used parametrisation of turbulent fluxes the formulation is consistent with the fluxes in the Prandtl-layer, which is basically the layer below the lowest model grid point z_p. This means that a parametrisation needs to guarantee vertically continuous fluxes at the first grid point. Therefore, we inspect if this is the case for the EDMF parametrisation in the following.

For sensible heat flux, continuous fluxes are ensured when the parametrisation meets the following condition:

$$\overline{w'\theta'}|_{z_p} = -u_*\theta_* = -K_H(z_p) \left.\frac{\partial \theta}{\partial z}\right|_{z_p} + M|_{z_p}(\theta_u(z_p) - \overline{\theta}(z_p)). \tag{4.21}$$

However, this condition is not fulfilled when the eddy-diffusivity in Eq. 4.20 is used. Thus, we use a simple approach, as in LS96, and multiply the eddy diffusivity by a factor A to meet the condition:

$$K_H(z) = A \cdot K'_H(z). \tag{4.22}$$

Inserting Eq. 4.22 in Eq. 4.21 and solving for A gives:

$$A = \frac{u_*\theta_* + M|_{z_p}(\theta_u(z_p) - \overline{\theta}(z_p))}{\frac{\partial \theta}{\partial z}|_{z_p} K'_H(z_p)} = \left(1 + \frac{M|_{z_p}(\theta_u(z_p) - \overline{\theta}(z_p))}{u_*\theta_*}\right) \left(\frac{z_i}{z_i - z_p}\right)^2. \tag{4.23}$$

With the mass-flux contribution at the lowest model level according to Eq. 4.13 and 4.18

$$M|_{z_p}(\theta_u(z_p) - \overline{\theta}(z_p)) = 0.3\sigma_w(z_p)\frac{\overline{w'\theta'_s}}{\sigma_w(z_p)} = -0.3u_*\theta_* \tag{4.24}$$

we obtain the modified eddy diffusivity as

$$K_H(z) = 0.7\ \frac{\kappa z u_*}{\Phi_H} \left(\frac{z_i - z}{z_i - z_p}\right)^2. \tag{4.25}$$

To illustrate the contributions of the eddy-diffusivity (ED, first term in Eq. 4.12) and mass-flux (MF, second term in Eq. 4.12) terms to the total flux in the EDMF parametrisation, exemplary results from a 1D model run of METRAS are shown in Fig. 4.15b. The presented curves are results after 24 h model run time using the initial conditions and the model setup described in Sect. 4.3.2. Near the surface the total flux is dominated by the ED term, while the mass-flux equals zero below the lowest grid point. The contribution of the MF term increases within the lowest 10 % of the ABL while the ED contribution decreases. In the upper 60 % of the ABL the ED term is even slightly negative. The two contributing terms add up to a total flux that linearly decreases with height and has a minimum at the top of the ABL. This minimum is dominated by the mass-flux term.

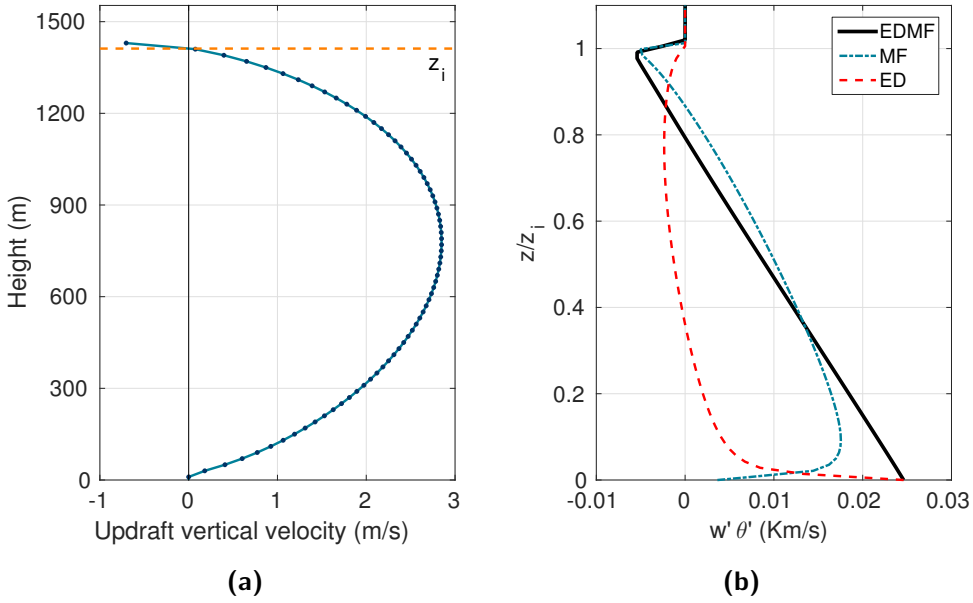

Figure 4.15: **(a)** Vertical profile of the updraft velocity according to Eq. 4.16 and derived ABL height z_i. **(b)** Vertical temperature flux as a function of normalized height using the EDMF parametrisation (Eq. 4.12) and contributions from the eddy-diffusivity (ED) and mass-flux (MF) terms. Both figures show results of a model run performed with a 1D version of METRAS after 24 h. For initial conditions and model setup see Sect. 4.3.2.

4.3.2 Comparison of results from 1D METRAS runs using different parametrisations with LES results

To test the performance of the above mentioned parametrisations they were implemented in a 1D version of METRAS and results were compared with LES. The model was initialized with a stably stratified atmosphere with a constant vertical potential temperature gradient of $\partial\theta/\partial z = 0.005\,\mathrm{K\,m^{-1}}$ starting at a value of θ = -12 °C near the surface. These conditions can be considered as representative for Arctic autumn or late spring conditions over thick sea ice. The geostrophic wind speed was $3\,\mathrm{m\,s^{-1}}$, which is at the lower end of the range of different values observed by Brümmer (1997). After initialisation an abrupt increase of the surface temperature to -2 °C was prescribed to generate near-surface heat fluxes with a similar magnitude as during CAOs. Results can be considered as a function of time but also in a Lagrangian way as a function of distance by assuming that the model box drifts with the mean wind.

As a first estimate of the "truth" we compare the results obtained with METRAS to results from large-eddy simulation. The model run was performed with the Parallelized Large Eddy Simulation Model (PALM, Raasch and Schröter, 2001)[1]. The horizontal and vertical resolutions were 30 m for PALM and the vertical resolution was 20 m for METRAS. The model run times were 20 h. Since the first two hours of the PALM run are necessary for spin up, the METRAS runs were initialised with the PALM profiles of potential temperature after 2 h to ensure consistent results.

The resulting profiles of potential temperature after model run times of 6, 12, and 18 hours are shown in Fig. 4.16. The PALM profiles show a well-mixed ABL with a near-neutral stratification in the center of the ABL and a slightly stable stratification in the uppermost 20 to 30 % of the

[1]The model runs with PALM were performed by Siegfried Raasch from the Institute of Meteorology and Climatology, University of Hannover.

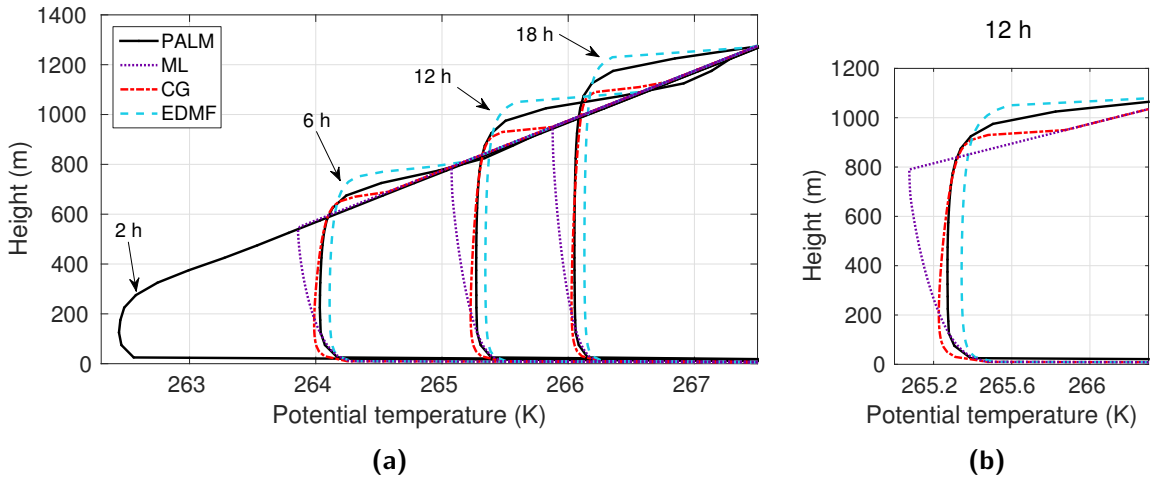

Figure 4.16: Vertical profiles of potential temperature from model runs of a 1D version of METRAS using the mixing-length (ML), counter-gradient (CG), and eddy-diffusivity mass-flux (EDMF) parametrisations and from the LES model PALM. **(a)** Results after model run times of 6, 12, and 18 hours and the LES profile after 2 hours used to initialize the METRAS runs. **(b)** Zoom in to the profiles after 12 hours.

ABL. The growth of the ABL beyond the intersection of a given profile with a previous profile indicates the existence of vertical entrainment in the inversion region. Consistent with LS96 we find that the potential temperature profiles produced with METRAS using the ML approach show an unrealistically unstable stratification in the upper 90 % of the ABL. However, this effect is much smaller than described by LS96, which is due to different values of the coefficient λ in Eq. 4.6. LS96 used the original Blackadar (1962) approach with a value of $\lambda = 0.007 u_*/f$, where f is the Coriolis parameter, which is larger than the parameter used here. Consequently, the potential temperatures near the inversion height are underestimated by more than 0.2 K for all time steps. The ML parametrisations also fails to reproduce the stably stratified region in the upper part of the ABL and cannot reproduce the entrainment present in the PALM runs. As a result, the ABL does not grow fast enough and the ABL height after 20 h of about 1000 m is more than 100 m smaller than the ABL height in PALM (Fig. 4.17b).

The METRAS runs using the CG approach reproduce the temporal evolution of the increase of the mean ABL potential temperature and the stable stratification in the upper part of the ABL very well (Fig. 4.16). However, in the CG run the potential temperature increase starts already in the lower part of the ABL, where PALM shows a height constant temperature. This small discrepancy has not yet been described by LS96. Other than the ML closure, the CG closure reproduces the entrainment present in the PALM run and thus the ABL growth agrees very well with the PALM results (Fig. 4.17b). However, the extent of the entrainment layer is slightly too small.

The newly introduced EDMF parametrisation is the only one that reproduces the near-neutral stratification obtained by PALM over large parts of the ABL (Fig. 4.16). The mean ABL potential temperatures are, however, slightly higher than in the PALM runs for all time steps. The slightly too warm ABL coincides with an overestimation of the initial growth of the ABL, leading to ABL heights that exceed the PALM results by up to 250 m after 20 h (Fig. 4.17b).

However, it should be noted here that the definition of the ABL height is different for the EDMF approach than for the two other used parametrisations and for PALM. The ABL height is determined from the zero-crossing of the updraft vertical velocity in the EDMF approach, which roughly corresponds to the height of the maximum potential temperature gradient in the capping

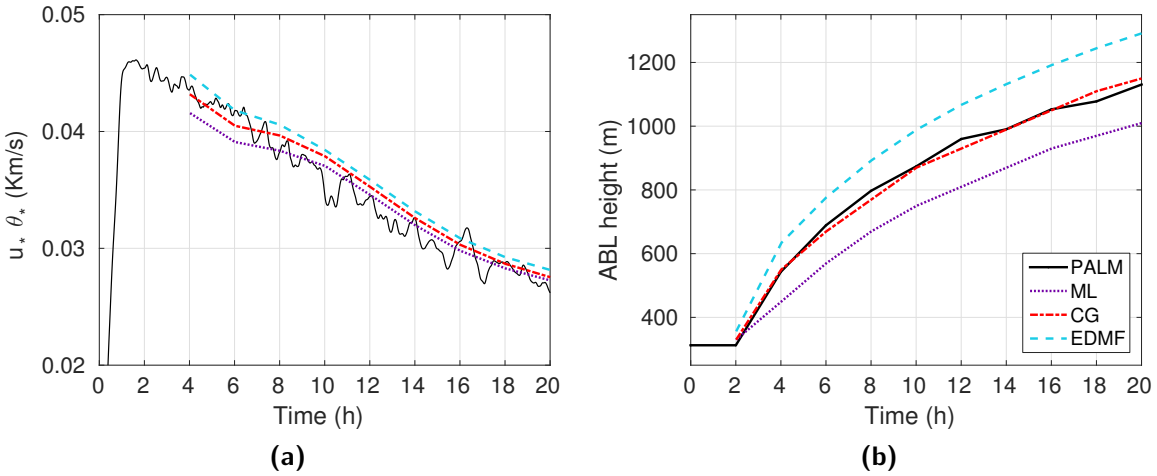

Figure 4.17: Time evolution of **(a)** surface heat fluxes and **(b)** ABL height derived from model runs of a 1D version of METRAS using the mixing-length (ML), counter-gradient (CG), and eddy-diffusivity mass-flux (EDMF) parametrisations and from the LES model PALM.

inversion. The resulting ABL heights are higher than those derived for the other cases, which are based on a critical value for the potential temperature gradient and thus place the ABL height close to the inversion base. Consequently, as can be seen in the profiles in Fig. 4.16, the actual overestimation of the ABL heights using the EDMF closure is not as large as suggested by the values in Fig. 4.17b. The different definitions of the ABL height also perform differently when the vertical grid spacing is increased, as we will demonstrate in the next section.

4.3.3 Sensitivity to vertical grid spacing

The comparison and evaluation of different flux parametrisations is also relevant for the choice of parametrisations in climate and reanalysis models. In those models the vertical grid spacing is usually much larger than the 20 m used in the METRAS test case presented in the previous section. For example, in the ERA-Interim reanalysis, which has 60 vertical levels, the vertical grid size increases from about 20 m near the surface to about 200 m at 1 km height (The ERA-Interim archive, version 2.0, 2011). Similar values or slightly higher vertical resolutions in the lower troposphere are currently used in many climate models, such as ECHAM6 (Stevens et al., 2013, (47 levels)), IPSL-CM5 (Dufresne et al., 2013, (39 levels)), or the NCAR CCSM4 model (Gent et al., 2011, (26 levels)).

Thus, in addition to the comparison with LES results in the previous section, it is interesting to analyse the performance of the different parametrisations for an increased vertical grid spacing. For this purpose, additional 1D METRAS runs with a vertical grid spacing that agrees at the surface with the height constant value of 20 m used in the reference run, but increases then with height were performed and compared to the high resolution runs. In this new model setup Δz equals 20 m below $z = 200$ m and increases to 50 m at 500 m height and further to 100 m at 2000 m. The initial conditions for wind speed and stratifications are the same as for PALM described in the previous section. We only use the CG and EDMF approaches for this comparison since the characteristics of the convective ABL during CAOs are not well reproduced by the ML approach.

Figure 4.18a shows the potential temperature profiles after a model run time of 24 h. It is evident that the largest changes between the model runs with high and with increasing vertical grid spacings occurs for the CG approach, when the ABL height is determined by a critical

temperature gradient (full lines, "grad" criterion). There, the ABL grows and warms much faster when the vertical grid spacing is increased. The ABL height for the decreased resolution run exceeds the ABL heights for the high resolution run by more than 200 m after 24 h and by about 700 m after 3 days (Fig. 4.18b,c). Considering the wind speed of 3 $m s^{-1}$ this means that after a distance of only 780 km (or about 7° latitude for a flow in north-south direction) the ABL height is overestimated by already 30 %. Such a horizontal scale of several hundreds of kilometers has often been observed for CAOs in the Fram Strait region (e.g. Brümmer and Pohlmann, 2000; Brümmer, 1997).

The changes of the ABL height for an increased grid spacing are much smaller when the EDMF approach is used (Fig. 4.18, dashed lines), although there is a similar slight increase of the mean ABL potential temperature as for the CG approach in the order of 0.1 K after 24 h. The ABL height is only slighly overestimated for an increased grid size with differences in the order of 50 m after 3 days. An explanation for this different behavior are the different methods used to determine the ABL height, as already pointed out in the previous section. Our results suggest that the criterion based on the zero-crossing of the updraft velocity ("w_u" criterion), as used in the EDMF approach, is much less sensitive to the choice of the vertical grid.

To support this finding we tested whether the CG results improved when the w_u criterion was used to determine the ABL height instead of the grad criterion. These results are shown as dotted lines in Fig. 4.18. Indeed, the overestimation of the ABL with increased vertical grid spacing is largely reduced with only about 100 m after 24 h and 150 m after 3 days. Thus, the error decreases from 30 % to about 7 % for typical horizontal scales of CAOs.

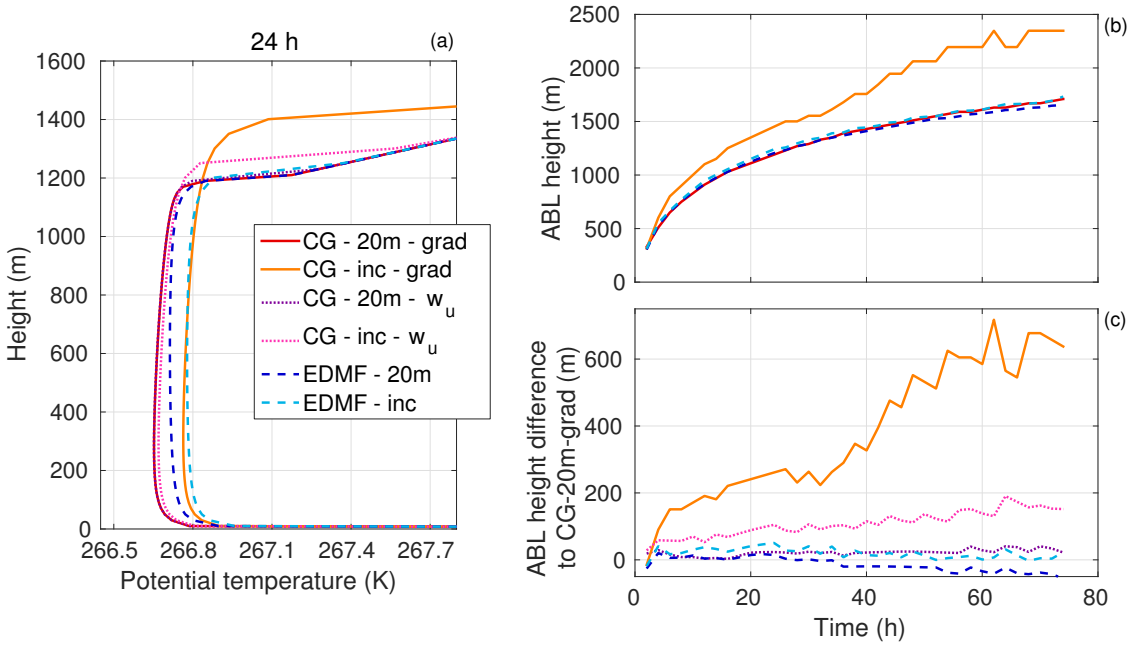

(a)

Figure 4.18: Results for model runs using the CG and EDMF closures with "20 m" and with increasing ("inc") vertical grid spacing. Two versions of the CG approach are shown where the calculation of the ABL heights is based on a critical temperature gradient ("grad") or on the zero-crossing of the updraft velocity ("w_u"). **(a)** Potential temperature profiles after 24 h, **(b)** time evolution of the ABL height, and **(c)** differences of the ABL heights of the high resolution run (using the CG closure and the gradient method to derive the ABL height) to the ABL heights from all other cases.

4.3.4 Summary

In a comparison of LES results with 1D METRAS runs using different parametrisations we demonstrated that the recently introduced EDMF closure by Siebesma et al. (2007) is useful in CAO modeling applications and even has some advantages compared to the CG appraoch. While all three considered parametrisations reproduce the surface heat fluxes reasonably well, the EDMF closure yields the best agreement of the temperature profiles with LES, with a near-neutral stratification in the center and a slightly stable stratification close to the capping inversion. However, in the presented case for the EDMF closure the ABL grew too fast and was slightly too warm compared to the LES results. The EDMF approach is also less sensitive to the vertical grid spacing than the CG closure, which can be attributed to the derivation of the ABL height using a diagnostic equation of the updraft vertical velocity (Eq. 4.16). We showed that for the CG approach the overestimation of the ABL height caused by an increased vertical grid spacing can be reduced when the ABL height is also derived from the updraft velocity rather than from a critical potential temperature gradient.

This is especially relevant for an appropriate parametrisation of fluxes in climate models where the vertical grid spacing in the lower troposphere can be even larger than the maximum of 100 m at 2 km height considered in this study. There, a definition of the ABL height based on the updraft velocity could be a simple method to reduce errors of the ABL growth during CAOs. Since the required additional equation is only diagnostic, the added costs would remain within reasonable bounds.

5 Conclusions

In this study we examined convective processes in the polar atmospheric boundary layer. This includes convection over sea ice covered regions, which is caused by the presence of leads and the related heterogeneous distribution of sea ice concentration and thickness. Moreover, we also considered convection during cold air outbreaks at the sea ice edge. A large part of these investigations was based on aircraft measurements. They were supplemented by modeling results obtained with a simple box model and a one-dimensional mesoscale model.

Surface temperature impact on Arctic air temperatures

The aim of the first major part of this thesis was to investigate the dependence of near-surface atmospheric temperatures on the heterogeneity of surface temperatures over the Arctic Ocean. We used a Lagrangian approach based on backward-trajectories calculated from 10 m wind fields of two different reanalysis data sets. The trajectories were initiated at three Arctic locations, namely Alert, Barrow, and at the Tara drifting station. We applied three different methods to relate the measured 2-m temperatures at these stations to the ice cover in their upstream regions, which included calculations with a simple box model that only accounted for the effect of sensible heat fluxes. The model used MODIS ice surface temperatures and four different sets of satellite-derived ice concentrations as input data.

We found that, under nearly cloud-free conditions, up to 90 % of the 2-m air temperature variance at the stations can be explained by heterogeneous ice surface temperatures. The results also suggest that near-surface temperatures at a given site are influenced by the variability of surface temperatures in a domain of about 200 km radius around the site. These results underline the large importance of a very accurate representation of sea ice properties – such as concentration, thickness, snow cover, and albedo – in climate and weather prediction models.

The results are most sensitive to uncertainties in ice surface temperatures, which are mainly due to shortcomings of the MODIS cloud mask and to uncertainties in the trajectory positions. We found that the trajectories based on the two different reanalyses show large spatial differences of up to 380 km after 30 h in the Central Arctic. The differences are only about 120 km for Barrow, which is located in a region where more in-situ measurements are available for assimilation into the reanalysis model. This might suggest that backward-trajectories based on reanalysis data are less reliable in regions where measurements are sparse. It would be interesting to test this hypothesis by comparing backward-trajectories calculated for additional reanalysis data sets and for other regions with a different coverage of in situ and satellite measurements. It is quite possible that without the uncertainty in the cloud mask and the trajectory positions the spatial surface temperature heterogeneity would explain even a larger fraction of the local air temperature variability than found in the present results.

Influence of leads on the atmospheric boundary layer

In the second major part of this thesis we analysed aircraft measurements in the environment of leads obtained during the campaign STABLE, which took place in March 2013 in the northern Fram Strait region. The measurements over four individual leads aimed to improve our current understanding of the formation of convective plumes over leads and their impact on the polar atmospheric boundary layer. They were supplemented by measurements during long low-level flight legs that were used to estimate the lead impact on a regional scale.

We presented case studies of the boundary layer modification and turbulent fluxes over four wide leads, which differed with respect to environmental conditions and lead characteristics. The conditions over the leads were strongly variable with observed near-surface sensible heat fluxes ranging from 15 to 180 $\mathrm{W\,m^{-2}}$ and an increase of the near-surface temperature of up to 3.2 °C. In two cases the plumes strongly affected the wind field within the atmospheric boundary layer. Low level jets that existed in those cases in the region upstream of the leads disappeared in the plume region.

In one of the cases large entrainment fluxes exceeding 30 % of the surface fluxes were observed, which contributed significantly to the ABL warming downstream of the lead. We found that plumes emanating from leads also affected the structure of the vertical flux profiles, which were non-linear downstream of the leads with a distinct flux maximum in the core of the convective plumes. Furthermore, we found that the presence of leads may cause large errors of the measured sensible heat fluxes when the turbulent fluxes were derived only from flight legs orthogonal to the leads. Uncertainties of near-surface fluxes were much smaller when stacks of lead parallel flight legs at multiple heights were conducted. Therefore, such complex flight patterns are necessary to accurately determine the energy fluxes in the environment of leads.

The convective plumes over leads cannot be directly taken into account by climate models, nor by mesoscale models, even when the used grid sizes are in the range of only one kilometer and therefore have to be parametrised. Our measurements form a valuable dataset for future validations of such parametrisations of the lead impact in models. However, since our analysis was based on only four cases with highly variable lead characteristics and forcing conditions, it is necessary to carry out more case studies in the future to generalize our findings of the lead impact.

In addition, we analysed the regional impact of lead ensembles on atmospheric temperatures using long transect flights. The near-surface atmospheric temperatures showed a strong dependence on the ice concentration with a correlation of r = -0.66. Furthermore, our analysis showed a temperature change of 0.25 K per 1 % change in ice concentration during the considered time periods of 30 min, which agrees well with the results of a modeling study by Lüpkes et al. (2008b).

There have been approaches to parametrise the heat exchange over lead ensembles using a fetch dependent formulation of the heat fluxes (Andreas and Cash, 1999). When such formulations are used, it is important to know about the distributions of lead widths and lead surface temperatures. Thus, we derived a lead width distribution based on surface temperature measurements during long flight sections. We found that the distribution follows a power law with an exponent of $b = 2.5$ for lead widths above 400 m, which agrees well with values found in other studies by Marcq and Weiss (2012) and Wernecke and Kaleschke (2015). The exponent is smaller for lead widths between 100 and 400 m, which suggests that the distribution is not completely scale invariant. In addition, our data showed that the distribution of the surface temperature difference between the leads and the surrounding thick ice can be described by an exponential function. For future work, it would be interesting to include a joint distribution of lead widths and surface temperature differences in the heat flux calculations.

Cold air outbreaks: observations and modeling

The third major part of this thesis dealt with convection during cold air outbreaks in the polar regions. In the first part, we used dropsonde measurements carried out during the campaign STABLE, supplemented by aircraft profiles, to analyse the downstream development of meteorological variables and the growth of the internal convective boundary layer during four CAOs. To begin with, we validated the quality of the dropsonde data against the aircraft measurements since the dropsondes measure with a lower resolution and a simpler instrumentation than the aircraft. Besides a dry bias in the humidity measurements, we found a generally good quality of the dropsonde measurements, especially of the GPS derived wind vectors.

In two of the four considered CAOs (4 and 26 March 2013) our measurements differed strongly from those during previous campaigns in the Fram Strait region. This was due to the northeast-southwest orientation of the ice edge in the northern Fram Strait region, which was related to the large size of the Whaler's Bay polynya north of Svalbard. Our analysis of sea ice concentrations derived from passive microwave satellite data revealed that the extent of the Whaler's Bay polynya north of Svalbard was much larger in the winters of the years 2012 to 2014 than ever observed in the previous 20 years. This increased polynya size caused strong atmospheric convection during cold air outbreaks in a region north of Svalbard that was typically ice-covered in the last decades.

The strong atmosphere-ocean interaction above the polynya alters the structure of the atmospheric boundary layer during cold air outbreaks and can have a large impact on the local temperatures around Svalbard. Based on ERA-Interim data within the polynya, we found that increased near-surface temperatures in this region are strongly related to a larger polynya extent. In addition, we observed an increase of the potential temperature by 9 K over the open water compared to the pack ice region during one of the CAO cases north of Svalbard. Our measurements also show that the unusual ice conditions generate extreme convective boundary layer heights that are larger than the regional values reported in previous studies. With predictions of further shrinking of the Arctic sea ice volume in the next decades (e.g. Overland and Wang, 2013), a large Whaler's Bay polynya, as observed from 2012 to 2014, might be present more often in the future.

We also considered a small side aspect concerning the parametrisation of turbulent sensible heat fluxes in the convective ABL during CAOs. The performance of three different parametrisations in a 1D mesoscale model was tested and compared to results from LES. Both the considered counter-gradient and eddy-diffusivity mass-flux (EDMF) approaches reproduced the characteristics of the convective ABL better than the mixing length approach, while the shape of the temperature profile was reproduced best for the EDMF approach. As a next step, the performance of the EDMF parametrisation should be tested in a 3D version of the mesoscale model. These tests could also include an EDMF formulation of the latent heat flux, which has already been proposed by Siebesma et al. (2007). Finally, we found that the largest advantage of the EDMF closure is that the ABL height is determined based on a diagnostic equation for the updraft vertical velocity, which is less sensible to changes of the vertical grid spacing of the model. This approach could be also very promising to reduce errors of the ABL growth during CAOs in climate models.

Outlook

Future work should focus on improving the representation of convective processes in the polar atmospheric boundary layer in climate models. The measurements obtained during the STABLE campaign are well suited for the validation of modeling studies with mesoscale models or LES. For example, in a modeling study Lüpkes et al. (2008a) used METRAS to develop a turbulence closure

that accounts for the non-local transport in the convective plumes over leads. They validated their parametrisation with model results from LES. It would be beneficial to repeat such a study using the four case studies over leads measured during STABLE as validation data. In addition, Lüpkes et al. (2008a) only focussed on a lead of 1 km width under near-neutral conditions. The four case studies offer a variety of different lead widths, lead surface temperatures, and upstream stratifications and could thus be used to test and improve the developed parametrisation also for these conditions.

In addition, our measurements during CAOs are very useful for the validation of future modeling studies aimed at improving parametrisations for convective ABLs during CAOs. The two cases on 6 and 7 March are only little influenced by the unusual orientation of the ice edge. They are thus suitable for idealized modeling studies with a simplified quasi 2D model setup, such as in Lüpkes and Schlünzen (1996) and Chechin et al. (2013) using mesoscale models, or in Gryschka et al. (2008, 2014) using LES. These two cases could also be used for further testing of the EDMF closure for CAO applications. The two CAOs on 4 and 26 March will also make very interesting modeling case studies due to the very complex geometry of the ice edge and the influence of the orography of Svalbard. However, here a full 3D model setup including the Svalbard archipelago would be necessary to model these cases.

A Publications within this thesis

Paper 1 – Tetzlaff et al. (2013)

Tetzlaff, A., L. Kaleschke, C. Lüpkes, F. Ament, and T. Vihma. The impact of heterogeneous surface temperatures on the 2-m air temperature over the Arctic Ocean under clear skies in spring. *The Cryosphere*, 7(1):153–166, 2013. doi: 10.5194/tc-7-153-2013

Author contributions
Amelie Tetzlaff developed the trajectory model and developed and implemented the box model. She performed all necessary calculations, analyzed the results and wrote the manuscript. All other authors provided ideas for the conception of the study and improved the manuscript.

A part of the work of this paper has been conducted in the framework of the Master's thesis by the author (Tetzlaff, 2011). There, the trajectory model and a simpler version of the box model were developed. The focus of the research lay only on the quantification of the amount of the observed temperature variability at three sites that could be attributed to a heterogeneous sea ice cover. For this analysis only one reanalysis and one sea ice concentration data set was used.

Within the framework of this dissertation the research question was extended to the determination of a characteristic radius of impact at which changes in sea ice cover affect temperatures at a given site. Additional advances include:

1) Improvement of the box model:

- an additional term accounting for radiative cooling is considered
- for comparison with the measured temperatures at the stations the modeled temperatures at 10 m height are reduced to 2 m assuming a logarithmic temperature profile
- we could also show that the model assumptions are not only valid for a well-mixed ABL, but also hold for a more general power law temperature profile

2) Sensitivity tests:

- backward-trajectories are calculated using two different reanalysis data sets for comparison
- to test the sensitivity to different input data the model is run with four different ice concentration data sets
- model results are also tested using ABL heights from the ERA-Interim reanalysis in addition to the results obtained with constant values for the ABL height
- an analysis of ABL stratification based on Barrow soundings is added

3) Selection of considered cases:

- to exclude cloud-radiative effects only cloud-free trajectories are considered
- to ensure that the well-mixed assumption is valid, only cases with wind speeds exceeding 3 ms^{-1} are considered

Paper 2 – Tetzlaff et al. (2014)

Tetzlaff, A., C. Lüpkes, G. Birnbaum, J. Hartmann, T. Nygård, and T. Vihma. Brief communication: Trends in sea ice extent north of svalbard and its impact on cold air outbreaks as observed in spring 2013. *The Cryosphere*, 8(5):1757–1762, 2014. doi: 10.5194/tc-8-1757-2014

Author contributions
All authors participated in the aircraft campaign and were involved in the flight planning and data acquisition. Amelie Tetzlaff analyzed all data, plotted the results and wrote the manuscript. The other authors contributed ideas for the analysis and improved the manuscript.

Paper 3 – Tetzlaff et al. (2015)

Tetzlaff, A., C. Lüpkes, and J. Hartmann. Aircraft-based observations of atmospheric boundary layer modification over arctic leads. *accepted for Q. J. Roy. Meteor. Soc.*, 2015. doi: 10.1002/qj.2568

Author contributions
Amelie Tetzlaff analyzed the data, plotted the results and wrote the manuscript. All authors participated in the planning of the flight missions and the data acquisition. Christof Lüpkes was involved in the interpretation of the results and reviewed and supplemented the manuscript. Jörg Hartmann was responsible for calibration and pre-processing of the measured data and improved the manuscript.

Acronyms

ABL	Atmospheric Boundary Layer
AMSR-E	Advanced Microwave Scanning Radiometer for EOS
AMSR-2	Advanced Microwave Scanning Radiometer - 2
ASI	ARTIST Sea Ice algorithm
AT	Atmospheric Temperature method
CAO	Cold Air Outbreak
CG	Counter-Gradient approach
EDMF	Eddy-Diffusivity Mass-Flux approach
ERA-Interim	European centre for medium-range weather forecasts ReAnalysis
HYSPLIT	HYbrid Single-Particle Lagrangian Integrated Trajectory transport and dispersion model
IBL	Internal Boundary Layer
IST	Ice Surface Temperature method
JRA	Japanese 25-year ReAnalysis
LES	Large Eddy Simulation
LLJ	Low Level Jet
METRAS	MEsoscale TRAnsport and Stream model
ML	Mixing Length approach
MODIS	MODerate resolution Imaging Spectroradiometer
PALM	PArallelized Large eddy simulation Model
RMSE	Root Mean Squared Error
SSM/I	Special Sensor Microwave Imager
STABLE	Spring Time Atmospheric Boundary Layer Experiment
TV	Temperature Variability method
WNB	Western Nansen Basin

List of Figures

List of Tables

Bibliography

Aagaard, K., A. Foldvik, and S. R. Hillman. The West Spitsbergen Current: Disposition and water mass transformation. *J. Geophys. Res.*, 92(C4):3778–3784, 1987. doi: 10.1029/JC092iC04p03778.

Alam, A. and J. Curry. Lead-induced atmospheric circulations. *J. Geophys. Res. Oceans*, 100(C3): 4643–4651, 1995. ISSN 2156-2202. doi: 10.1029/94JC02562.

Alam, A. and J. A. Curry. Determination of surface turbulent fluxes over leads in arctic sea ice. *J. Geophys. Res*, 102:3331–3343, 1997. doi: 10.1029/96JC03606.

Andersen, S., R. Tonboe, L. Kaleschke, G. Heygster, and L. T. Pedersen. Intercomparison of passive microwave sea ice concentration retrievals over the high concentration Arctic sea ice. *J. Geophys. Res.*, 112:C08004, 2007. doi: 10.1029/2006JC003543.

Andreas, E. L. and B. A. Cash. Convective heat transfer over wintertime leads and polynyas. *J. Geophys. Res.*, 104:25,721–25,734, 1999. doi: 10.1029/1999JC900241.

Andreas, E. L. and B. Murphy. Bulk transfer coefficients for heat and momentum over leads and polynyas. *J. Phys. Oceanogr.*, 16:1875–1883, 1986. doi: 10.1175/1520-0485(1986)016⟨1875:BTCFHA⟩2.0.CO;2.

Andreas, E. L., C. A. Paulson, R. M. William, R. W. Lindsay, and J. A. Businger. The turbulent heat flux from arctic leads. *Bound.-Layer Meteorol.*, 17(1):57–91, 1979. doi: 10.1007/BF00121937.

Andreas, E. L., P. O. G. Persson, R. E. Jordan, T. W. Horst, P. S. Guest, A. A. Grachev, and C. W. Fairall. Parameterizing turbulent exchange over sea ice in winter. *J. Hydromet.*, 11:87–104, 2010. doi: 10.1175/2009JHM1102.1.

Andreas, E.L, W.B. Tucker III, and S. F. Ackley. Atmospheric boundary-layer modification, drag coefficient, and surface heat flux in the antarctic marginal ice zone,. *J. Geophys. Res.*, 89:649–661, 1984. doi: 10.1029/JC089iC01p00649.

Bange, J., F. Beyrich, and D. A. M. Engelbart. Airborne measurements of turbulent fluxes during LITFASS-98: Comparison with ground measurements and remote sensing in a case study. *Theor. Appl. Clim.*, 73(1-2):35–51, 2002. doi: 10.1007/s00704-002-0692-6.

Barber, D., R. Marsden, P. Minnett, G. Ingram, and L. Fortier. Physical processes within the North Water (NOW) polynya. *Atmos.-Ocean*, 39(3):163–166, 2001. doi: 10.1080/07055900.2001.9649673.

Bechtold, P., E. Bazile, F. Guichard, P. Mascart, and E. Richard. A mass-flux convection scheme for regional and global models. *Q. J. Roy. Meteor. Soc.*, 127(573):869–886, 2001. doi: 10.1002/qj.49712757309.

Bitz, C. M., M. M. Holland, M. Eby, and A. J. Weaver. Simulating the ice-thickness distribution in a coupled climate model. *J. Geophys. Res.*, 106(C2):2441–2463, 2001. doi: 10.1029/1999JC000113.

Blackadar, A. K. Exchange in a neutral atmosphere. *J. Geophys. Res.*, 67(8), 1962. doi: 10.1029/JZ067i008p03095.

Boisvert, L. N., T. Markus, C. L. Parkinson, and T. Vihma. Moisture fluxes derived from eos aqua satellite data for the north water polynya over 2003-2009. *J. Geophys. Res.*, 117:D06119, 2012. doi: 10.1029/2011JD016949.

Bromwich, D. H., K. M. Hines, and L.-S. Bai. Development and testing of polar weather research and forecasting model: 2. arctic ocean. *J. Geophys. Res.*, 114:D08122, 2009. doi: 10.1029/2008JD010300.

Brown, A. R. Evaluation of parametrization schemes for the convective boundary layer using large-eddy simulation results. *Bound.-Layer Meteorol.*, 81(2):167–200, 1996. doi: 10.1007/BF00119064.

Brümmer, B. Boundary-layer modification in wintertime cold-air outbreaks from the arctic sea ice. *Bound.-Layer Meteorol.*, 80(1-2):109–125, 1996. doi: 10.1007/BF00119014.

Brümmer, B. Boundary layer mass, water, and heat budgets in wintertime cold-air outbreaks from the arctic sea ice. *Mon. Weather Rev.*, 125(8):1824–1837, 1997. doi: 10.1175/1520-0493(1997)125⟨1824:BLMWAH⟩2.0.CO;2.

Brümmer, B. Roll and cell convection in wintertime arctic cold-air outbreaks. *J. Atmos. Sci.*, 56(15):2613–2636, 1999. doi: 10.1175/1520-0469(1999)056⟨2613:RACCIW⟩2.0.CO;2.

Brümmer, B. and S. Pohlmann. Wintertime roll and cell convection over greenland and barents sea regions: A climatology. *J. Geophys. Res.*, 105(D12):15559–15566, 2000. doi: 10.1029/1999JD900841.

Brümmer, B. and S. Thiemann. The atmospheric boundary layer in an Arctic wintertime on-ice air flow. *Bound.-Layer Meteorol.*, 104(1):53–72, 2002. doi: 10.1023/A:1015547922104.

Brümmer, B., B. Rump, and G. Kruspe. A cold air outbreak near Spitsbergen in springtime – Boundary-layer modification and cloud development. *Bound.-Layer Meteorol.*, 61(1-2):13–46, 1992. doi: 10.1007/BF02033993.

Cavalieri, D., T. Markus, and J. Comiso. AMSR-E/Aqua daily L3 12.5 km brightness temperature, sea ice conentration & snow depth polar grids v002. *Boulder, Colorado USA: National Snow and Ice Data Center*, Digital media, 2004.

Cavalieri, D. J. and C. L. Parkinson. Arctic sea ice variability and trends, 1979-2010. *The Cryosphere*, 6 (4):881–889, 2012. doi: 10.5194/tc-6-871-2012.

Chechin, D. G., C. Lüpkes, I. A. Repina, and V. M. Gryanik. Idealized dry quasi 2-d mesoscale simulations of cold-air outbreaks over the marginal sea ice zone with fine and coarse resolution. *J. Geophys. Res.*, 118(16):8787–8813, 2013. doi: 10.1002/jgrd.50679.

Chlond, Andreas. Three-dimensional simulation of cloud street development during a cold air outbreak. *Bound.-Layer Meteorol.*, 58(1-2):161–200, 1992. doi: 10.1007/BF00120757.

Chrobok, G., S. Raasch, and D. Etling. A comparison of local and non-local turbulence closure methods for the case of a cold air outbreak. *Bound.-Layer Meteorol.*, 58(1-2):69–90, 1992. doi: 10.1007/BF00120752.

Dare, R. A. and B. W. Atkinson. Atmospheric response to spatial variations in concentration and size of polynyas in the southern ocean sea-ice zone. *Bound.-Layer Meteorol.*, 94(1):65–88, 2000. doi: 10.1023/A:1002442212593.

Dee, D. P., S. M. Uppala, A. J. Simmons, P. Berrisford, P. Poli, S. Kobayashi, U. Andrae, A. Balmaseda, G. Balsamo, P. Bauer, P. Bechtold, A. C. M. Beljaars, L. Bergvan de , J. Bidlot, N. Bormann, C. Delsol, R. Dragani, M. Fuentes, A. J. Geer, L. Haimberger, S. B. Healy, H. Hersbach, E. V. Holm, L. Isaksen, P. Kallberg, M. Köhler, M. Matricardi, A. P. McNally, B. M. Monge-Sanz, J. Morcrette, B. Park, C. Peubey, P. Rosnayde , C. Tavolate, J. Thepaut, and F. Vitart. The era-interim reanalysis: configuration and performance of the data-assimilation system. *Q. J. Roy. Meteor. Soc.*, 137:553–597, 2011. doi: 10.1002/qj.828.

Deser, C., R. Tomas, M. Alexander, and D. Lawrence. The seasonal atmospheric response to projected Arctic sea ice loss in the late twenty-first century. *J. Clim.*, 23(2):333–351, 2010. doi: 10.1175/2009JCLI3053.1.

Draxler, R.R. and G.D. Rolph. HYSPLIT (HYbrid Single-Particle Lagrangian Integrated Trajectory) Model access via NOAA ARL READY Website (http://www.arl.noaa.gov/HYSPLIT.php). *NOAA Air Resources Laboratory, College Park, MD*, 2013.

Dufresne, J.-L., M.-A. Foujols, S. Denvil, A. Caubel, O. Marti, O. Aumont, Y. Balkanski, S. Bekki, H. Bellenger, R. Benshila, S. Bony, L. Bopp, P. Braconnot, P. Brockmann, P. Cadule, F. Cheruy, F. Codron, A. Cozic, D. Cugnet, N. Nobletde , J.-P. Duvel, C. EthÃľ, L. Fairhead, T. Fichefet, S. Flavoni, P. Friedlingstein, J.-Y. Grandpeix, L. Guez, E. Guilyardi, D. Hauglustaine, F. Hourdin, A. Idelkadi, J. Ghattas, S. Joussaume, M. Kageyama, G. Krinner, S. Labetoulle, A. Lahellec, M.-P. Lefebvre, F. Lefevre, C. Levy, Z.X. Li, J. Lloyd, F. Lott, G. Madec, M. Mancip, M. Marchand, S. Masson, Y. Meurdesoif, J. Mignot, I. Musat, S. Parouty, J. Polcher, C. Rio, M. Schulz, D. Swingedouw, S. Szopa, C. Talandier, P. Terray, N. Viovy, and N. Vuichard. Climate change projections using the IPSL-CM5 Earth System Model: from CMIP3 to CMIP5. *Clim. Dynam.*, 40(9-10):2123–2165, 2013. doi: 10.1007/s00382-012-1636-1.

Dyer, A. J. A review of flux-profile relationships. *Bound.-Layer Meteorol.*, 7(3):363–372, 1974. doi: 10.1007/BF00240838.

Ebner, L., D. Schröder, and G. Heinemann. Impact of laptev sea flaw polynyas on the atmospheric boundary layer and ice production using idealized mesoscale simulations. *Pol. Res.*, 30:7210, 2011. doi: 10.3402/polar.v30i0.7210.

Esau, I. N. Amplification of turbulent exchange over wide Arctic leads: Large-eddy simulation study. *J. Geophys. Res.*, 112(D8), 2007. doi: 10.1029/2006JD007225.

Etling, D. and R. A. Brown. Roll vortices in the planetary boundary layer: A review. *Bound.-Layer Meteorol.*, 65(3):215–248, 1993. doi: 10.1007/BF00705527.

Fetterer, F., K. Knowles, W. Meier, and M. Savoie. Sea Ice Index. *Boulder, Colorado USA: National Snow and Ice Data Center.*, 2002. doi: 10.7265/N5QJ7F7W.

Fiedler, E. K., T. A. Lachlan-Cope, I. A. Renfrew, and J. C. King. Convective heat transfer over thin ice covered coastal polynyas. *J. Geophys. Res.*, 115:C10051, 2010. doi: 10.1029/2009JC005797.

Friehe, C. A., W. J. Shaw, D. P. Rogers, K. L. Davidson, W. G. Large, S. A. Stage, G. H. Crescenti, S. J. S. Khalsa, G. K. Greenhut, and F. Li. Air-sea fluxes and surface layer turbulence around a sea surface temperature front. *J. Geophys. Res.*, 96(C5):8593–8609, 1991. doi: 10.1029/90JC02062.

Garbrecht, T., C. Lüpkes, E. Augstein, and C. Wamse. Influence of a sea ice ridge on low-level airflow. *J. Geophys. Res.*, 104:24,499–24,507, 1999. doi: 10.1029/1999JD900488.

Garbrecht, T., C. Lüpkes, J. Hartmann, and M. Wolff. Atmospheric drag coefficients over sea ice - validation of a parametrisation concept. *Tellus A*, 54:205–21, 2002. doi: 10.1034/j.1600-0870.2002.01253.x.

Garratt, J. R. The internal boundary layer - a review. *Bound.-Layer Meteorol.*, 50(1-4):171–203, 1990. doi: 10.1007/BF00120524.

Gent, P. R., G. Danabasoglu, L. J. Donner, M. M. Holland, E. C. Hunke, S. R. Jayne, D. M. Lawrence, R. B. Neale, P. J. Rasch, M. Vertenstein, P. H. Worley, Z.-L. Yang, and M. Zhang. The community climate system model version 4. *J. Clim.*, 24:4973–4991, 2011. doi: 10.1175/2011JCLI4083.1.

Glendening, J. W. Horizontally integrated atmospheric heat flux from an Arctic lead. *J. Geophys. Res.*, 100(C3):4613–4620, 1995. doi: 10.1029/94JC02424.

Glendening, J. W. and S. D. Burk. Turbulent transport from an Arctic lead: A large-eddy simulation. *Bound.-Layer Meteorol.*, 59(4):315–339, 1992. doi: 10.1007/BF02215457.

Gordon, H. B. and S. P. O'Farrell. Transient climate change in the csiro coupled model with dynamic sea ice. *Mon. Weather Rev.*, 125(5):875–908, 1997. doi: 10.1175/1520-0493(1997)125⟨0875:TCCITC⟩2.0.CO;2.

Grachev, A. A., E. L. Andreas, C. W. Fairall, P. S. Guest, and P. O. G. Persson. Sheba flux-profile relationships in the stable atmospheric boundary layer. *Bound.-Layer Meteorol.*, 124(3):315–333, 2007. doi: 10.1007/s10546-007-9177-6.

Gryschka, M. and S. Raasch. Roll convection during a cold air outbreak: A large eddy simulation with stationary model domain. *Geophys. Res. Let.*, 32(14):L14805, 2005. doi: 10.1029/2005GL022872.

Gryschka, M., C. Drüe, D. Etling, and S. Raasch. On the influence of sea-ice inhomogeneities onto roll convection in cold-air outbreaks. *Geophys. Res. Let.*, 35(23), 2008. doi: 10.1029/2008GL035845.

Gryschka, M., J. Fricke, and S. Raasch. On the impact of forced roll convection on vertical turbulent transport in cold air outbreaks. *J. Geophys. Res. Atmos.*, 119(22):12,513–12,532, 2014. doi: 10.1002/2014JD022160.

Guest, P. S. and K. L. Davidson. The effect of observed ice conditions on the drag coefficient in the summer east greenland sea marginal ice zone. *J. Geophys. Res.*, 92(C7):6943–6954, 1987. doi: 10.1029/JC092iC07p06943.

Haas, C., S. Hendricks, H. Eicken, and A. Herber. Synoptic airborne thickness surveys reveal state of Arctic sea ice cover. *Geophys. Res. Lett.*, 37(9), 2010.

Hall, D. K., J. R. Key, K. A. Casey, G. A. Riggs, and D. J. Cavalieri. Sea ice surface temperature product from MODIS. *IEEE Trans. Geosc. Rem. Sens.*, 42:1076–1087, 2004. doi: 10.1109/TGRS.2004.825587.

Hall, D. K., G. A. Riggs, and V. V. Salomonson. MODIS/Terra Sea Ice Extent and IST Daily L3 Global 4km EASE-Grid Day V005. *Boulder, Colorado USA: National Snow and Ice Data Center*, Digital media, 2006.

Hartmann, J., C. Kottmeier, C. Wamser, and E. Augstein. *The polar oceans and their role in shaping the global environment*, chapter Aircraft measured atmospheric momentum, heat and radiation fluxes over Arctic sea ice, pages 443–454. Wiley Online Library, 1994.

Hartmann, J., C. Kottmeier, and R. Raasch. Boundary layer development and roll vortex structure during a cold air outbreak. *Bound.-Layer Meteorol.*, 84:45–65, 1997. doi: 10.1023/A:1000392931768.

Hartmann, J., F. Albers, S. Argentini, A. Bochert, U. Bonafe, W. Cohrs, A. Conidi, D. Freese, T. Georgiadis, A. Ippoliti, L. Kaleschke, C. Lüpkes, U. Maixner, G. Mastrantonio, F. Ravegnani, A. Reuter, G. Trivellone, and A. Viola. Arctic Radiation and Turbulence Interaction Study (ARTIST). *Reports on Polar Research, Alfred Wegener Institute for Polar and Marine Research, Bremerhaven*, 305, 1999.

Herbert, F. and G. Kramm. Trockene deposition reaktionsträger substanzen, beschrieben mit einem diagnostischen simulationsmodell der bodennahen luftschicht. In *Atmosphärische Spurenstoffe und ihr physikalisch-chemisches Verhalten*, pages 190–209. Springer, 1985.

Holland, M. M., C. M. Bitz, E. C. Hunke, W. H. Lipscomb, and J. L. Schramm. Influence of the Sea Ice Thickness Distribution on Polar Climate in CCSM3. *J. Clim.*, 19:2398–2414, 2006. doi: 10.1175/JCLI3751.1.

Holtslag, A. A. M. and C.-H. Moeng. Eddy diffusivity and countergradient transport in the convective atmospheric boundary layer. *J. Atmos. Sci.*, 48(14):1690–1698, 1991. doi: 10.1175/1520-0469(1991)048⟨1690:EDACTI⟩2.0.CO;2.

Holtslag, A. A. M., E. Van Meijgaard, and W. C. De Rooy. A comparison of boundary layer diffusion schemes in unstable conditions over land. *Bound.-Layer Meteorol.*, 76(1-2):69–95, 1995. doi: 10.1007/BF00710891.

Inoue, J., J. A. Curry, and J. A. Maslanik. Application of aerosondes to melt-pond observations over arctic sea ice. *J. Atmos. Ocean. Tech.*, 25(2):327–334, 2008. doi: 10.1175/2007JTECHA955.1.

Inoue, J., E. H. Masatake, T. Enomoto, and T. Kikuchi. Intercomparison of Surface Heat Transfer Near the Arctic Marginal Ice Zone for Multiple Reanalyses: A Case Study of September 2009. *SOLA*, 7: 57–60, 2011. doi: 10.2151/sola.2011-015.

Ivanov, V. V., V. A. Alexeev, I. Repina, N. V. Koldunov, and A. Smirnov. Tracing atlantic water signature in the arctic sea ice cover east of svalbard. *Adv. Met.*, 2012, 2012. doi: 10.1155/2012/201818.

Jakobson, E., T. Vihma, T. Palo, L. Jakobson, H. Keernik, and J. Jaagus. Validation of atmospheric reanalyses over the central arctic ocean. *Geophys. Res. Let.*, 39:L10802, 2012. doi: 10.1029/2012GL051591.

Kaimal, J. C. and J. J. Finnigan. *Atmospheric boundary layer flows: their structure and measurement*. Oxford University Press, 1994. pp. 269.

Kaleschke, L., G. Heygster, C. Lüpkes, A. Bochert, J. Hartmann, J. Haarpaintner, and T. Vihma. SSM/I sea ice remote sensing for mesoscale ocean-atmosphere interaction analysis. *Can. J. Rem. Sens.*, 27 (5):526–537, 2001. doi: 10.1080/07038992.2001.10854892.

Kalnay, E., M. Kanamitsu, R. Kistler, W. Collins, D. Deaven, L. Gandin, M. Iredell, S. Saha, G. White, J. Woollen, Y. Zhu, A. Leetmaa, R. Reynolds, M. Chelliah, W. Ebisuzaki, W. Higgins, J. Janowiak, K. C. Mo, C. Ropelewski, J. Wang, R. Jenne, and D. Joseph. The ncep/ncar 40-year reanalysis project. *Bull. Amer. Meteor. Soc.*, 77:437–471, 1996. doi: 10.1175/1520-0477(1996)077⟨0437:TNYRP⟩2.0.CO;2.

Kolstad, E. W. and T. J. Bracegirdle. Marine cold-air outbreaks in the future: an assessment of IPCC AR4 model results for the Northern Hemisphere. *Clim. Dynam.*, 30(7):871–885, 2008. doi: 10.1007/s00382-007-0331-0.

Lampert, A., M. Maturilli, C. Ritter, A. Hoffmann, M. Stock, A. Herber, G. Birnbaum, R. Neuber, K. Dethloff, T. Orgis, R. Stone, R. Brauner, J. Kässbohrer, C. Haas, A. Makshtas, V. Sokolov, and P. Liu. The Spring-Time Boundary Layer in the Central Arctic Observed during PAMARCMiP 2009. *Atmosphere*, 3(3):320–351, 2012. doi: 10.3390/atmos3030320.

Laxon, S. W., K. A. Giles, A. L. Ridout, D. J. Wingham, R. Willatt, R. Cullen, R. Kwok, A. Schweiger, J. Zhang, C. Haas, S. Hendricks, R. Krishfield, N. Kurtz, S. Farrell, and M. Davidson. CryoSat-2 estimates of Arctic sea ice thickness and volume. *Geophys. Res. Lett.*, 40(4):732–737, 2013. doi: 10.1002/grl.50193.

Lindsay, R. and A. Schweiger. Arctic sea ice thickness loss determined using subsurface, aircraft, and satellite observations. *The Cryosphere*, 9(1):269–283, 2015. doi: 10.5194/tc-9-269-2015.

Lindsay, R. W. and D. A. Rothrock. Arctic sea ice leads from advanced very high resolution radiometer images. *J. Geophys. Res. Oceans*, 100(C3):4533–4544, 1995. ISSN 2156-2202. doi: 10.1029/94JC02393.

Liu, A. Q., G. W. K. Moore, K. Tsuboki, and I. A. Renfrew. The Effect of the Sea-ice Zone on the Development of Boundary-layer Roll Clouds During Cold Air Outbreaks. *Bound.-Layer Meteorol.*, 118 (3):557–581, 2006. doi: 10.1007/s10546-005-6434-4.

Lüpkes, C. and G. Birnbaum. Surface drag in the arctic marginal sea-ice zone: a comparison of different parameterisation concepts. *Bound.-Layer Meteorol.*, 117:179–211, 2005. doi: 10.1007/s10546-005-1445-8.

Lüpkes, C. and K. H. Schlünzen. Modelling the arctic convective boundary-layer with different turbulence parameterizations. *Bound.-Layer Meteorol.*, 79(1-2):107–130, 1996. doi: 10.1007/BF00120077.

Lüpkes, C., V. M. Gryanik, B. Witha, M. Gryschka, S. Raasch, and T. Gollnik. Modeling convection over arctic leads with LES and a non-eddy-resolving microscale model. *J. Geophys. Res.*, 113(C9), 2008a. doi: 10.1029/2007JC004099.

Lüpkes, C., T. Vihma, G. Birnbaum, and U. Wacker. Influence of leads in sea ice on the temperature of the atmospheric boundary layer during polar night. *Geophys. Res. Lett.*, 35:L03805, 2008b. doi: 10.1029/2007GL032461.

Lüpkes, C., T. Vihma, E. Jakobson, G. König-Langlo, and A. Tetzlaff. Meteorological observations from ship cruises during summer to the central arctic: A comparison with reanalysis data. *Geophys. Res. Lett.*, 27:L09810, 2010. doi: 10.1029/2010GL042724.

Lüpkes, C., V. M. Gryanik, J. Hartmann, and E. L. Andreas. A parametrization, based on sea ice morphology, of the neutral atmospheric drag coefficients for weather prediction and climate models. *J. Geophys. Res.*, 117(D13112), 2012a. doi: 10.1029/2012JD017630.

Lüpkes, C., T. Vihma, G. Birnbaum, S. Dierer, T. Garbrecht, V. Gryanik, M. Gryschka, J. Hartmann, G. Heinemann, L. Kaleschke, H. Raasch, S.and Savijärvi, K. Schlünzen, and U. Wacker. *ARCTIC Climate Change - The ACSYS Decade and Beyond*, volume 43 of *Atmospheric and Oceanographic Sciences Library*, chapter 7. Mesoscale modelling of the Arctic atmospheric boundary layer and its interaction with sea ice. Springer, 2012b.

Marcq, S. and J. Weiss. Influence of sea ice lead-width distribution on turbulent heat transfer between the ocean and the atmosphere. *The Cryosphere*, 6(1):143–156, 2012. doi: 10.5194/tc-6-143-2012.

Martin, S., R. Drucker, R. Kwok, and B. Holt. Estimation of the thin ice thickness and heat flux for the Chukchi Sea Alaskan coast polynya from Special Sensor Microwave/Imager data, 1990-2001. *J. Geophys. Res.*, 109:C10012, 2004. doi: 10.1029/2004JC002428.

Maslanik, J., J. Stroeve, C. Fowler, and W. Emery. Distribution and trends in Arctic sea ice age through spring 2011. *Geophys. Res. Lett.*, 38:L13502, 2011. doi: 10.1029/2011GL047735.

Maslanik, J. A. and J. Key. On treatments of fetch and stability sensitivity in large-area estimates of sensible heat flux over sea ice. *J. Geophys. Res.*, 100:4573–4584, 1995. doi: 10.1029/94JC02204.

Matsumura, Y. and H. Hasumi. Brine-driven eddies under sea ice leads and their impact on the arctic ocean mixed layer. *J. Phys. Oceanogr.*, 38:146–163, 2008. doi: 10.1175/2007JPO3620.1.

Maykut, G. A. Large-Scale Heat Exchange and Ice Production. *J. Geophys. Res.*, 87(C10):7971–7984, 1982. doi: 10.1029/JC087iC10p07971.

Maykut, G. A. *The surface heat and mass balance, in: The Geophysics of Sea Ice, NATO ASI Series B Phys.* Plenum Press, 1986.

Meier, W. M., J. A. Maslanik, J. R. Key, and C. W. Fowler. Multiparameter AVHRR-Derived Products for Arctic Climate Studies. *Earth Int.*, 1(5):1–29, 1997. doi: 10.1175/1087-3562(1997)001⟨0001:MADPFA⟩2.3.CO;2.

Meier, W. N., G. K. Hovelsrud, B. E. H. Oort, J. R. Key, K. M. Kovacs, C. Michel, C. Haas, M. A. Granskog, S. Gerland, D. K. Perovich, A. Makshtas, and J. D. Reist. Arctic sea ice in transformation: A review of recent observed changes and impacts on biology and human activity. *Rev. Geophys.*, 52 (3):185–217, 2014. doi: 10.1002/2013RG000431.

Morison, J. H. and M. G. McPhee. Lead convection measured with an autonomous underwater vehicle. *J. Geophys. Res. Oceans*, 103(C2):3257–3281, 1998. doi: 10.1029/97JC02264.

Müller, G. and A. Chlond. Three-dimensional numerical study of cell broadening during cold-air outbreaks. *Bound.-Layer Meteorol.*, 81(3-4):289–323, 1996. doi: 10.1007/BF02430333.

Onarheim, I., L. Smedsrud, R. Ingvaldsen, and F. Nilsen. Loss of sea ice during winter north of svalbard. *Tellus A*, 66:23933, 2014. doi: 10.3402/tellusa.v66.23933.

Onogi, K., J. Tsutsui, H. Koide, M. Sakamoto, S. Kobayashi, H. Hatsushika, T. Matsumoto, N. Yamazaki, H. Kamahori, K. Takahashi, S. Kadokura, K. Wada, K. Kato, R. Oyama, T. Ose, N. Mannoji, and R. Taira. The JRA-25 reanalysis. *JMSJ*, 85:369–432, 2007. doi: 10.2151/jmsj.85.369.

Overland, J. E. and M. Wang. When will the summer arctic be nearly sea ice free? *Geophys. Res. Let.*, 40(10):2097–2101, 2013. doi: 10.1002/grl.50316.

Overland, J. E., S. L. McNutt, J. Groves, S. Salo, E. L. Andreas, and P. O. G. Persson. Regional sensible and radiative heat flux estimates for the winter Arctic during the surface heat budget of the Arctic ocean (SHEBA) experiment. *J. Geophys. Res.*, 105:14,093–14,102, 2000. doi: 10.1029/1999JC000010.

Parkinson, C. L., D. Rind, R. J. Healy, and D. G. Martinson. The Impact of Sea Ice Concentration Accuracies on Climate Model Simulations with the GISS GCM. *J. Clim.*, 14:2606–2623, 2001. doi: 10.1175/1520-0442(2001)014⟨2606:TIOSIC⟩2.0.CO;2.

Perovich, D. K., B. Light, H. Eicken, K. F. Jones, K. Runciman, and S. V. Nghiem. Increasing solar heating of the Arctic Ocean and adjacent seas, 1979–2005: Attribution and role in the ice-albedo feedback. *Geophys. Res. Let.*, 34(19), 2007. doi: 10.1029/2007GL031480.

Persson, P. O. G., C. W. Fairall, E. L. Andreas, P. S. Guest, and D. K. Perovich. Measurements near the atmospheric surface flux group tower at SHEBA: Near-surface conditions and surface energy budget. *J. Geophys. Res.*, 107:8045, 2002. doi: 10.1029/2000JC000705.

Persson, P. Ola G., Dominique Ruffieux, and C. W. Fairall. Recalculations of pack ice and lead surface energy budgets during the Arctic Leads Experiment (LEADEX) 1992. *J. Geophys. Res.*, 102(C11): 25085–25089, 1997. ISSN 2156-2202. doi: 10.1029/97JC02045.

Petersen, G. N. and I. A. Renfrew. Aircraft-based observations of air-sea fluxes over Denmark Strait and the Irminger Sea during high wind speed conditions. *Q. J. Roy. Meteor. Soc.*, 135(645):2030–2045, 2009. doi: 10.1002/qj.355.

Pielke, R. A. *Mesoscale Meteorological Modeling*, chapter 7. Parameterization-Averaged Subgrid-Scale Fluxes. Academic Press, 2002.

Pinto, J. O. and J. A. Curry. Atmospheric convective plumes emanating from leads. 2. Microphysical and radiative processes. *J. Geophys. Res.*, 100(C3):4633–4642, 1995. doi: 10.1029/94JC02655.

Pinto, J. O., J. A. Curry, and K. L. McInnes. Atmospheric convective plumes emanating from leads. 1. Thermodynamic structure. *J. Geophys. Res.*, 100:4621–4631, 1995. doi: 10.1029/94JC02654.

Pinto, J. O., A. Alam, J. A. Maslanik, J. A. Curry, and R. S. Stone. Surface characteristics and atmospheric footprint of springtime Arctic leads at SHEBA. *J. Geophys. Res.*, 108(C4), 2003. doi: 10.1029/2000JC000473.

Raasch, S. Numerical simulation of the development of the convective boundary layer during a cold air outbreak. *Bound.-Layer Meteorol.*, 52(4):349–375, 1990. doi: 10.1007/BF00119429.

Raasch, S. and M. Schröter. PALM - A large-eddy simulation model performing on massively parallel computers. *Meteorol. Z.*, 10(5):363–372, 2001. doi: 10.1127/0941-2948/2001/0010-0363.

Raddatz, R. L., M. G. Asplin, L. Candlish, and D. G. Barber. General characteristics of the atmospheric boundary layer over a flaw lead polynya region in winter and spring. *Bound.-Layer Meteorol.*, 138: 321–335, 2011. doi: 10.1007/s10546-010-9557-1.

Raddatz, R. L., R. J. Galley, L. M. Candlish, M. G. Asplin, and D. G. Barber. Integral profile estimates of sensible heat flux from an unconsolidated sea-ice surface. *Atmos.-Ocean*, 51(2):135–144, 2013. doi: 10.1080/07055900.2012.759900.

Rasmussen, E and J Turner. *Polar Lows: mesoscale weather systems at high latitudes*. Cambridge University Press, Cambridge, 2003.

Renfrew, I. A. and J. C. King. A simple model of the convective internal boundary layer and its application to surface heat flux estimates within polynyas. *Boundary-Layer Meteorol.*, 94(3):335–356, 2000. doi: 10.1023/A:1002492412097.

Renner, A. H. H., S. Gerland, C. Haas, G. Spreen, J. F. Beckers, E. Hansen, M. Nicolaus, and H. Goodwin. Evidence of Arctic sea ice thinning from direct observations. *Geophys. Res. Lett.*, 41(14):5029–5036, 2014. doi: 10.1002/2014GL060369.

Rigor, I., R. Colony, and S. Martin. Variations in surface air temperature observations in the Arctic, 1979 - 1997. *J. Clim.*, 13(5):896–914, 2000. doi: 10.1175/1520-0442.

Robbe, N and O Zielinski. Airborne remote sensing of oil spills - analysis and fusion of multi-spectral near-range data. In *Proceedings of the Institute of Marine Engineering, Science and Technology. Part C. J. Mar. Sci. Enviro.*, volume 2, pages 19–27, 2004.

Rojo, M., C. Claud, P.-E. Mallet, G. Noer, A. Carleton, and M. Vicomte. Polar low tracks over the nordic seas: a 14-winter climatic analysis. *Tellus A*, 67(0), 2015. doi: 10.3402/tellusa.v67.24660.

Ruffieux, D., P. O. G. Persson, C. W. Fairall, and D. E. Wolfe. Ice pack and lead surface energy budgets during LEADEX 1992. *J. Geophys. Res.*, 100:4593–4612, 1995. doi: 10.1029/94JC02485.

Savelyev, S. A. and P. A. Taylor. Internal boundary layers: I. Height formulae for neutral and diabatic flows. *Bound.-Layer Meteorol.*, 115(1):1–25, 2005. doi: 10.1007/s10546-004-2122-z.

Schlünzen, K. H. Das mesoskalige Transport- und Stromungsmodell METRAS - Grundlagen, Validierung, Anwendung. *Hamburger Geophysikalische Einzelschriften*, A88:139 pp., 1988.

Screen, J. A. and I. Simmonds. The central role of diminishing sea ice in recent Arctic temperature amplification. *Nature*, 464:1334–1337, 2010. doi: 10.1038/nature09051.

Serreze, M. C. and R. B. Barry. Processes and impacts of Arctic amplification: A research synthesis . *Global Planet. Change*, 77(1–2):85 – 96, 2011. doi: 10.1016/j.gloplacha.2011.03.004.

Serreze, M. C., A. P. Barrett, J. C. Stroeve, D. N. Kindig, and M. M. Holland. The emergence of surface-based arctic amplification. *The Cryosphere*, 3(1):11–19, 2009. doi: 10.5194/tc-3-11-2009.

Shokr, M. and L. Kaleschke. Impact of surface conditions on thin sea ice concentration estimate from passive microwave observations. *Remote Sens. Environ.*, 121:36–50, 2012. doi: 10.1016/j.rse.2012.01.005.

Siebesma, A. P., P. M. M. Soares, and J. Teixeira. A combined eddy-diffusivity mass-flux approach for the convective boundary layer. *J. Atmos. Sci.*, 64(4):1230–1248, 2007. doi: 10.1175/JAS3888.1.

Smith, D. C. and J. H. Morison. A numerical study of haline convection beneath leads in sea ice. *J. Geophys. Res. Oceans*, 98(C6):10069–10083, 1993. doi: 10.1029/93JC00137.

Spreen, G., L. Kaleschke, and G. Heygster. Sea ice remote sensing using AMSR-E 89-GHz channels. *J. Geophys. Res.*, 113:C02S03, 2008. doi: 10.1029/2005JC003384.

Sreenivasan, K. R., A. J. Chambers, and R. A. Antonia. Accuracy of moments of velocity and scalar fluctuations in the atmospheric surface layer. *Bound.-Layer Meteorol.*, 14(3):341–359, 1978. doi: 10.1007/BF00121044.

Stevens, B., M. Giorgetta, M. Esch, T. Mauritsen, T. Crueger, S. Rast, M. Salzmann, H. Schmidt, J. Bader, K. Block, R. Brokopf, I. Fast, S. Kinne, L. Kornblueh, U. Lohmann, R. Pincus, T. Reichler, and E. Roeckner. Atmospheric component of the MPI-M Earth System Model: ECHAM6. *J. Adv. Modeling Earth Syst.*, 5(2):146–172, 2013. doi: 10.1002/jame.20015.

Stirling, Ian. The importance of polynyas, ice edges, and leads to marine mammals and birds. *J. Marine Syst.*, 10(1–4):9 – 21, 1997. doi: 10.1016/S0924-7963(96)00054-1.

Stössel, A. and M. Claussen. On the momentum forcing of a large-scale sea-ice model. *Clim. Dyn.*, 9(2):71–80, 1993. doi: 10.1007/BF00210010.

Stroeve, J., V. Kattsov, A. Barrett, M. Serreze, T. Pavlova, M. Holland, and W. N. Meier. Trends in arctic sea ice extent from cmip5, cmip3 and observations. *Geophys. Res. Let.*, 39:L095012L16502, 2012. doi: 10.1029/2012GL052676.

Tamura, T., K. I. Ohshima, and S. Nihashi. Mapping of sea ice production for Antarctic coastal polynyas. *Geophys. Res. Let.*, 35(7), 2008. doi: 10.1029/2007GL032903.

Taylor, K. E., R. J. Stouffer, and G. A. Meehl. An Overview of CMIP5 and the Experiment Design. *Bull. Amer. Meteor. Soc.*, 93:485–498, 2012. doi: 10.1175/BAMS-D-11-00094.1.

Tetzlaff, A. Master's thesis: Investigation of the influence of sea ice concentration on boundary layer temperatures using a simple heat flux model. *University of Hamburg, Germany*, 2011.

Tetzlaff, A., L. Kaleschke, C. Lüpkes, F. Ament, and T. Vihma. The impact of heterogeneous surface temperatures on the 2-m air temperature over the Arctic Ocean under clear skies in spring. *The Cryosphere*, 7(1):153–166, 2013. doi: 10.5194/tc-7-153-2013.

Tetzlaff, A., C. Lüpkes, G. Birnbaum, J. Hartmann, T. Nygård, and T. Vihma. Brief communication: Trends in sea ice extent north of svalbard and its impact on cold air outbreaks as observed in spring 2013. *The Cryosphere*, 8(5):1757–1762, 2014. doi: 10.5194/tc-8-1757-2014.

Tetzlaff, A., C. Lüpkes, and J. Hartmann. Aircraft-based observations of atmospheric boundary layer modification over arctic leads. *accepted for Q. J. Roy. Meteor. Soc.*, 2015. doi: 10.1002/qj.2568.

The ERA-Interim archive, version 2.0, . *ERA report series. 1. Technical Report*. Berrisford, P., Dee, D., Poli, P., Brugge, R., Fielding, K., Fuentes, M., Kallberg, P., Kobayashi, S., Uppala, S. and Simmons, A., ECMWF, 2011, 2011.

Tiedtke, M. A comprehensive mass flux scheme for cumulus parameterization in large-scale models. *Mon. Weather Rev.*, 117(8):1779–1800, 1989. doi: 10.1175/1520-0493(1989)117⟨1779:ACMFSF⟩2.0.CO;2.

Tilling, R. L., A. Ridout, A. Shepherd, and D. J. Wingham. Increased Arctic sea ice volume after anomalously low melting in 2013. *Nature Geosc.*, 8(8):643–646, 2015. doi: 10.1038/ngeo2489.

Tisler, P., T. Vihma, G. Müller, and B. Brümmer. Modelling of warm-air advection over arctic sea ice. *Tellus A*, 60:775–788, 2008. doi: 10.3402/tellusa.v60i4.15301.

Tjernström, M. and R. G. Graversen. The vertical structure of the lower Arctic troposphere analysed from observations and the ERA-40 reanalysis. *Q. J. Roy. Meteor. Soc.*, 135:431–443, 2009. doi: 10.1002/qj.380.

Valkonen, T., T. Vihma, and M. Doble. Mesoscale modeling of the atmosphere over antarctic sea ice: A late-autumn case study. *Mon. Weather Rev.*, 136:1457–1474, 2008. doi: 10.1175/2007MWR2242.1.

Vance, A. K., J. P. Taylor, T. J. Hewison, and J. Elms. Comparison of in situ humidity data from aircraft, dropsonde, and radiosonde. *J. Atmos. Ocean. Tech.*, 21:921–932, 2004. doi: 10.1175/1520-0426(2004)021⟨0921:COISHD⟩2.0.CO;2.

Venkatram, A. An examination of methods to estimate the height of the coastal internal boundary layer. *Bound.-Layer Meteorol.*, 36(1-2):149–156, 1986. doi: 10.1007/BF00117465.

Vihma, T. and R. Pirazzini. On the factors controlling the snow surface and 2-m air temperatures over the arctic sea ice in winter. *Bound.-Layer Meteorol.*, 1117:73–90, 2005. doi: 10.1007/s10546-004-5938-7.

Vihma, T., J. Hartmann, and C. Lüpkes. A case study of an on-ice air flow over the arctic marginal sea ice zone. *Bound.-Layer Meteorol.*, 107:189–217, 2003. doi: 10.1023/A:1021599601948.

Vihma, T., J. Jaagus, E. Jakobson, and T. Palo. Meteorological conditions in the Arctic Ocean in spring and summer 2007 as recorded on the drifting ice station Tara. *Geophys. Res. Let.*, 35:L18706, 2008. doi: 10.1029/2008GL034681.

Vihma, T., R. Pirazzini, I. Fer, I. A. Renfrew, J. Sedlar, M. Tjernström, C. Lüpkes, T. Nygård, D. Notz, J. Weiss, D. Marsan, B. Cheng, G. Birnbaum, S. Gerland, D. Chechin, and J. C. Gascard. Advances in understanding and parameterization of small-scale physical processes in the marine Arctic climate system: a review. *Atmos. Chem. Phys.*, 14(17):9403–9450, 2014. doi: 10.5194/acp-14-9403-2014.

Storch, H.von and F. W. Zwiers. *Statistical Analysis in Climate Research*, chapter 8 Regression. Cambridge University Press, 1999.

Wacker, U., K. V. J. Potty, C. Lüpkes, J. Hartmann, and M. Raschendorfer. A Case Study on a Polar Cold Air Outbreak over Fram Strait using a Mesoscale Weather Prediction Model. *Bound.-Layer Meteorol.*, 117(2):301–336, 2005. doi: 10.1007/s10546-005-2189-1.

Walsh, J. E. and W. L. Chapman. Arctic cloud-radiation-temperature associations in observational data and atmospheric reanalyses. *J. Clim.*, 11(11):3030–3045, 1998. doi: 10.1175/1520-0442(1998)011⟨3030:ACRTAI⟩2.0.CO;2.

Weinbrecht, S. and S. Raasch. High-resolution simulations of the turbulent flow in the vicinity of an Arctic lead. *J. Geophys. Res.*, 106(C11):27035–27046, 2001. doi: 10.1029/2000JC000781.

Weisman, B. On the criteria for the occurrence of fumigation inland from a large lake - a reply. *Atmos. Environ.*, 10(2):172 – 173, 1976. doi: 10.1016/0004-6981(76)90243-2.

Wernecke, A. and L. Kaleschke. Lead detection in Arctic sea ice from CryoSat-2: quality assessment, lead area fraction and width distribution. *The Cryosphere Disc.*, 9(2):2167–2200, 2015. doi: 10.5194/tcd-9-2167-2015.

Wetzel, C. and B. Brümmer. An Arctic inversion climatology based on the European Centre Reanalysis ERA-40. *Meteorol. Z.*, 20(6):589–600, 2011. doi: 10.1127/0941-2948/2011/0295.

White, P. W. (Ed.). Ifs documentation cy31r1: Part iv physical processes, 2006. URL `http://www.ecmwf.int/research/ifsdocs/`.

WMO CIMO Guide, . *World Meteorological Organization, Guide to Meteorological Instruments and Methods of Observation, Appendix 4B, WMO-No. 8*. Geneva, 2008.

Yao, T., C. L. Tang, and I. K. Peterson. Modeling the seasonal variation of sea ice in the labrador sea with a coupled multicategory ice model and the princeton ocean model. *J. Geophys. Res. Oceans*, 105 (C1):1153–1165, 2000. doi: 10.1029/1999JC900264.

Young, G. S., D. A. R. Kristovich, M. R. Hjelmfelt, and R. C. Foster. Rolls, streets, waves, and more: A review of quasi-two-dimensional structures in the atmospheric boundary layer. *Bull. Amer. Meteor. Soc.*, 83(7):997–1001, 2002. doi: 10.1175/1520-0477(2002)083⟨0997:RSWAMA⟩2.3.CO;2.

Zulauf, M. A. and S. K. Krueger. Two-dimensional numerical simulations of Arctic leads: Plume penetration height. *J. Geophys. Res.*, 108(C2), 2003a. doi: 10.1029/2000JC000495.

Zulauf, M. A. and S. K. Krueger. Two-dimensional cloud-resolving modeling of the atmospheric effects of Arctic leads based upon midwinter conditions at the Surface Heat Budget of the Arctic Ocean ice camp. *J. Geophys. Res.*, 108(D10), 2003b. doi: 10.1029/2002JD002643.

Acknowledgements

This dissertation was prepared at the Alfred Wegener Institute Helmholtz Centre for Polar and Marine Research in Bremerhaven. A part of this thesis was funded by DFG, namely the results presented in Sect. 4.2 and Sect. 4.3. These results contributed to a joint project between the Alfred Wegener Institute and the Institute of Meteorology and Climatology of the University of Hannover (*"Representation of the convective atmospheric boundary layer in cold-air outbreaks in regional models: a joined study based on observations, Large Eddy Simulation and mesoscale modelling"*, grant LU 818/3-1).

First and foremorst I would like to thank Dr. Christof Lüpkes for being such a great supervisor. I am deeply thankful for his support and advice in all situations and for his very constructive remarks and discussions.

I also express my thanks to Prof. Dr. Peter Lemke and Prof. Dr. Thomas Jung for reviewing of this thesis.

I am grateful for the friendly and successful collaboration with Prof. Dr. Siegfried Raasch and his group.

Special thanks go to all participants of the STABLE campaign who made flying over the Arctic an unforgettable experience. I would like to acknowledge especially the great support of the pilots and the aircraft engineers who went out of their way to keep our research running.

I give my thanks to my great colleges from the "Kafferunde", especially to Wolfgang Cohrs, who always helped to keep my spirits up.

I am also very grateful to Prof. Dr. Lars Kaleschke who offered my a post-doc position although my dissertation had not been quite finished at that point.

Finally, I wish to thank friends and family who provided me with good advice and much needed distractions. And last but not least I thank Richard Schmitt who put back in favor of my dissertation, who was always there for me in difficult times and supported me unconditionally.

Erklärung

Hiermit versichere ich, dass ich

1. die Arbeit ohne unerlaubte fremde Hilfe angefertigt habe,
2. keine anderen als die von mir angegebenen Quellen und Hilfsmittel benutzt habe und
3. die den benutzten Werken wörtlich oder inhaltlich entnommenen Stellen als solche kenntlich gemacht habe.

Hamburg, den

(Amelie Tetzlaff)